Computational Modelling of Atmospheric Flows over Forested Terrain for Wind Energy Applications

Jesus Rodrigues Monteiro
(MSc in Electromechanical Engineering)

Dissertation submitted to the University of Porto
in partial satisfaction of the requirements for the
degree of Doctor in Mechanical Engineering.

March 2, 2026

U.PORTO
FEUP FACULDADE DE ENGENHARIA
UNIVERSIDADE DO PORTO

FEUP, Rua Dr Roberto Frias, s/n, 4200-465, Porto.
Jesus Rodrigues Monteiro
email: up202000027@fe.up.pt

© University of Porto. All rights reserved.

Abstract

Studying atmospheric flow over forested terrain is essential in wind resource assessment and wind turbine siting. This study contributes to that goal by computational fluid dynamics (CFD) simulations of microscale flow, validated against field measurements.

Simulations were carried out to evaluate the performance of common RANS $k-\varepsilon$ canopy models over flat terrain with a forest edge. The results of the mean velocity showed minor differences between models. Models that account for the dissipation of turbulent kinetic energy (TKE) by short-circuiting the energy cascade tend to represent in-canopy turbulence more accurately. In contrast, models that treat the forest mainly as a source of TKE showed larger deviations from observed data.

A canopy model based weak turbulence regime (WTR) hypothesis was incorporated into the RANS $k-\varepsilon$ model and tested in three canopy scenarios: homogeneous forest, forest edge, and forested hill. By including second-order WTR terms, the model achieved better predictive performance than standard canopy models, namely in the forested hill case. The dissipation term formulation outperformed earlier time-scale-based approachs.

The WTR model was tested over both flat and complex terrain. Results showed that it captured the key canopy flow features observed in LES results and field measurements on flat terrain, such as wind speed reduction inside the canopy, the formation of a sub-canopy wind jet caused by sparse foliage, and the development of the internal boundary layer above the canopy. In complex terrain, the WTR model highlighted vegetation-driven flow effects, especially on downhill slopes and in valleys, where significant velocity deficits and increased momentum extraction occur. Overall, the WTR model represented both mean and turbulent flow well over forested areas, without relying on fixed constants typical of currently used RANS $k-\varepsilon$ canopy models.

This research demonstrated that the WTR hypothesis performs well across various terrains and forest types, balancing computational efficiency with physical accuracy. Its ability to capture essential forest–atmosphere interactions makes it a valuable tool for wind energy applications. The findings encourage further development of flow models incorporating detailed canopy structures to enhance atmospheric simulation accuracy.

Future work will include third-order terms in the WTR model and integrate more detailed surface data—such as the CORINE Land Cover map—alongside tree height information from the Sentinel-2 database and airborne LIDAR surveys. These advances aim to produce more physically realistic canopy models and improve wind resource assessments in forested and complex terrain.

Keywords: Computational Fluid Dynamics (CFD); Wind Energy; Atmospheric Flow; Canopy Flow Modelling; Forested and Complex Terrain.

Resumo

Estudar o escoamento atmosférico sobre terrenos florestados é fundamental para a avaliação do recurso eólico e a instalação de turbinas. Este trabalho contribui para esse objetivo por meio da modelação computacional de escoamentos em microescala, baseada num conjunto de simulações de mecânica de fluidos computacional (MFC) validadas com dados de campo.

Foram feitas simulações para avaliar o desempenho de modelos de canópia RANS $k-\varepsilon$ em terreno plano com borda florestada. Os resultados da velocidade mostraram pequenas diferenças entre os modelos. Modelos que representam a dissipação da energia cinética turbulenta (ECT) por meio do curto-circuito da cascata de energia tendem a reproduzir melhor os níveis de ECT observados. Já os que tratam a floresta principalmente como fonte de ECT apresentaram maiores desvios em relação aos dados observados.

Um modelo de canópia baseado na hipótese do regime de turbulência fraca (WTR) foi integrado ao modelo RANS $k-\varepsilon$ e testado em três cenários com cobertura florestal: floresta homogénea, borda florestada e colina florestada. Com a inclusão de termos de segunda ordem do WTR, o modelo apresentou melhor desempenho preditivo do que os modelos de canópia convencionais, especialmente no caso da colina florestada. A formulação do termo de dissipação superou abordagens anteriores baseadas na escala temporal.

O modelo WTR foi testado em terrenos planos e complexos. Em terreno plano, conseguiu reproduzir bem as principais características do escoamento no canópia observadas em simulações LES e medições de campo, como a redução da velocidade do vento dentro da floresta e o desenvolvimento da camada limite interna acima do canópia. Em terreno complexo, o modelo captou os efeitos da vegetação no escoamento, sobretudo em encostas descendentes e vales, onde se verificaram défices de velocidade e maior extração de momento. No geral, o modelo WTR representou bem o escoamento médio e turbulento sobre áreas florestadas, sem depender de constantes fixas usadas nos modelos RANS $k-\varepsilon$ atuais.

Este estudo demonstrou que a hipótese WTR apresenta bom desempenho em diferentes tipos de terreno e de floresta, equilibrando eficiência computacional com realismo físico. A sua capacidade de representar as principais interações entre a floresta e a atmosfera torna-a uma ferramenta útil para aplicações em energia eólica. Os resultados incentivam o desenvolvimento de modelos de escoamento que considerem estruturas de canópia mais detalhadas, com vista a melhorar a precisão das simulações atmosféricas.

Trabalhos futuros irão incluir termos de terceira ordem no modelo WTR e integrar dados de superfície mais detalhados — como o mapa CORINE Land Cover — em conjunto com informações de altura das árvores provenientes da base de dados Sentinel-2 e de levantamentos LIDAR aéreos. Estes avanços visam criar modelos de canópia fisicamente mais realistas e melhorar a avaliação do recurso eólico em terrenos florestados e complexos.

Palavras-chave: Mecânica de Fluidos Computacional (MFC); Energia Eólica; Escoamento Atmosférico; Modelação do Escoamento em Canópia; Terreno Florestado e Complexo.

Acknowledgements

First and foremost, I thank God for guiding me throughout this journey. Even in the most challenging moments, I always felt supported and deeply grateful.

I thank Prof. José Laginha Palma for his supervision, guidance, and the knowledge he shared with me. His insightful feedback played a crucial role in shaping the direction and quality of this work.

I would also like to thank my teammates, Vasco Batista and Isadora Coimbra, for their patience, support, and valuable ideas, which helped keep this project on track. I am grateful to all my co-authors for their contributions. In particular, João Lopes provided insightful input on the weak turbulence regime approach.

My thanks go to Alice Ely and Jonathan Newton (RES, Renewable Energy Systems Ltd.), and to Peter Denholm, Graeme Watson, and Andreas Athanasopoulos (NP, Natural Power Consultants), for the insightful questions and discussions that encouraged me to focus on the practical aspects of this research. Their perspective helped align the investigation with real-world engineering challenges.

Finally, thank my parents and wife for their unwavering love, support, and encouragement. Their presence has been essential throughout this journey, and this achievement would not have been possible without them.

This work was developed within a research programme coordinated by Prof. José Laginha Palma, in collaboration with RES and NP. Financial support was provided by the Ministry of Higher Education, Science, Technology and Innovation (MESCTI) of Angola through the DP 67/19 doctoral grant (2020–2023), and by the two companies from 2025–2026. Part of the numerical simulations was performed under two Advanced Computing Design Projects, 2021.09680.CPCA (Navigator) and 2024.14673.CPCA.A3 (Deucalion), awarded by the Fundação para a Ciência e a Tecnologia (FCT).

Contents

Abstract i

Resumo iii

Acknowledgements v

Table of Contents vii

List of Figures xi

List of Tables xiii

Nomenclature xv

1 Introduction 1

1.1 Motivation . . . 1

1.2 Brief bibliographic review . . . 2

1.2.1 Flow over homogeneous forest on flat terrain . . . 2

1.2.2 Flow over forest edge on flat terrain . . . 3

1.2.3 Flow modelling over forested complex terrain . . . 4

1.2.4 RANS–$k-\varepsilon$ canopy model approach . . . 5

1.3 Objectives . . . 6

1.4 Author's contributions . . . 7

1.5 Outline of the thesis . . . 8

2 Mathematical Model and Numerical Techniques 9

2.1 Introduction . . . 9

2.2 Governing equations . . . 10

2.2.1 Canopy model . . . 11

2.3 Boundary conditions . . . 11

2.4 Meshing and coordinate transformation . . . 12

2.5 Numerical methods and convergence criteria 13

3 Forest Edge over Flat Terrain: Falster Case Study 15

3.1 Introduction 15

3.2 Experimental data 16

3.3 Numerical techniques 17

3.3.1 Computational domain, canopy description and grid refinement 17

3.4 Results and discussion 18

3.4.1 Scenario 1: flow towards the forest 19

3.4.2 Scenario 2: flow from the forest 20

3.4.3 Model performance and sensitivity to parameterisation 22

3.5 Conclusion 23

4 The Weak Turbulence Regime Approach 25

4.1 Introduction 25

4.2 Mathematical formulation 26

4.2.1 Transport of momentum 27

4.2.2 Transport of turbulent kinetic energy 27

4.2.3 Transport of the dissipation rate of turbulent kinetic energy 28

4.3 Numerical techniques 29

4.4 Results and discussion 30

4.4.1 Homogeneous canopy 30

4.4.2 Forest edge 31

4.4.3 Forested hill 35

4.5 Conclusion 39

5 Weak Turbulence Regime Approach–3D Flow Modelling 41

5.1 Introduction 41

5.2 The weak turbulence regime approach: 3D mathematical formulation 41

5.2.1 Transport of momentum 42

5.2.2 Transport of turbulent kinetic energy 42

5.2.3 Transport of the dissipation rate of turbulent kinetic energy 43

5.3 Experimental data and numerical techniques . . . 44
5.4 Results and discussion . . . 44
5.5 Conclusion . . . 46

6 Assessing the WTR Model over Complex Terrain: Perdigão Case Study 47
6.1 Introduction . . . 47
6.2 The Perdigão field campaign . . . 48
6.2.1 Measurement data . . . 49
6.2.2 Atmospheric stability . . . 50
6.3 Numerical techniques . . . 51
6.3.1 Computational domain and inlet conditions . . . 51
6.3.2 Terrain coverage . . . 51
6.4 Results and discussion . . . 52
6.5 Conclusion . . . 65

7 Conclusions 67
7.1 Main contributions . . . 67
7.2 Future work . . . 68

Appendices 69

A Results from Falster Case of Study 71
A.1 Spatial distribution of flow towards the forest . . . 71
A.1.1 Wind speed distribution . . . 71
A.1.2 Turbulent kinetic energy distribution . . . 72
A.2 Spatial distribution of flow from the forest . . . 73
A.2.1 Wind speed distribution . . . 73
A.2.2 Turbulent kinetic energy distribution . . . 74

B Results from Forest Edge Flow Case 75
B.1 Reynolds shear stress along domain . . . 75
B.2 Table of RMSE and BIAS between LES and RANS . . . 76
B.3 Differences between RANS and LES . . . 77

B.3.1 Wind speed differences along domain 77
B.3.2 Turbulent kinetic energy differences along domain 77
B.3.3 Reynolds shear stress differences along domain 78

C Results from Forested Hill Case **79**

C.1 Reynolds shear stress along domain 79
C.2 Table of RMSE and BIAS between LES and RANS 79
C.3 Differences between RANS and LES 81
C.3.1 Wind speed differences along domain 81
C.3.2 Turbulent kinetic energy differences along domain 81
C.3.3 Reynolds shear stress differences along domain 82

D Publications **83**

D.1 Paper I: Assessing canopy models across forest edges on flat terrain 83
D.2 Paper II-First Draft: Canopy models assessment near a forest edge in two configurations: flow towards and from the forest 94
D.3 Paper III-Abstract: Modelling the flow within forest: The weak turbulence regime approach in the Reynolds-averaged formulation with $k-\varepsilon$ turbulence model. 119
D.4 Paper IV-Abstract: Three-dimensional formulation of the weak turbulence regime in Reynolds-averaged framework with $k-\varepsilon$ turbulence model: the Perdigão case study. 120

Bibliography **121**

List of Figures

1.1 Expected wind capacity additions by 2026 1
1.2 Vertical profiles of normalised wind speed 2
1.3 Characteristics of flow over a forest edge 3
1.4 Characteristics of flow over low hills 5

2.1 Control volume 13

3.1 Computational domain of the flow towards and from the forest, with mast locations 18
3.2 Measurements and computational results of flow towards the forest at M2 19
3.3 Canopy contribution for k and ε transport equations 20
3.4 Measurements and computational results of flow from the forest at Mast M2 . . 21
3.5 Measurements and computational results of flow from the forest at Mast M1 . . 22

4.1 Flow across a homogeneous canopy: profiles of RANS $k-\varepsilon$ canopy models and LES. 31
4.2 Flow across a forest edge: profiles of RANS $k-\varepsilon$ canopy models and LES. . . . 32
4.3 Edge case wind speed (U/U_b) 33
4.4 Edge case TKE/u_*^2 34
4.5 Flow across a forested hill: profiles of RANS $k-\varepsilon$ canopy and LES model. . . . 36
4.6 Hill case wind speed (U/U_b) 37
4.7 Hill case TKE/u_*^2 38

5.1 Measurements and computational results of flow towards the forest at M2 45
5.2 Flow towards the forest: mean streamwise velocity and TKE of WTR model . . 45

6.1 Perdigão site overview 48
6.2 Forest characteristics over the AOI 52
6.3 Velocity deficit and turbulent kinetic energy differences at 17 m a.g.l. for SW . . 53
6.4 Velocity deficit and turbulent kinetic energy differences at 98 m a.g.l. for SW . . 54
6.5 Streamwise wind along transect A for SW winds. 56

6.6 SW wind measurements and computational results for transect A 57
6.7 Streamwise wind along transect B for SW winds. 58
6.8 SW wind measurements and computational results for transect B 59
6.9 Velocity deficit and turbulent kinetic energy differences at 17 m a.g.l. for NE . . 60
6.10 Velocity deficit and turbulent kinetic energy differences at 98 m a.g.l. for NE . . 61
6.11 Streamwise wind along transect A for NE winds. 62
6.12 NE wind measurements and computational results for transect A 63
6.13 Streamwise wind along transect B for NE winds. 64
6.14 NE wind measurements and computational results for transect B 65

A.1.1 Flow towards the forest: streamwise velocity. 71
A.1.2 Flow towards the forest: turbulent kinetic energy. 72
A.2.1 Flow from the forest: streamwise velocity. 73
A.2.2 Flow from the forest: turbulent kinetic energy 74

B.1 Edge case Reynolds shear stress 75
B.3.1 Wind speed differences 77
B.3.2 Turbulent kinetic energy differences 77
B.3.3 Reynolds shear stress differences 78

C.1 Hill case Reynolds shear stress 79
C.3.1 Wind speed differences 81
C.3.2 Turbulent kinetic energy differences 81
C.3.3 Reynolds shear stress differences 82

List of Tables

2.1 $k-\varepsilon$ turbulence model constants 11

3.1 Canopy model coefficients for the RANS k-ε model. 16

4.1 Numerical parameters 29
4.2 Error indicator of the flow across the homogeneous canopy 30
4.3 Edge flow: global differences between LES and RANS 35
4.4 Forested hill: global differences between LES and RANS 39

5.1 RMSE and BIAS at mast M2. 44

6.1 Points of interest and elevation above sea level. 49
6.2 Period with near-neutral condition at selected POIs for SW winds. 50

B.2 Error indicator of the flow across a forest edge 76

C.2 Error indicator of the flow across a forested hill 80

Nomenclature

List of Acronyms

2D	Two dimensional
3D	Three dimensional
ABL	Atmospheric boundary layer
a.g.l.	Above ground level
AOI	Area of interest
CFD	Computation fluid dynamics
IBL	Internal boundary layer
IOP	Intensive observational period
LAD	Leaf area density
LAI	Leaf area index
LES	Large eddy simulations
LIDAR	Light detection and ranging
POI	Point of interest
QUICK	Quadratic upwind interpolation scheme
RANS	Reynolds averaged Navier-Stokes
RASS	Radio acoustic sounding system
RMSE	Root mean squared errors
SIMPLE	Semi-implicit method for pressure-linked equations
SODAR	Sonic detection and ranging
TDMA	tri-diagonal matrix algorithm
TKE	Turbulent kinetic energy
WF	Wind farm
WT	Wind turbine
WTR	Weak turbulence regime

Symbols - Greek

β	Component of the coordinate transformation tensor	–
β_d, β_p	Canopy model constants	–
δ_{ij}	Kronecker delta	–
μ	Molecular dynamic viscosity	$\mathrm{kg\,m^{-1}\,s^{-1}}$
μ_T	Turbulent dynamic viscosity	$\mathrm{kg\,m^{-1}\,s^{-1}}$
ν	Molecular kinematic viscosity	$\mathrm{m^2\,s^{-1}}$
ν_T	Turbulent kinematic viscosity	$\mathrm{m^2\,s^{-1}}$
ρ	Fluid density	$\mathrm{kg\,m^{-3}}$
σ_{ij}	Reynolds stress tensor component	$\mathrm{kg\,m^{-1}\,s^{-2}}$
$\sigma_k, \sigma_\varepsilon$	$k-\varepsilon$ turbulence model constants	–
τ_{ij}	Viscous stress tensor component	$\mathrm{kg\,m^{-1}\,s^{-2}}$
ε	Turbulent kinetic energy dissipation	$\mathrm{m^2\,s^{-3}}$
ξ	Orthogonal computational space coordinates	–

Operators

Δ	Absolute/relative difference
$\frac{\partial}{\partial}$	Partial derivative
$\overline{()}$	Temporal average
$()'$	Perturbation

Symbols - Latin

$\overline{u_i' u_j'}$	Turbulent stress	$\mathrm{m^2\,s^{-2}}$
a	Leaf area density	$\mathrm{m^{-1}}$
C_1, C_2	Constants in the turbulence model equation for ε	–
C_μ	$k-\varepsilon$ turbulence model constant	–
$C_{\varepsilon 4}, C_{\varepsilon 5}$	Canopy model constants	–
C_d	Mean drag coefficient	–
F_i	Drag force	$\mathrm{kg\,m^{-2}\,s^{-2}}$
h_c	Canopy height	m
i, j, k	Domain cell index per Cartesian direction	–
J	Jacobian matrix	–

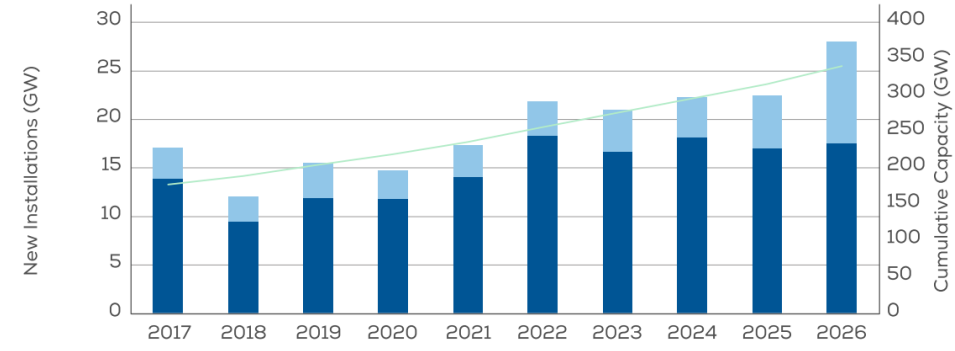
k	Turbulent kinetic energy	$\mathrm{m^2\,s^{-2}}$
p	Pressure field	Pa
P_k	Production term in $k-\varepsilon$ turbulence model	$\mathrm{kg\,m^{-1}\,s^{-3}}$
Q	Weak turbulence regime velocity scale	$\mathrm{m\,s^{-1}}$
S_{C_ε}	Canopy's effect on the transport of ε	$\mathrm{kg\,m^{-1}\,s^{-4}}$
S_{C_k}	Canopy's effect on the transport of k	$\mathrm{kg\,m^{-1}\,s^{-3}}$
u'_s, u'_n	Velocity fluctuation in the streamwise and normal directions	$\mathrm{m\,s^{-1}}$
u, v, w	Cartesian velocity vector components	$\mathrm{m\,s^{-1}}$
u_*	Friction velocity	$\mathrm{m\,s^{-1}}$
U_i	Mean velocity component	$\mathrm{m\,s^{-1}}$
U_{rot}	Wind speed along transect	$\mathrm{m\,s^{-1}}$
v_h	Horizontal velocity	$\mathrm{m\,s^{-1}}$

CHAPTER 1

Introduction

1.1 Motivation

The energy sector is going through a major shift, with less dependence on fossil fuels and a growing use of different renewable sources. As the world moves towards greater electrification, there is a growing need to use resources like wind energy more efficiently. By 2026, renewable energy is expected to provide nearly 95% of the global increase in power capacity (IEA, 2022). According to WindEurope (2022), Europe is expected to install 116 GW of new wind capacity by 2026 (Figure 1.1), with approximately 76% of this coming from onshore wind. As the demand for onshore wind increases, easily accessible sites are becoming scarcer, highlighting the growing importance of site assessments in more complex terrains, such as mountainous and forested regions (e.g., Clifton et al., 2022).



	2017	2018	2019	2020	2021	2022	2023	2024	2025	2026
Offshore	3.2	2.7	3.6	2.9	3.3	3.5	4.4	4.1	5.4	10.4
Onshore	13.9	9.4	11.9	11.8	14.0	18.3	16.6	18.1	17.0	17.6
Cumulative	177	189	204	219	236	256	276	296	315	341

Figure 1.1: Expected wind capacity additions by 2026. Source: WindEurope (2022).

The influence of forests on atmospheric turbulence has been studied, with recent reviews such as Brunet (2020) offering a comprehensive overview of how our understanding and modelling of forest flows have evolved over the past five decades. This modelling remains crucial for wind energy applications, particularly in resource assessment and wind farm design. Accurate prediction of turbulent layers is essential for optimising wind turbine performance and extending operational lifetimes, as increased turbulence can negatively impact both. Inadequate turbulence forecasts may lead to decisions that reduce energy production, such as shutting down specific turbine sectors, adjusting power curves, or relocating turbines.

1.2 Brief bibliographic review

This section outlines the expected flow features over forested flat terrain (homogeneous canopy and canopy edge; Sections 1.2.1 and 1.2.2) and forested hills (Section 1.2.3).

1.2.1 Flow over homogeneous forest on flat terrain

A comprehensive review by Finnigan (2000) outlines how homogeneous vegetation shapes flow patterns, momentum transfer, and turbulence generation. Flow through homogeneous canopies is typically characterised by three distinct sublayers (Figure 1.2): the canopy sublayer (CSL), where vegetation imposes strong drag and modifies the turbulence; the roughness sublayer (RSL), marked by an interplay between mean flow and coherent turbulent structures; and the inertial sublayer (ISL), where the canopy's influence diminishes and turbulent fluxes tend to stabilise with height.

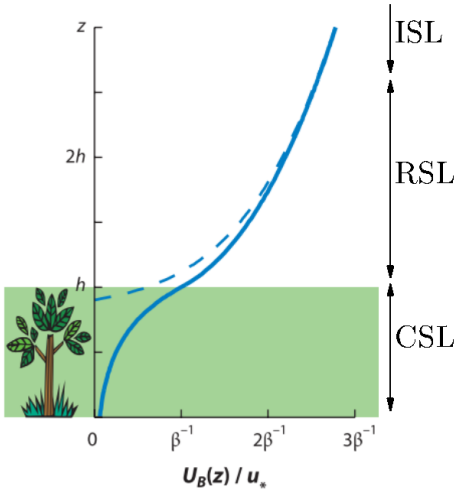


Figure 1.2: Vertical profiles of normalised wind speed. $U_b(z)$ denotes the mean wind speed, u_* the friction velocity, h the canopy height, and β quantifies the depth-integrated drag exerted by the canopy. Source: Belcher et al. (2012).

A wide range of studies has been conducted over the years to explore canopy turbulence, employing diverse modelling strategies (e.g., Brunet, 2020). Poggi et al. (2004) found that dispersive fluxes play a significant role in momentum transfer for sparse canopies, highlighting the sensitivity of these fluxes to canopy structure. To improve representations of flow above vegetation, Harman and Finnigan (2007) introduced a unified model that links canopy and roughness sublayer dynamics, leading to more accurate predictions of the mean flow profile. The double-averaging approach presented by Finnigan and Shaw (2008) offers a robust framework for capturing both temporal variability and spatial heterogeneity within canopy flows, advancing the understanding of momentum transport and drag generation. Results from large-eddy simulations (LES) have revealed the presence of mixing-layer eddies driven by inflection-

point instabilities, which play a dominant role in transporting momentum within the roughness sublayer (Finnigan et al., 2009).

While the homogeneous forest configuration remains valuable for validating canopy models (e.g., Lopes et al., 2021, M. Garza et al., 2019), real-world environments rarely match such idealised conditions. As a result, more complex configurations, such as forest edges (Dupont and Brunet, 2008, Yang et al., 2006b) and forested hills (Dupont et al., 2008, Lopes et al., 2021), have increasingly been studied to better capture the flow dynamics typical of natural forested landscapes.

1.2.2 Flow over forest edge on flat terrain

When atmospheric flow transitions from an open flat surface to a uniformly vegetated area, a complex adjustment process begins at the forest edge (Figure 1.3). This transition initiates an impact zone (i), where a pressure gradient develops, slowing the incoming flow. Downstream, the adjustment region (ii) emerges, extending over a distance of about ten canopy heights (h_c), where vegetation-induced drag continues to reduce flow velocity. This is followed by the canopy-flow region (iii), where the flow adjusts to the forest structure, and above it forms the canopy-shear layer (iv), characterised by shear-generated eddies that govern the exchange of momentum. At the forest leading edge, an internal boundary layer (IBL, v) also develops, marked by enhanced turbulence due to the abrupt change in surface roughness. At the downstream (vi), canopy resistance drops, creating a force imbalance. This accelerates the mean flow and induces a downward vertical velocity. Further downstream, in the far-wake region (vii), flow dynamics are largely governed by streamwise advection and the downward transport of momentum through turbulent mixing (Belcher et al., 2003, 2012).

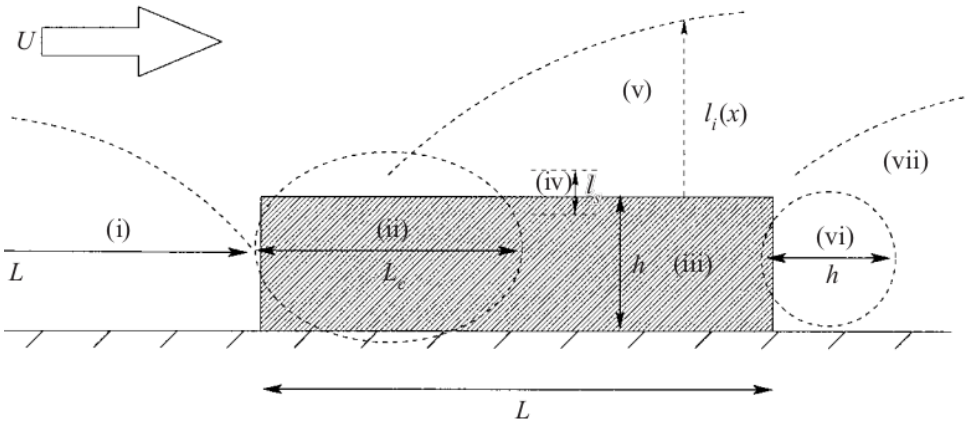


Figure 1.3: Characteristics of the flow over a forest edge: (i) impact region; (ii) adjustment region; (iii) canopy interior; (iv) canopy shear layer; (v) roughness-change region; (vi) exit region; and (vii) far wake. Here, h denotes the canopy height, L the canopy length, L_c the adjustment length, l_s the shear-layer thickness, l_i the depth of the internal boundary layer, and U the streamwise velocity. Source: Belcher et al. (2003).

Several LES studies—such as those by Yang et al. (2006a), Dupont et al. (2011), and Boudreault et al. (2017)—have explored how canopy structure and atmospheric conditions

influence edge flow dynamics. Together, these studies highlight that strong shear at the canopy top generates coherent turbulent structures, and features such as trunk space configuration and canopy inhomogeneities shape turbulence development and flow penetration near the edge. In parallel, Reynolds-averaged Navier–Stokes (RANS) simulations have also contributed to forest edge characterisation. Lopes et al. (2013) demonstrated that tuning canopy parametrisations is vital for reproducing the near-edge acceleration and deceleration zones; and Cintolesi et al. (2023) combined field measurements with simulations to identify three flow regimes: upwind deceleration, a jet within the canopy, and wake recovery. Collectively, these RANS studies confirm the practical value of computational models for edge-flow assessment, yet they also highlight the need for refined turbulence closures and canopy-specific drag schemes to predict exchange processes at forest boundaries across diverse terrains.

Although forest edge flow has been investigated using both field measurements (Dellwik et al., 2014) and computational modelling (Boudreault et al., 2017, Cintolesi et al., 2023), key gaps remain—especially in understanding how far the high-turbulence layer extends downstream on the lee side of forests. It also remains challenging to assess how accurately canopy models represent the forest edge flow (Lopes et al., 2013), which is essential for reliable wind resource evaluation.

1.2.3 Flow modelling over forested complex terrain

Finnigan et al. (2020) provides an insightful review of five decades of progress in understanding boundary-layer flows over complex terrain, including the dynamics of canopy-covered hills. Flow over a forested hill is primarily driven by a large-scale horizontal pressure gradient. On the windward side, the mean velocity increases toward the hill crest, then decreases on the lee side, where turbulent stresses intensify. This flow is typically divided into two regions: the inner and outer layers (Figure 1.4). In the inner region surface layer (ISL), a strong shear stress layer (SSL) develops, accompanied by a near-local turbulence equilibrium. Within the ISL, canopy drag forces appear explicitly in the momentum equation, requiring both turbulence production and dissipation to be accounted for. On the lee side, a wake region forms, characterised by an adverse pressure gradient, enhanced turbulence, and reduced wind speeds. In contrast, the outer region is generally approximated as inviscid, with advection and pressure gradient terms in approximate balance (e.g., Finnigan and Belcher, 2004, Patton and Katul, 2009). Hunt et al. (1988) highlighted the significant role of shear in the middle layer of the upstream flow in driving hilltop acceleration.

Numerous studies have validated theoretical insights into how canopy structure and complex terrain influence wind flow. Arroy et al. (2014) and Vasiljevia et al. (2017) employed Doppler LIDAR and advanced scanning techniques to observe flow patterns induced by complex terrain, capturing key features such as flow asymmetries and three-dimensional wind structures. Building on this, Menke et al. (2019) further characterised ridge-top flows using LIDAR-based approaches. On the canopy side, morphology plays a critical role in shaping leeward airflow, affecting phenomena such as recirculation zones and momentum fluxes (Ma et al., 2020). LES and RANS results from Quimbayo-Duarte et al. (2022) and Venkatraman et al. (2023), highlighted that simplifying assumptions—such as uniform tree height and constant leaf area density—can limit the accuracy of simulations. These simplifications neglect spatial variability in canopy structure, which can obscure important local flow features driven by gaps, edges, or density

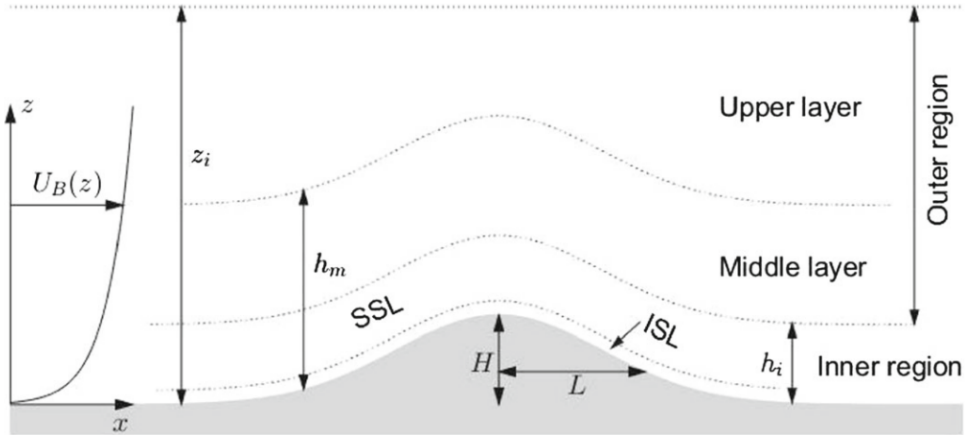


Figure 1.4: Characteristics of flow over low hills. Here, h_i denotes the depth of the shear-stress layer, h_m the middle-layer depth, H the hill height, and L the hill length, defined as the horizontal distance from the summit to the half-height point. $U_B(z)$ represents the undisturbed approaching wind profile, and z_i denotes the boundary-layer depth. Source: Finnigan et al. (2020).

gradients, which are critical for resolving turbulence and momentum exchange processes.

In terms of model development, research converges on the need to represent canopy heterogeneity and drag with greater fidelity. A series of studies show that treating tall canopies simply as rough surfaces, prescribing uniform drag coefficients, or assuming generic forest types degrades predictions of mean velocity, turbulence intensity, and lee-side separation (Ivanell et al., 2018, Tabas et al., 2019, Tolladay and Chemel, 2021).Their collective results confirm that flow fields are sensitive to how the canopy is parametrised.

Together, these studies highlight the ongoing limitations in forest parameterisation, particularly the oversimplification of tree height and canopy structure, which are critical to accurately capturing turbulent flow characteristics in complex, forested terrain. This limitation impedes the ability to make precise wind resource predictions and to assess turbine performance in forested regions effectively.

1.2.4 RANS–$k-\varepsilon$ canopy model approach

LES is capable of resolving flow across canopies, reproducing velocity, turbulent kinetic energy, and Reynolds shear stress profiles without the need for a calibrated canopy model. However, in wind energy applications (Costa et al., 2006, Li et al., 2024), the RANS approach is more commonly adopted due to its lower computational cost. In such cases, the standard k–ε turbulence model is typically enhanced with additional source and sink terms in the transport equations (Section 2.2).

Earlier RANS $k-\varepsilon$ canopy models relied on wind tunnel experimental data to derive and validate model constants (e.g., Liu et al., 1996, Svensson and Häggkvist, 1990). Svensson and Häggkvist (1990) simulated mean wind speed, shear stress, and turbulence intensity downstream from a forest edge as fully developed flow (similar to a homogeneous forest scenario). The

approach did not account for the additional turbulent kinetic energy (TKE) dissipation caused by the canopy, which was later addressed by Green (1992). Liu et al. (1996) incorporated the terms from Green (1992) to model wind speed and TKE profiles, validating their results against wind-tunnel measurements just downwind (half a tree height) of a homogeneous forest. They found that the eddy viscosity was overestimated in areas where the canopy still significantly influenced the flow. Sanz (2003) proposed model constants based on an analytical solution for a dense, homogeneous canopy located far enough from any boundaries, where the mixing length remains relatively constant. Similarly, Costa (2007) validated his model using both the analytical solutions from Sanz (2003) and LES results.

Later, Lopes et al. (2013) reported that the canopy enhances turbulence dissipation, in contrast to the findings of Svensson and Häggkvist (1990), where the canopy was shown to enhance turbulence production. The remaining models account for both mechanisms, balancing production and dissipation. This model was initially calibrated using LES results over a homogeneous canopy and subsequently validated against LES data for flow over a forest edge and a forested hill. In Lopes et al. (2016), and later in Lopes et al. (2021), a new canopy model for the RANS framework was proposed using the $k-\varepsilon$ turbulence model. The canopy-related terms in transport equations (Section 2.2) were derived through a Taylor series expansion of the velocity magnitude, employing a velocity scale based on the total kinetic energy. This formulation assumes a weak turbulence regime, in which turbulent fluctuations are significantly smaller than the mean flow velocity.

On the other hand, Sogachev and Panferov (2006), Sogachev (2009), and Sogachev et al. (2012) assume equilibrium between the production and dissipation of TKE due to plant drag within the canopy. As a result, the transport equation for TKE does not require any additional term; the short-circuiting process ensures that the enhanced production of turbulence due to the canopy matches the enhanced dissipation from the short-circuiting of the energy cascade. Consequently, no additional terms are needed in transport equation of TKE. In this model, the canopy effects are only incorporated into the dissipation transport equation (Section 2.2).

Although RANS models with $k-\varepsilon$ canopy formulations have advanced, they still face limitations in accurately representing flow features near forest edges and over complex terrain, where phenomena such as flow separation and wake formation—particularly on the lee side of forested hills—are common. Consequently, selecting an appropriate canopy model is crucial for site assessment, as some models are better suited to capturing the complex turbulence dynamics in these regions. Moreover, it is important to recognise that simplified representations of forest structure—such as assuming homogeneous forests or uniform leaf area density (LAD) profiles—can lead to inaccurate or overly generalised results (Bannister et al., 2022).

1.3 Objectives

This thesis aims to improve our understanding of airflow over forested terrain for better wind turbine (WT) siting and enhanced wind farm (WF) performance. It examines how various canopy models represent the mean flow and turbulence in these environments. By comparing simulation results with observational data, the study highlights the limitations of existing approaches and explores ways to improve flow predictions in forested areas.

This work builds on earlier research in microscale flow modelling carried out by the same research group. Castro et al. (2003) studied flow over Askervein Hill using the RANS equations, laying a foundation for subsequent developments. Lopes et al. (2013) evaluated five canopy models across a range of flow scenarios, from flat to complex terrain. Building on these results, Lopes et al. (2016) proposed a new RANS-based model using the $k-\varepsilon$ turbulence scheme, later refined by Lopes et al. (2021) for improved canopy modelling in complex environments.

1.4 Author's contributions

The thesis contributes to two main areas: (I) flow modelling over forested flat terrain and (II) flow modelling over forested complex terrain. The core objective is to identify the most suitable canopy model for capturing both mean flow characteristics (wind speed) and second-order statistics (turbulent kinetic energy and shear stress) in flat terrain with forest edges (I) and in more complex forested terrain (II). To support this, the weak turbulence regime (WTR, Lopes et al. (2021)) was implemented in VENTOS®/2 (Castro et al., 2003) to examine how canopy effects influence flow behaviour.

Reliable model evaluation requires high-quality experimental data, and this work uses measurements from the Falster-2008 campaign (Dellwik et al., 2014) and the Perdigão-2017 campaign (Fernando et al., 2019) to assess model performance, uncertainties, and potential improvements.

Part of the work developed in the thesis has been included in the following publications:

- J. R. Monteiro, V. T. P. Batista, J. M. L. M. Palma. Assessing alternative models of atmospheric flow over a forest edge. In 4th Doctoral Congress in Engineering – DCE21: Symposium on Mechanical Engineering, 80–82, 2021. Porto, Portugal: FEUP Edições. ISBN 978-972-752-286-6.

- J. R. Monteiro, V. T. P. Batista, J. M. L. M. Palma. Canopy models evaluation over forests in flat terrain. In 17th EAWE PhD Seminar on Wind Energy: Wind Resource, Turbulence & Wake, 233–234, 2021. Porto, Portugal: EAWE.

- I. L. Coimbra, J. R. Monteiro, V. T. P. Batista. The wind flow from macroscale to microscale. Poster presented at the 17th EAWE PhD Seminar on Wind Energy: Wind Resource, Turbulence & Wake, 2021. Porto, Portugal.

- Paper I: J. R. Monteiro, V. T. P. Batista, J. M. L. M. Palma. Assessing canopy models across forest edges on flat terrain. Journal of Physics: Conference Series, 2767(9):092011, jun 2024. doi: 10.1088/1742-6596/2767/9/092011. URL https://dx.doi.org/10.1088/1742-6596/2767/ 9/092011.

- J. R. Monteiro, V. T. P. Batista, J. M. L. M. Palma. Assessing canopy models across forest edges on flat terrain. Poster presented at the Torque 2024: Wind Resource, Turbulence & Wake, 2024. Florence, Italy.

- J. R. Monteiro, V. T. P. Batista, J. M. L. M. Palma, I. L. Coimbra. Assessing canopy models in forested complex terrain: insights from the Perdigão case study. Accepted for

oral presentation at the WESC 2025: Wind Resource, Turbulence & Wake, 2025. Nante, France.

The remaining work is currently being prepared for submission to peer-reviewed journals, as detailed below:

- Paper II: J. R. Monteiro, V. T. P. Batista, J. M. L. M. Palma, and J. Mann. Canopy models assessment over a forest edge in two configurations: flow towards and from the forest. Wind Energy Science, 2025 (to be submitted).
- Paper III: J. R. Monteiro. Modelling the flow within forest: The weak turbulence regime approach in the Reynolds-averaged formulation with $k - \varepsilon$ turbulence model. Journal of Fluid Mechanics, 2025 (in preparation).
- Paper IV: J. R. Monteiro. Three-dimensional formulation of the weak turbulence regime in Reynolds-averaged framework with $k - \varepsilon$ turbulence model: the Perdigão case study. Boundary-Layer Meteorology, 2025 (in preparation).

As Papers III and IV are still in the early stages, the list of co-authors is yet to be finalised, and the titles are considered preliminary and subject to change.

The VENTOS®/2 CFD code is currently licensed for use by wind energy consultants Renewable Energy Systems Ltd. and Natural Power. The work presented in Chapters 4 and 5 was essential for implementing the WTR approach in both VENTOS®/2 and the VENTOS®/M (Rodrigues, 2013) CFD model, supporting more stable and accurate simulations over forested terrain, with or without orographic complexity. Results from these chapters are being prepared for publication in Papers III and IV. Meanwhile, Chapter 3 was key to understanding the performance of existing canopy models, with findings reported in Papers I and II.

1.5 Outline of the thesis

This thesis addresses two key challenges: computational modelling of wind flow over forested flat terrain and over mountainous forested terrain.

It is structured into seven chapters. Following the introduction in Chapter 1, the mathematical formulation is presented in Chapter 2. Chapter 3 examines the performance of canopy models over flat terrain. The WTR approach is introduced and assessed in Chapter 4, with its three-dimensional (3D) validation discussed in Chapter 5. Chapter 6 addresses the evaluation of canopy models over forested complex terrain. Finally, the main conclusions are summarised in Chapter 7.

CHAPTER 2

Mathematical Model and Numerical Techniques

Abstract

This chapter presents the mathematical framework used to simulate atmospheric flow over forested terrain. The formulation is based on a steady, neutrally stratified flow regime and includes a canopy parametrisation to represent vegetation-induced drag. The governing equations are solved using a Reynolds-averaged Navier–Stokes (RANS) approach with a standard $k-\varepsilon$ turbulence closure. The chapter summarises the governing equations, numerical implementation, and overall modelling strategy.

2.1 Introduction

The mathematical framework adopted in this study is designed to model atmospheric wind flow over forested terrain under idealised conditions. The flow is treated as incompressible and neutrally stratified, and Coriolis effects are neglected. A parametrisation of forest canopy effects is included to account for vegetation-induced momentum loss. The governing equations consist of the continuity equation and the momentum conservation equations, commonly known as the Navier–Stokes equations. To model turbulence within the RANS approach, the $k-\varepsilon$ turbulence model is employed. This widely used closure introduces two additional transport equations—one for the turbulent kinetic energy (k) and another for its dissipation rate (ε)—offering a practical balance between computational efficiency and predictive accuracy across a range of flow scenarios.

The primary aim of this chapter is to present the mathematical framework used in this study to simulate atmospheric wind flow. The simulations were performed using the VENTOS®/2 code (Castro et al., 2003) and its simplified two-dimensional version, VENTOS-2D, which is used in Papers I and II.

After the introduction (Section 2.1), the governing equations are presented in Section 2.2, followed by boundary conditions description (Section 2.3). Section 2.4 describes the meshing system and coordinate transformation, while Section 2.5 outlines the numerical methods and the convergence criteria.

2.2 Governing equations

The mass (2.1) and momentum (2.2) equations were solved in a non-orthogonal curvilinear coordinate system, where β and ξ are components of the coordinate transformation tensor and orthogonal computational space coordinates, and J is the Jacobian matrix (Castro et al., 2003).

$$\frac{\partial}{\partial \xi^j}\left(\rho U_j \beta_k^j\right) = 0 \tag{2.1}$$

$$\rho \frac{\partial}{\partial \xi^j}\left(U_k U_i \beta_k^j\right) = -\frac{\partial}{\partial \xi^j}\left(p\beta_i^j\right) + \frac{\partial}{\partial \xi^j}\left[\left(\sigma_{ki} + \tau_{ki}\right)\beta_k^j\right] + JF_i \tag{2.2}$$

Air density and dynamic viscosity are denoted by ρ and μ. Pressure is represented by p, while F_i denotes a force term accounting for the effects of the canopy. The velocity components in the x^i Cartesian directions are represented by U_i.

The Boussinesq approach is used for the Reynolds stress tensor (2.3),

$$\sigma_{ki} = -\rho\overline{u_k' u_i'} = -\frac{2}{3}\rho k \delta_{ki} + \frac{\mu_t}{J}\left(\frac{\partial U_k}{\partial \xi^m}\beta_i^m + \frac{\partial U_i}{\partial \xi^m}\beta_k^m\right) \tag{2.3}$$

The viscous stress tensor, τ_{ki}, is defined by:

$$\tau_{ki} = \frac{\mu}{J}\left(\frac{\partial U_k}{\partial \xi^m}\beta_i^m + \frac{\partial U_i}{\partial \xi^m}\beta_i^m\right) \tag{2.4}$$

$$\beta_k^j = J\frac{\partial \xi^j}{\partial x^k} \tag{2.5}$$

The transport of turbulent kinetic energy k and its rate of dissipation ε are:

$$\rho \frac{\partial}{\partial \xi^j}\left(U_k k \beta_k^j\right) = \frac{\partial}{\partial \xi^j}\left[\frac{1}{J}\left(\mu + \frac{\mu_t}{\sigma_k}\right)\frac{\partial k}{\partial \xi^m}\beta_k^m \beta_k^j\right] + J\left(P_k - \rho\varepsilon + S_{C_k}\right) \tag{2.6}$$

$$\rho \frac{\partial}{\partial \xi^j}\left(U_k \varepsilon \beta_k^j\right) = \frac{\partial}{\partial \xi^j}\left[\frac{1}{J}\left(\mu + \frac{\mu_t}{\sigma_\varepsilon}\right)\frac{\partial \varepsilon}{\partial \xi^m}\beta_k^m \beta_k^j\right] + J\left(\frac{C_{\varepsilon 1}\varepsilon}{k}P_k - \frac{C_{\varepsilon 2}\rho\varepsilon^2}{k} + S_{C_\varepsilon}\right) \tag{2.7}$$

where P_k is the production term,

$$P_k = \sigma_{ij}\frac{1}{J}\frac{\partial U_i}{\partial \xi^m}\beta_j^m \tag{2.8}$$

μ_t is the eddy viscosity,

$$\mu_t = \rho C_\mu \frac{k^2}{\varepsilon} \tag{2.9}$$

and S_{C_k} and S_{C_ε} (Subsection 2.2.1) represent the canopy's effect on the transport of k and ε.

Terms σ_k, σ_ε, C_1, C_2 and C_μ are $k-\varepsilon$ model constants (Table 2.1), tuned for atmospheric flows (Costa et al., 2006).

In the case of VENTOS-2D, the above equations were solved in a Cartesian system, as indicated in Papers I and II.

Table 2.1: $k-\varepsilon$ turbulence model constants

	$C_{\varepsilon 1}$	$C_{\varepsilon 2}$	C_{μ}	σ_k	σ_{ε}
Atmospheric flow	1,44	1,92	0,033	1,0	1,84

2.2.1 Canopy model

The VENTOS®/2 and VENTOS-2D solvers incorporate the canopy model by including the aerodynamic drag force, F_i (2.10), within the momentum equation (2.2). Additionally, the canopy influences turbulence through source terms S_{C_k} (2.11) in the turbulent kinetic energy equation (2.6) and S_{C_ε} (2.12) in the dissipation rate equation (2.7).

$$F_i = -\,\rho\, C_d\, a(x,y,z)\, |U|\, \overline{U_i} \tag{2.10}$$

$$S_{C_k} = \rho\, C_d\, a(x,y,z) \left(\beta_p |U|^3 - \beta_d |U| k\right) \tag{2.11}$$

$$S_{C_\varepsilon} = \rho\, C_d\, a(x,y,z) \left(C_{\varepsilon 4} \beta_p |U|^3 \frac{\varepsilon}{k} - C_{\varepsilon 5} \beta_d |U| \varepsilon\right) \tag{2.12}$$

C_d is the forest mean drag coefficient, $a(x,y,z)$, the LAD that represents the area of canopy leaves per unit volume (i.e., foliage density over the height of the forest or tree $\mathrm{m}^2\,\mathrm{m}^{-3}$); β_p and β_d, set the fraction of mean flow kinetic energy converted to turbulent kinetic energy (a source term) and the fraction of turbulent kinetic energy dissipated (a sink term) by short-circuiting of the energy cascade; $C_{\epsilon 4}$ and $C_{\epsilon 5}$ adjust the effect of the canopy on the dissipation rate of turbulence.

2.3 Boundary conditions

Near-ground flow is modelled using wall functions (Ferziger and Peric, 2002). The lower boundary is a rough surface, with the first control volume defined by constant tangential Reynolds stress, $\sigma_t = \rho u_*^2$, and tangential velocity following the log law (2.13)(Launder, 1974). Turbulent kinetic energy and dissipation at the wall are given by (2.14) and (2.15).

$$u_t = \frac{u_*}{\kappa} \ln\left(1 + \frac{z}{z_0}\right) \tag{2.13}$$

$$k_{\omega all} = \frac{u_*^2}{C_\mu^{1/2}} \tag{2.14}$$

$$\epsilon_{\omega all} = \frac{u_*^3}{\kappa(z + z_0)} \tag{2.15}$$

Here, $\kappa = 0.4$ is the von Kármán constant, u_* is the friction velocity, and z_0 is the surface roughness length. In addition to the tangential Reynolds stress (2.16), the mean production and dissipation of turbulent kinetic energy, given by (2.17) and (2.18), must also be computed.

$$\sigma_t = \frac{\rho C_\mu^{1/4} k_{\omega all}^{1/2} u_t \kappa}{\ln(1 + z/z_0)} \tag{2.16}$$

$$\bar{\mathcal{P}_k} = ||\sigma_t|| \frac{u_t}{z} \tag{2.17}$$

$$\bar{\epsilon} = \frac{C_\mu^{3/4} k_{\omega all}^{3/2}}{\kappa z} \ln\left(1 + \frac{z}{z_0}\right) \tag{2.18}$$

At the top boundary, the shear stress can be specified using one of three approaches: by assuming a zero shear stress condition (2.19), by prescribing a fixed value (2.20), or by extrapolating from the interior of the domain (2.21).

$$\mu_t \frac{\partial U}{\partial z} = 0 \tag{2.19}$$

$$\mu_t \frac{\partial U}{\partial z} = \rho u_*^2 \tag{2.20}$$

$$\frac{\partial}{\partial z}\left(\mu_t \frac{\partial U}{\partial z}\right) = 0 \tag{2.21}$$

A zero-gradient (null flux) condition is applied for both k and ε at the top boundary:

$$\frac{\partial k}{\partial z} = \frac{\partial \varepsilon}{\partial z} = 0 \tag{2.22}$$

The inlet and initial profiles for wind speed (2.23), turbulent kinetic energy, and its dissipation rate (2.24) and (2.25) are defined as follows:

$$u(\mathbf{x}) = \frac{u_*}{\kappa} \ln\left(1 + \frac{z(\mathbf{x})}{z_0}\right) \tag{2.23}$$

$$k(\mathbf{x}) = \frac{C_\mu^{1/2}}{u_*^2 \left(1 + \frac{z(\mathbf{x})}{\delta_m}\right)^2} \tag{2.24}$$

$$\varepsilon(\mathbf{x}) = \frac{C_\mu^{1/2} k^{3/2}}{k\left(z(\mathbf{x}) + z_0\right)} \tag{2.25}$$

The boundary layer height is denoted by δ_m, $\mathbf{x}$ is a positional vector and z is the height above ground level. If a non-zero shear stress is applied at the top, TKE is set as $k(\mathbf{x}) = C_\mu^{-1/2} u_*^2$. Boundary conditions must be consistent to avoid artificial streamwise gradients. Symmetry conditions at lateral boundaries impose no normal flux, and a zero-gradient at outlet is used.

2.4 Meshing and coordinate transformation

VENTOS®/2 uses a terrain-following structured mesh of quadrilateral elements, projected vertically to form a box-shaped domain covering the area of interest (AOI) and surrounding at-

mospheric boundary layer (ABL). Since complex terrain is poorly represented in Cartesian coordinates, the equations are transformed into a non-orthogonal curvilinear system, mapping the physical domain onto an orthogonal computational space via transformation (2.26).

$$x^i = F^i\left(\xi^1, \xi^2, \xi^3\right) \tag{2.26}$$

In the transformed coordinate system, the ξ^1 and ξ^2 directions follow the terrain surface, while ξ^3 corresponds to the vertical direction in physical space (z). The equations keep their original conservative form and structure, with the only difference being the inclusion of terms related to the coordinate transformation. The model topography is derived from the input data using bilinear interpolation, with increased node density both horizontally and vertically around the AOI. Mesh refinement in both directions is achieved through geometric expansion, where the ratio between adjacent grid nodes remains constant.

2.5 Numerical methods and convergence criteria

The governing equations are solved using a segregated, implicit finite-volume method. Velocity–pressure coupling is handled using the SIMPLE algorithm (Patankar, 1980), in combination with the Rhie–Chow interpolation method (Rhie and Chow, 1983). Each equation is integrated over control volumes (Figure 2.1), resulting in a system of algebraic equations that is solved using the tri-diagonal matrix algorithm (TDMA). Discretisation is performed using standard finite-difference techniques, including upwind, second-order, and third-order interpolation schemes.

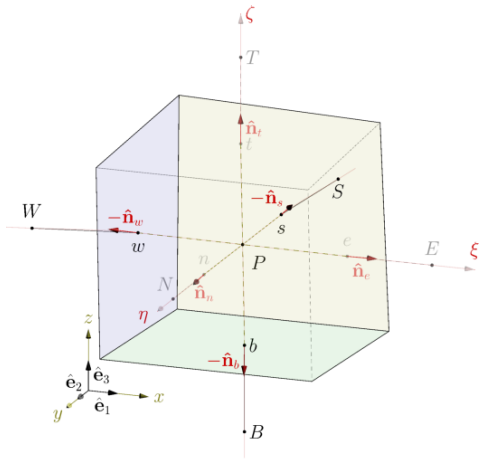


Figure 2.1: Control volume. The diagram illustrates a three-dimensional control volume bounded by six faces: top (T), bottom (B), east (E), west (W), north (N), and south (S), which indicate the neighbouring control volumes. Point P marks the centroid of the current control volume, and b, t, e, w, n, s denote its faces. The vectors $\hat{\mathbf{n}}_b$, $\hat{\mathbf{n}}_t$, $\hat{\mathbf{n}}_e$, $\hat{\mathbf{n}}_w$, $\hat{\mathbf{n}}_n$, and $\hat{\mathbf{n}}_s$ represent the face normal vectors. ξ, η, ζ define the non-orthogonal coordinate system, and the unit vectors $\hat{\mathbf{e}}_1, \hat{\mathbf{e}}_2, \hat{\mathbf{e}}_3$ denote the global Cartesian basis vectors along x, y, z.

The convective terms in the momentum equations are discretised using the QUICK scheme

(Leonard, 1979). For the convective terms in the k and ε equations, the hybrid scheme (Spalding, 1972) is applied. Diffusive terms are discretised using second-order finite-difference methods.

The iterative process stops when either the maximum number of iterations or simulation time is reached, or when the dimensionless residuals of all equations fall below the specified threshold.

CHAPTER 3

Forest Edge over Flat Terrain: Falster Case Study

Abstract

Eight canopy models were tested for neutral flow over flat terrain with a forest edge, using extra source terms to represent vegetation effects on momentum, TKE, and its dissipation. Simulations were compared with field measurements of streamwise velocity, TKE, and Reynolds stress. Results of flow towards and from the forest show that the models reproduced key canopy–flow patterns: reduced wind speed and turbulence inside the forest, a sub-canopy wind jet due to low leaf density, and a high TKE layer near the canopy. Some models showed early internal boundary layer growth and a positive momentum flux layer inside the canopy with stronger downward flux above the canopy. Overall, velocity predictions were similar across models, while those including TKE dissipation via short-circuiting of the energy cascade reproduced observed TKE more accurately, though their Reynolds shear stress predictions near the edge were less in agreement with the measurements, highlighting the complexity of evaluating model performance in the impact zone. In contrast, models that treated the canopy primarily as a TKE source showed larger differences in TKE compared with observations, but captured Reynolds shear stress near the edge more accurately. These results highlight the importance of correctly representing canopy–turbulence interactions to improve flow predictions in forested environments.

3.1 Introduction

The current RANS canopy approach, with its roots in Svensson and Häggkvist (1990), has originated many combinations of its four parameters, as listed in Lopes et al. (2021), of which eight (Table 3.1) were selected to evaluate their performance for simulating the mean and turbulent flow characteristics.

The term "models" is somewhat misleading, as the underlying mathematical framework is identical in all cases. The forest is represented as a porous medium by adding a drag term (F_i) to the momentum equation, along with additional source terms (S_{C_k} and S_{C_ε}) in the turbulence model equations to account for canopy effects on TKE and its dissipation rate (Chapter 2). The so-called "models" differ only in the values assigned to these coefficients (Table 3.1). For instance, Svensson and Häggkvist (1990) assumes the canopy solely increases TKE production, setting $\beta_d = 0$, whereas Lopes et al. (2013) and Lopes et al. (2021) assume a reduction, with $\beta_d > 0$. Other approaches—such as those by Green (1992), Liu et al. (1996), Sanz (2003), and Costa (2007)—use coefficient combinations derived from experiments or theoretical considerations. However, these coefficients remain largely empirical and may lack reliability outside their

Table 3.1: Canopy model coefficients for the RANS k-ε model.

Model	β_p	β_d	$C_{\varepsilon 4}$	$C_{\varepsilon 5}$	β	$C_{\varepsilon 1}$	$C_{\varepsilon 2}$
Svensson (1990)	1.00	-	1.95	-	-	-	-
Green (1992)	1.00	4.00	1.50	1.50	-	-	-
Liu (1996)	1.00	4.00	1.50	0.60	-	-	-
Sanz (2003)	1.00	5.10	0.90	0.90	-	-	-
Costa (2007)	0.17	3.37	0.90	0.90	-	-	
Lopes (2013)	-	4.00	-	0.90			
Viana (2021)	-	2.67	-	1.00	-	-	-
Sogachev (2006)	-	-	-	-	12.00	1.21	1.92

original calibration contexts.

Sogachev and Panferov (2006)'s equation (3.1) and its canopy flow assumptions differ from previous studies. It neglects any canopy effect on the TKE equation and introduces a positive (source) term in the dissipation rate equation, proportional to $|U|\varepsilon$. This contrasts with the sink-type term used by the other models.

$$S_{C_\varepsilon} = \rho\, C_d\, a(x,z)\, |U|\, \beta \sqrt{C_\mu}\, (C_{\varepsilon 2} - C_{\varepsilon 1})\; k\, \frac{\varepsilon}{k} \tag{3.1}$$

Here, β is a constant calibrated to fit observed wind profiles (Sogachev et al., 2012), while $C_{\varepsilon 1}$ and $C_{\varepsilon 2}$ are the standard coefficients for production and destruction terms in the ε equation. In Table 3.1, the constants labelled as Sogachev (2006) correspond to the same set used in Dellwik et al. (2019).

Unlike many studies relying on wind tunnel experiments or numerical simulations (Lopes et al., 2013), this work uses field measurements of flow towards (Dellwik et al., 2014) and from the forest (Paper II) to evaluate eight canopy models (Table 3.1) over a forest edge on flat terrain. The aim is to identify which model best reproduces observed streamwise velocity, turbulence kinetic energy, and Reynolds shear stress. RANS $k-\varepsilon$ simulations assume a neutrally stratified, statistically steady turbulent boundary layer.

The chapter begins with an introduction (Section 3.1), followed by the site description and numerical methods (Sections 3.2 and 3.3). Results and discussion are presented in Section 3.4, with key conclusions in Section 3.5.

3.2 Experimental data

Following a review of relevant studies since Lopes et al. (2013), the field experiment conducted by Dellwik et al. (2014) was selected for its suitability for two-dimensional flow analysis and its comprehensive documentation, further supported by detailed large-eddy simulation results from Boudreault et al. (2017).

The study site is characterised by dense European beech (*Fagus sylvatica*) forest, with an

average canopy height (h_c) of approximately 24 m and a leaf area index (LAI), defined as $\text{LAI} = \int_0^{h_c} a(z)dz$, of around 6 $\text{m}^2\,\text{m}^{-2}$, where $a(z)$ denotes the leaf area density (LAD). Two 45.9 m masts equipped with sonic anemometers were installed: M1 (54°45.79′ N, 12°2.116′ E), located on open grassland approximately $1.5h_c$ upstream of the forest edge, and M2 (54°45.778′ N, 12°2.181′ E), positioned within the forest at a similar distance from the edge. Measurements of the wind flow approaching the forest are reported in Dellwik et al. (2014), while data characterising the flow departing from the forest are presented in Paper II.

The measurements were treated as described in Paper II and used to calculate first-, second-, and third-order moments over ten-minute intervals, as well as Obukhov length (L) and friction velocity. Validation data were then selected for cases with wind approximately perpendicular to the edge (280–300° or 100–120°) and near-neutral stratification ($-0.1 \leq z/L \leq 0.07$), with reference wind speed above U_0 (5.5 ms^{-1} for flow towards the forest, 4 ms^{-1} for flow from the forest), resulting in 124 and 79 ten-minute series, respectively.

3.3 Numerical techniques

The simulations were carried out using the VENTOS-2D model, a simplified version of the VENTOS®/2 code (Castro et al., 2003). The governing equations for mass, momentum, and turbulence—based on the $k-\varepsilon$ closure within the RANS framework—were solved for a neutrally stratified atmosphere. The momentum (2.2), TKE (2.6), and dissipation (2.7) equations accounted for the effects of canopy-induced aerodynamic drag (2.10), as well as turbulence production and dissipation within the canopy (2.11), (2.12) or (3.1).

3.3.1 Computational domain, canopy description and grid refinement

The computational domain was the same as that used by Boudreault et al. (2017), with dimensions of $40h_c$ in the streamwise direction (x) and $8h_c$ in the vertical direction (z). The mesh was structured, with regular control volumes along the x-direction. In the z-direction, the grid spacing was uniform up to $z = 3h_c = 72$ m, beyond which a constant geometric expansion factor, f_z, was applied (Paper I).

Two scenarios were considered, as shown in Figure 3.1: a) flow towards the forest, and b) flow from the forest. The inlet conditions for the first scenario, following Richards and Norris (2011), were: $u(z) = u_* \log(1 + z/z_0)/\kappa$, $k = u_*^2/\sqrt{C_\mu}$, and $\varepsilon = u_*^3/(\kappa(z + z_0))$. The ground was modelled as a rough surface with constant tangential Reynolds stress ($\sigma_t = \rho u_*^2$) and a log-law tangential velocity profile. Zero-gradient conditions for shear stress, turbulent kinetic energy (TKE), and dissipation rate were applied at the top boundary. The second scenario used similar conditions, with the addition of a prescribed velocity, TKE, and dissipation profile at the upwind boundary, distinguishing it from the first scenario (Paper II).

In contrast to Paper I, which employed a streamwise-homogeneous leaf area density (LAD) profile based on the formulation by Boudreault et al. (2017), the present study adopts a spatially heterogeneous LAD distribution, as described in Paper II. A uniform drag coefficient of $C_d = 0.2$, consistent with the value used by Boudreault et al. (2017), was applied, and a constant roughness length of 0.2 m was imposed across the entire domain (Paper I).

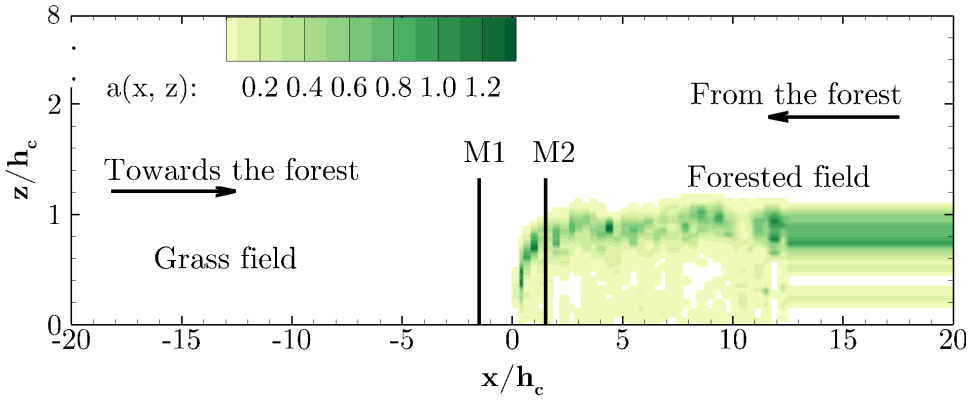


Figure 3.1: Computational domain of the flow towards and from the forest, with mast locations. h_c is the average canopy height, M1 and M2 indicate the mast positions, and $a(x, z)$ denotes the leaf area density (LAD) distribution

The grid independence study, in Paper I, showed that the medium-resolution mesh provided results closely matching those from the fine-resolution mesh. The discrepancies in mean wind speed (U) and turbulent kinetic energy (TKE) were limited to 0.3% and 3.8%. Given these minimal deviations, the medium-resolution mesh was considered sufficiently accurate for model comparison.

In the first and second scenarios, the inlet conditions were carefully adjusted to meet the minimum flow requirements for reliable comparison with field data, as detailed in Paper II. These adjustments ensured consistency in the development of the upstream boundary layer and enabled a more accurate evaluation of canopy-induced flow modifications across the simulated domains.

3.4 Results and discussion

This section presents the results for flow towards the forest (Subsection 3.4.1) and flow from the forest (Subsection 3.4.2). Model performance was assessed using the root mean square error (RMSE) (3.2) and BIAS (3.3) between the RANS $k-\varepsilon$ simulations and measurements of streamwise velocity, TKE, and Reynolds shear stress ($\overline{u'w'}$) at masts M2 and M1 (Figures 3.2, 3.4, and 3.5).

$$RSME = \sqrt{\frac{1}{n}\sum_{j=1}^{n}(\omega_j - \phi_j)^2} \tag{3.2}$$

$$BIAS = \frac{1}{n}\sum_{j=1}^{n}(\omega_j - \phi_j) \tag{3.3}$$

Where n represents the number of experimental points of the measured variable ω_j and ϕ_j is the result of the predictions.

3.4.1 Scenario 1: flow towards the forest

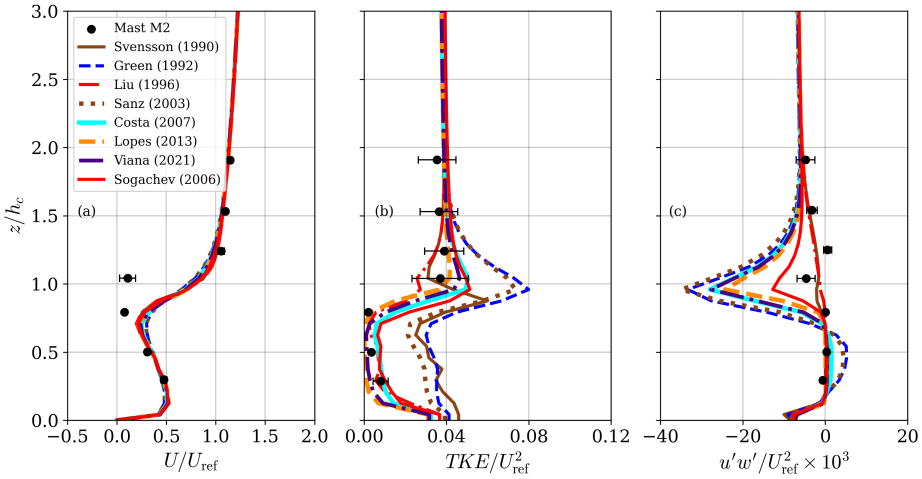


Figure 3.2: Measurements and computational results of flow towards the forest at M2: (a) streamwise velocity; (b) turbulent kinetic energy; (c) Reynolds shear stress. The black horizontal lines are the variability bars.

For streamwise velocity (Figure 3.2a), all models reproduced the general trends expected over a canopy (Dupont et al., 2011, Yang et al., 2006a). Maximum and minimum velocities occurred at $z/h_c \approx 0.2$ and 0.78, corresponding to regions of lower and higher foliage density, respectively. However, none of the models accurately matched observations at $1.04h_c$ and $0.78h_c$, suggesting potential uncertainties in the LAD distribution or canopy height representation near the forest edge. The inflexion point appeared at the canopy top, and above $z = 1.5h_c$, the forest's influence on U diminished.

Turbulent field predictions showed greater variation. For TKE (Figure 3.2b), five models (Lopes, Viana, Costa, Liu, Sogachev) followed the experimental trend, while Svensson, Sanz, and Green overestimated TKE levels below canopy. For Reynolds shear stress (Figure 3.2c), only the Svensson and Liu models aligned with measurements. Turbulence characteristics—such as elevated TKE near the canopy top, positive momentum flux below the crown, and negative momentum further down—were consistent with Dupont et al. (2011) and Boudreault et al. (2017). Only the Svensson and Liu models captured the observed reduction in momentum flux at the canopy top.

Model evaluation based on RMSE and BIAS (summarised in Paper II) showed that all models predicted mean velocity well, with average RMSE and BIAS around 0.30 and 0.10, respectively. For TKE, the Lopes model achieved the best performance, with an RMSE of 0.004 and BIAS of 0.001. Other models presented slightly higher errors, indicating reduced accuracy for turbulence predictions. For $\overline{u'w'}$, the Svensson and Liu models performed best, with RMSEs of 0.0018 and 0.0017, respectively, while others recorded values closer to 0.01.

TKE and $\overline{u'w'}$ profiles were closely linked to the S_k and S_ε terms in the transport equations (Figure 3.3). The Sanz and Green models acted as sources up to the canopy midpoint and as sinks up to about $0.95h_c$. Lopes and Viana acted purely as sinks in both equations. Sogachev contributed only to the ε equation, while Liu and Svensson behaved as sources in both. In the

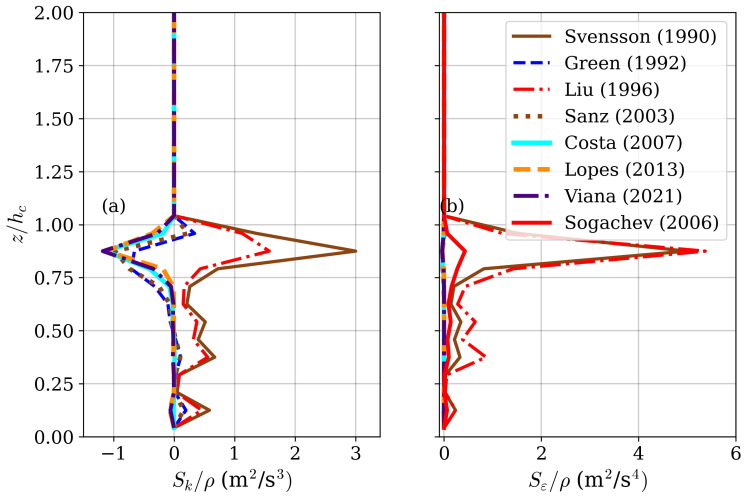


Figure 3.3: Canopy contribution for k (a) and ε (b) transport equations. Flow towards the forest.

top 20% of the canopy, S_ε from Liu and Svensson was nearly 43 times higher than that of other models.

To characterise the flow, spatial distributions of streamwise velocity are shown in Figure A.1.1. All models predicted similar streamwise velocity patterns, with a reduction up to $z/h_c \leq 1$ due to canopy drag, followed by acceleration above. Flow deflection near the canopy edge was evident, and sub-canopy jets developed where foliage density was low. High wind shear caused by dense foliage in the upper canopy generated a turbulent layer above (Figure A.1.2, TKE/U_{ref}^2). Within the canopy, turbulence was generally suppressed, except in the Svensson, Green, and Sanz models, which predicted elevated TKE. This contrasts with the expected turbulence damping due to small wake eddies from foliage but is consistent with observations in sparse pine forests where a shear layer forms beneath the crown (Dupont et al., 2011).

The Reynolds shear stress results, as shown in Paper II, indicated that all models developed a positive turbulent momentum flux ($\overline{u'w'}/U_{ref}^2$) layer within the canopy, starting at the edge, likely linked to the sub-canopy wind jet. A high momentum flux developed above the canopy within the internal boundary layer, with Svensson and Liu predicting near-zero momentum flux near the edge, while the other models estimated higher shear stress magnitudes, consistent with previous studies (Boudreault et al., 2017, Dupont et al., 2011).

3.4.2 Scenario 2: flow from the forest

The streamwise velocity, TKE, and $\overline{u'w'}$ results for the flow emerging from the forest (Figures 3.4 and 3.5) were computed for all models. For the streamwise velocity, the maximum and minimum values at M2 occur at $z/h_c = 0.2$ and approximately 0.8, respectively. Above this height, the flow begins to recover. At M1, flow recirculation is noticeable up to $z/h_c \leq 0.25$ across all wind profiles, except for Svensson and Green. Among the models, Liu most closely matched the

experimental minimum and maximum velocities at both M2 and M1 (Figures 3.4a and 3.5a). In contrast, Svensson and Green, respectively overestimated and underestimated, these values.

As in Scenario 1, the main differences among the models appear in the turbulence field (Figures 3.4b and 3.5b). All models show similar trends for TKE, apart from Svensson and Green. These two models consistently overpredicted TKE at both M2 and M1, whereas the others aligned more closely with the measurements. When comparing $\overline{u'w'}$ (Figures 3.4c and 3.5c), the models reproduced the measurements, but with differences among them. Svensson and Green predicted higher shear stress, while Liu predicted lower values. This behaviour is linked to the eddy viscosity formulations, which depend on the levels of turbulence production and dissipation. For instance, Svensson and Green predicted higher TKE production, resulting in increased eddy viscosity and thus greater shear stress. The remaining models followed the same general $\overline{u'w'}$ trend.

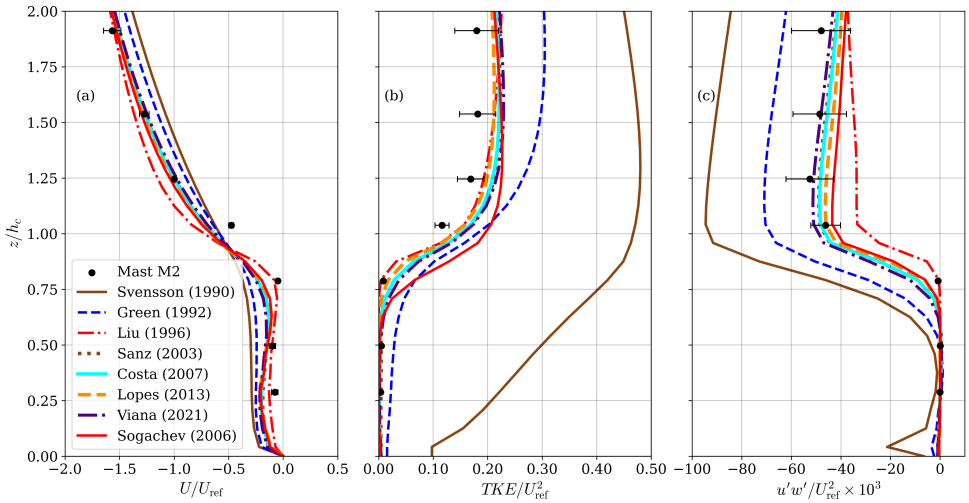


Figure 3.4: Measurements and computational results of flow from the forest at Mast M2: (a) streamwise velocity; (b) turbulent kinetic energy; (c) Reynolds shear stress. The black horizontal lines are the variability bars. The negative sign on wind speed indicates the flow is from the forest.

The RMSE and BIAS results, as shown in Paper II, indicate that the Sanz model provides the most accurate predictions of wind speed, achieving the lowest RMSE at both M2 and M1. The Lopes model performs best in predicting TKE, while Sanz also gives the most accurate Reynolds shear stress predictions at M2. At M1, the Green model provides the best shear stress estimates. In contrast, the Svensson model consistently shows the highest RMSE and BIAS across all variables, reflecting poor agreement with observations.

The contour plot of the normalised streamwise velocity (U/U_{ref}, Figure A.2.1) highlights a deceleration of the flow within the canopy due to vegetation-induced drag. This creates a low-speed zone near the surface, with flow recovery observed above the canopy ($z/h_c > 1$). Localized recirculation zones immediately downwind of the forest edge suggest increased turbulence and momentum exchange within the canopy, although the recirculation was modest and could not be validated due to a lack of measurement.

Above the canopy, a high-TKE layer extends from about $-20h_c$ to beyond $20h_c$ downwind

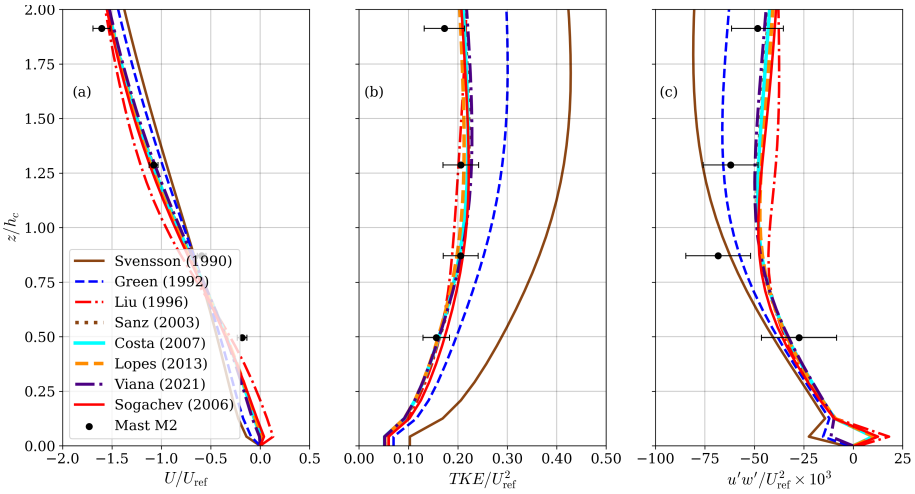


Figure 3.5: Measurements and computational results of flow from the forest at Mast M1: (a) streamwise velocity; (b) turbulent kinetic energy; (c) Reynolds shear stress. The black horizontal lines are the variability bars. The negative sign on wind speed indicates the flow is from the forest.

(Figure A.2.2), a typical feature of flows over forested terrain, with Svensson and Green over-predicting TKE. This layer influences the optimal distance from the forest edge for WT siting. Within the canopy, flow is damped by frictional drag and turbulence dissipation induced by vegetation, with models such as Svensson failing to capture this damping effect. The positive momentum flux within the canopy and the well-defined internal boundary layer (IBL) above it, in Paper II, further illustrate the canopy's influence on the wind profile.

3.4.3 Model performance and sensitivity to parameterisation

The performance of each model is strongly influenced by its original development and the specific adjustments made to align with reference data. For instance, the Svensson model relies on the parameter $C_{\epsilon 4}$ to fit the mean streamwise velocity and Reynolds shear stress, as noted in the literature. In contrast, the Liu model modifies the dissipative term S_{C_ε} to better capture eddy viscosity, assuming a constant mixing length scale (Liu et al., 1996). The tuning of the turbulent viscosity parameter μ_t is critical to the model's overall behaviour, as demonstrated by the Liu model's sensitivity to this adjustment.

The Sogachev model's performance, however, is more dependent on the choice of atmospheric flow constants (C_μ, σ_k, σ_ε, $C_{\varepsilon 1}$, $C_{\varepsilon 2}$, κ) rather than on introducing new constants into the $k-\varepsilon$ framework. For example, the configuration with constants (0.03, 1, 1.3, 1.21, 1.92, 0.4) performed better than the alternative (0.09, 1, 1.7, 1.52, 1.833, 0.4), as also reported by Ivanell et al. (2018). The Lopes model was developed to maximise the correlation between RANS and LES predictions of canopy drag contributions to TKE and dissipation, resulting in excellent TKE predictions but an underestimation of the flow near the ground. This underestimation, associated with turbulent transport terms, is a known limitation of the model. Canopy models that explicitly account for turbulent kinetic energy dissipation, such as Lopes, generally

reproduce TKE behaviour more accurately.

Based on the models' evaluation presented in Subsections 3.4.1 and 3.4.2, the models by Lopes, Viana, Costa, Sanz, Liu, and Sogachev are able to accurately capture canopy flow dynamics. These models reliably represent the development of the turbulent structure above the canopy, which is crucial for understanding the transition from forested surfaces to the free atmosphere. Although variations in the LAD assumptions exist among the models, their impact was found to be minimal, as shown in Paper I and Paper II.

Results from Subsection 3.4.2, particularly relevant for wind resource assessment, indicate that all models except Svensson and Green are suitable for wind energy applications over forested flat terrain. These models provide valuable insights into the horizontal and vertical extension of the high TKE layer, which are key for optimising WT siting.

3.5 Conclusion

Eight canopy models were evaluated for neutrally stratified flow over flat terrain with a forest edge. Forest-atmosphere interactions were represented through additional terms in the transport equations for TKE, dissipation rate ($k - \varepsilon$), and momentum body force. Simulations replicated observed conditions from a benchmarking site, and performance was assessed using mean streamwise velocity, TKE, and Reynolds shear stress.

Key findings are:

- The streamwise velocity, U, showed little variation across all models, indicating a high level of consistency in the prediction of this parameter, regardless of the model used.
- The models by Lopes (Lopes et al., 2013), Viana (Lopes et al., 2021), Costa (Costa, 2007), Sanz (Sanz, 2003), and Sogachev (Sogachev and Panferov, 2006) effectively capture canopy flow dynamics and turbulent structures above the canopy, aiding understanding of the transition from forested to free-atmosphere flow.
- The Liu model (Liu et al., 1996) produced results that closely matched the TKE measurements. However, its representation of the turbulence pattern differed from the other RANS models in terms of the vertical and horizontal distribution of TKE.

Overall, models that mainly account for the dissipation of turbulent kinetic energy due to short-circuiting of the energy cascade–Lopes–offer a more accurate representation of TKE behaviour. In contrast, models treating the forest canopy mainly as a net source of TKE–Svensson–tended to diverge from field observations. Except for the Svensson (Svensson and Häggkvist, 1990) and Green (Green, 1992) models, the remaining six approaches were suitable for wind resource assessments over forested flat terrain, offering valuable insights into both the horizontal and vertical extent of the high TKE layer.

CHAPTER 4

The Weak Turbulence Regime Approach

Abstract

The weak turbulence regime (WTR) developed by Lopes et al. (2016) was integrated into the RANS $k-\varepsilon$ formulation and evaluated in three idealised forest scenarios: a homogeneous canopy, a forest edge, and a forested hill. Model predictions were assessed against LES results. The WTR showed a reliable performance across all cases, particularly in high-turbulence regions, such as canopy edges and the lee side of hills. Over the forest edge, it closely reproduced LES trends in wind speed, TKE, Reynolds shear stress, and dissipation rate, with minor discrepancies near the canopy top. For the forested hill, the model improved the prediction of the recirculation region compared to standard approaches. The inclusion of the dissipation equation, as proposed by Lopes et al. (2021), further enhanced accuracy relative to earlier time-scale-based models. These findings underscore the promise of the WTR approach in forested terrain applications and support continued development toward higher-order closures within the RANS context.

4.1 Introduction

Previous results (Chapter 3) highlight the link between the effectiveness of canopy models and their derivation methods. Some models were designed to reproduce key variables, such as mean wind speed or TKE, with high accuracy. In addition, their coefficients can be sensitive to site-specific conditions (Lopes et al., 2013). This underlines the need for a single model capable of reliably predicting turbulent flow across a range of flow scenarios. The study in this chapter builds on the work of Lopes et al. (2013), proposing canopy constants derived from LES of a homogeneous forest and validated against two additional canopy flows: a finite-length forest and a forested hill. Lopes et al. (2016) later advanced the canopy modelling by using the WTR as a canopy model within the RANS $k-\varepsilon$ framework. Subsequently, Lopes et al. (2021) refined the approach by adjusting the dissipation terms, with results validated against the LES outputs.

The WTR assumes that TKE is small relative to the kinetic energy of the mean flow. Using perturbation theory, a Taylor series expansion is applied to express the velocity magnitude around a characteristic velocity scale defined by the total kinetic energy (mean flow plus turbulence). This formulation enables canopy-induced effects on turbulent quantities to be represented as a series of velocity moments, with the lower-order terms explicitly written in terms of variables available in the $k-\varepsilon$ turbulence model (Lopes et al., 2021). A similar approach was used by Lien et al. (2005), although their characteristic velocity scale was based solely on the magnitude of the spatially averaged wind speed.

This chapter applies the WTR approach (Lopes et al., 2021) within a RANS $k-\varepsilon$ framework, in three canopy configurations: a homogeneous canopy, a forest edge, and a forested hill. The

performance of the WTR is assessed through comparisons with LES results and reference RANS $k-\varepsilon$ models (Chapter 3).

The chapter opens with an introduction (Section 4.1), followed by an overview of the mathematical formulation (Section 4.2) and the numerical techniques used (Section 4.3). Section 4.4 presents results and discussion for flows of increasing complexity—from a horizontally homogeneous canopy, to sequences of clearings and forested areas, and finally a forested hill. The main conclusions are summarised in Section 4.5.

4.2 Mathematical formulation

The WTR formulation is derived under the assumption that turbulence fluctuations remain small compared to the mean velocity,

$$u_i' u_i' \ll U^2 \,. \tag{4.1}$$

This assumption forms the basis of the WTR approach proposed by Lopes et al. (2021). Within this framework, the velocity magnitude is reformulated using perturbation theory as

$$|u| = Q\sqrt{1 + 2\frac{U u_s'}{Q^2} + \frac{u_i' u_i' - 2k}{Q^2}}, \tag{4.2}$$

where the velocity scale Q is defined as

$$Q = \left(U^2 + 2k\right)^{1/2} . \tag{4.3}$$

Near flow separation on the lee side of the forested hill, the mean velocity becomes very small and turbulence is not weak. In these regions, the WTR main assumption (4.1) may not be formally valid. The definition of Q (4.3) does not guarantee that the WTR assumption (4.1) holds. In contrast to Lien et al. (2005), where only the mean velocity is considered, the definition of Q provides a finite velocity magnitude (4.2) when $U \to 0$. This prevents singular behaviour and keeps the equations well defined in separated or recirculating flow.

However, the model is still called WTR because it is derived from the weak turbulence regime. WTR is a global asymptotic framework, not a condition that must be satisfied at every point. It defines the dominant balances, the ordering of terms, and the structure of the perturbation expansion.

The square-root term in (4.2) is subsequently expanded using a Taylor series (Lopes et al., 2021) in order to derive the final model expression. Here, U denotes the magnitude of the mean velocity and u_s' represents the velocity fluctuations in the streamwise direction. The turbulent stress $\overline{u_i' u_j'}$ is modelled using the Boussinesq assumption (2.3).

4.2.1 Transport of momentum

The canopy drag force (2.10) is expressed as a sum of terms with decreasing order of magnitude, as presented in Lopes et al. (2021),

$$F_i(n) = -C_d\, a(y) \sum_{j=0}^{n} s_{U_i}(j)\,. \tag{4.4}$$

The non-zero terms up to second-order are defined in a two-dimensional x, y coordinate system,

$$s_{U_i}(0) = QU_i, \tag{4.5}$$

$$s_U(2) = \frac{U}{Q}\left(\overline{uu}_s - \frac{Uu}{2Q^2}\overline{u}_{sq}\right), \tag{4.6}$$

$$s_V(2) = \frac{U}{Q}\left(\overline{vu}_s - \frac{Uv}{2Q^2}\overline{u}_{sq}\right). \tag{4.7}$$

where $\overline{uu}_s = \overline{uu}s_x + \overline{uv}s_y$ and $\overline{vu}_s = \overline{uv}s_x + \overline{vv}s_y$ represent the directional Reynolds stress tensor components along a specified direction. The directional vector is defined by $s_x = u/U$ and $s_y = v/U$, where u and v are the horizontal and vertical velocity components and $U = \sqrt{u^2 + v^2}$ is the local flow magnitude. This formulation enables the analysis of stress variations along the flow direction or along an inclined surface.

The quantity $\overline{u}_{sq}$ is represented by (4.8). The turbulent stress $\overline{u_i' u_k'}$ is modelled using the Boussinesq approximation (2.3).

$$\overline{u}_{sq} = \overline{uu}s_x^2 + 2\overline{uv}s_x s_y + \overline{vv}s_y^2 \tag{4.8}$$

Starting from the second-order term $s_U(2)$, this approach results in a finite average drag even when the mean velocity is near zero ($U \to 0$) due to turbulent fluctuations. A small drag normal to the flow appears if the velocity components are correlated, indicated by a nonzero Reynolds shear stress $\overline{u_s' u_n'}$, where u_n' represents the velocity fluctuation normal to the streamline. Although the normal component is smaller than the streamwise component (Lopes et al., 2021), this is a key difference between the WTR and other approaches (Chapter 3). Furthermore, the zero-order term (4.5) agrees with the RANS canopy drag (2.10) when $k \ll U^2$ and $Q \approx U$.

4.2.2 Transport of turbulent kinetic energy

The canopy terms in the turbulence kinetic energy (2.11) are defined by

$$S_{C_k}(n) = -C_d\, a(y) \sum_{j=0}^{n} s_k(j)\,, \tag{4.9}$$

where the terms up to the second order are

$$s_k(0) = 2Qk \tag{4.10}$$

$$s_k(2) = U^2 \left(\frac{Q^2 - k}{Q^3} \right) \overline{u}_{sq} \tag{4.11}$$

$\overline{u}_{sq}$ is represented in (4.8). The series was truncated at second-order, providing approximations based on quantities obtainable from standard RANS models. The second-order approximation matches the RANS $k-\varepsilon$ canopy model ($\beta_p = 0$ [2.11]) when TKE is much lower than the mean flow's kinetic energy ($k << U^2$, $Q \approx U$).

4.2.3 Transport of the dissipation rate of turbulent kinetic energy

In contrast to Lopes et al. (2016), where the canopy contribution to the TKE dissipation transport equation, S_{C_ε}, was related to the canopy source term in the TKE transport equation, S_{C_k}, via the turbulence time scale $\tau = k/\varepsilon$, the present approach decomposes the TKE dissipation rate within the canopy (2.12) into distinct large-scale ($s_\varepsilon^{\mathsf{L}}(n)$) and small-scale ($s_\varepsilon^{\mathsf{s}}(n)$) contributions, as proposed by Lopes et al. (2021):

$$S_{C_\varepsilon}(n) \;=\; s_\varepsilon^{\mathsf{L}}(n) + s_\varepsilon^{\mathsf{s}}(n) = -\nu\, C_d \left(\sum_{j=0}^{n} s_\varepsilon^{\mathsf{L}}(j) + \sum_{j=0}^{n} s_\varepsilon^{\mathsf{s}}(j) \right) \tag{4.12}$$

$$\begin{aligned} s_\varepsilon^{\mathsf{L}}(2) = {} & \frac{\partial}{\partial x}\left[a(y)\, Q \left(\frac{u^2}{Q^2} + 1 \right) \right] \frac{\partial \overline{u'u'}}{\partial x} + \frac{\partial}{\partial y}\left[a(y)\, Q \left(\frac{u^2}{Q^2} + 1 \right) \right] \frac{\partial \overline{u'u'}}{\partial y} \\ & + 2\,\frac{\partial}{\partial x}\left[a(y) \left(\frac{uv}{Q} \right) \right] \frac{\partial \overline{u'v'}}{\partial x} + 2\,\frac{\partial}{\partial y}\left[a(y) \left(\frac{uv}{Q} \right) \right] \frac{\partial \overline{u'v'}}{\partial y} \\ & + \frac{\partial}{\partial x}\left[a(y)\, Q \left(\frac{v^2}{Q^2} + 1 \right) \right] \frac{\partial \overline{v'v'}}{\partial x} + \frac{\partial}{\partial y}\left[a(y)\, Q \left(\frac{v^2}{Q^2} + 1 \right) \right] \frac{\partial \overline{v'v'}}{\partial y} \end{aligned} \tag{4.13}$$

$$\begin{aligned} s_\varepsilon^{\mathsf{s}}(2) = {} & 2\, a(y)\, Q \left(1 + \frac{u^2}{Q^2} \right) \left(\overline{\frac{\partial u'}{\partial x}\frac{\partial u'}{\partial x}} + \overline{\frac{\partial u'}{\partial y}\frac{\partial u'}{\partial y}} + \overline{\frac{\partial u'}{\partial z}\frac{\partial u'}{\partial z}} \right) \\ & + 4\, a(y) \left(\frac{u\, v}{Q} \right) \left(\overline{\frac{\partial u'}{\partial x}\frac{\partial v'}{\partial x}} + \overline{\frac{\partial u'}{\partial y}\frac{\partial v'}{\partial y}} + \overline{\frac{\partial u'}{\partial z}\frac{\partial v'}{\partial z}} \right) \\ & + 2\, a(y)\, Q \left(1 + \frac{v^2}{Q^2} \right) \left(\overline{\frac{\partial v'}{\partial x}\frac{\partial v'}{\partial x}} + \overline{\frac{\partial v'}{\partial y}\frac{\partial v'}{\partial y}} + \overline{\frac{\partial v'}{\partial z}\frac{\partial v'}{\partial z}} \right) \\ & + 2\, a(y)\, Q \left(\overline{\frac{\partial w'}{\partial x}\frac{\partial w'}{\partial x}} + \overline{\frac{\partial w'}{\partial y}\frac{\partial w'}{\partial y}} + \overline{\frac{\partial w'}{\partial z}\frac{\partial w'}{\partial z}} \right) \end{aligned} \tag{4.14}$$

This approach required the evaluation of velocity correlations and turbulent strain rates. To account for viscous effects at small scales (4.14), the dissipative correlation, $\overline{\frac{\partial u_i'}{\partial x_k}\frac{\partial u_j'}{\partial x_k}}$, was modelled using [4.15], following the recommendation of Hanjalic and Launder (1976).

$$\nu \overline{\frac{\partial u_i'}{\partial x_k} \frac{\partial u_j'}{\partial x_k}} = \frac{\overline{u_i' u_j'}}{k} \varepsilon \tag{4.15}$$

Unlike the transport of momentum and TKE, the zero- and first-order terms of both the large- and small-scale contributions to the transport of the TKE dissipation rate are zero. Moreover, when the TKE is much smaller than the kinetic energy of the mean flow and isotropy is assumed, the second-order small-scale approximation reduces to that used in conventional RANS k–ε canopy models ($\beta_p = 0$; see [2.12]).

4.3 Numerical techniques

The governing flow equations (2.1)–(2.7) were solved for turbulent flow under a neutrally stratified atmosphere using VENTOS-2D. The terms related to the WTR canopy in the momentum, turbulent kinetic energy (k), and dissipation rate (ε) equations were incorporated through (4.5), (4.6), (4.10), (4.11), (4.13), and (4.14).

To assess the accuracy of the WTR approach, simulations were carried out for three reference cases previously examined by Lopes et al. (2013, 2016): a horizontally homogeneous canopy (Shaw and Schumann, 1992), a forest edge (Yang et al., 2006b), and a forested hill (Dupont et al., 2008). The computational domain, mesh resolution, and numerical parameters (Table 4.1) followed those used by Lopes et al. (2013, 2016). The streamwise and vertical mesh resolutions were denoted by Δx and Δz, respectively, while U_b and z_0 represented the reference wind speed and roughness length. The characteristic hill length and height were set to $L = 84$ m and $H = 30$ m.

Periodic boundary conditions were applied in the streamwise direction, with a rough-wall condition at the ground and a free-slip condition at the domain top (Lopes et al., 2013). Alongside the WTR approach, the canopy models developed by Lopes et al. (2013) and Liu et al. (1996) were also used for comparison.

Table 4.1: Numerical parameters

Parameters	Homogeneous	Forest edge	Forested hill
h_c(m)	20	7.5	10
Domain size	$9.6h_c \times 3.0h_c$	$38.4h_c \times 6.2h_c$	$300h_c \times 20h_c$
U_b(m s^{-1})	2	3	2
C_d	0.15	0.2	0.2
Grid nodes	192×98	480×101	849×125
z_0/h_c	1.00×10^{-3}	3.73×10^{-3}	3×10^{-3}
$\Delta x/h_c$	5×10^{-2}	8×10^{-2}	3.5×10^{-1}
$\Delta z_{min}/h_c$	1.25×10^{-2}	1.07×10^{-2}	3.5×10^{-2}
LAI	2.0	2.0	1.6

4.4 Results and discussion

The performance of the WTR approach was assessed based on the mean wind speed, Reynolds shear stress, TKE, and its dissipation rate. The evaluation involved comparisons with LES results from Lopes et al. (2013) and with the RANS canopy models of Lopes and Liu (Papers I and II). The assessment was conducted across three flow configurations of increasing complexity.

To ensure consistency in the analysis, the mean wind speed was normalised by the reference wind speed (U_b), while the remaining variables were scaled using the friction velocity (u_*) at the canopy top. As in the previous chapter, RMSE (3.2) and BIAS (3.3) metrics were used to quantify the quality of the results.

4.4.1 Homogeneous canopy

The streamwise velocity profiles (Figure 4.1a) exhibit a consistent decay within the region of high foliage density across all models. Both the WTR and Liu models tend to underestimate the LES results, while the Lopes model provides a closer match. Despite these differences, all models successfully capture the inflection point near the canopy top.

Larger discrepancies appear in the TKE and shear stress profiles (Figures 4.1b–c). Near the surface ($z/h_c < 0.5$), both the WTR and Lopes models underestimate TKE, with BIAS values of -0.19 and -0.21. In contrast, the Liu model aligns more closely with LES, showing a BIAS of -0.071. Despite being calibrated for this type of flow, the Lopes model is outperformed by the WTR model in replicating the TKE profile. Contrary to the results reported in Lopes et al. (2016), the WTR model underpredicts shear stress near the canopy top, a trend also seen in the Liu model. Above the canopy, however, all models yield similar and accurate shear stress estimates.

Table 4.2: Error indicator of the flow across the homogeneous canopy

Variable	Canopy model	RMSE	BIAS
U/U_b	Liu (1996)	0.079	-0.007
	Lopes (2013)	**0.040**	0.012
	WTR	0.063	**-0.002**
TKE/u_*^2	Liu (1996)	0.341	0.026
	Lopes (2013)	0.423	-0.338
	WTR	**0.248**	**-0.214**
$\overline{u'w'}/u_*^2$	Liu (1996)	0.081	-0.035
	Lopes (2013)	**0.016**	**-0.006**
	WTR	0.084	-0.033

Note: Best and worst values in bold and underlined.

Table 4.2 indicates that no single canopy model consistently outperforms the others. The Lopes (2013) model provides the most accurate predictions for U/U_b and momentum flux, with the lowest RMSE values for both, but tends to substantially underestimate TKE. The WTR model excels in predicting TKE, achieving both the lowest RMSE and BIAS for this variable,

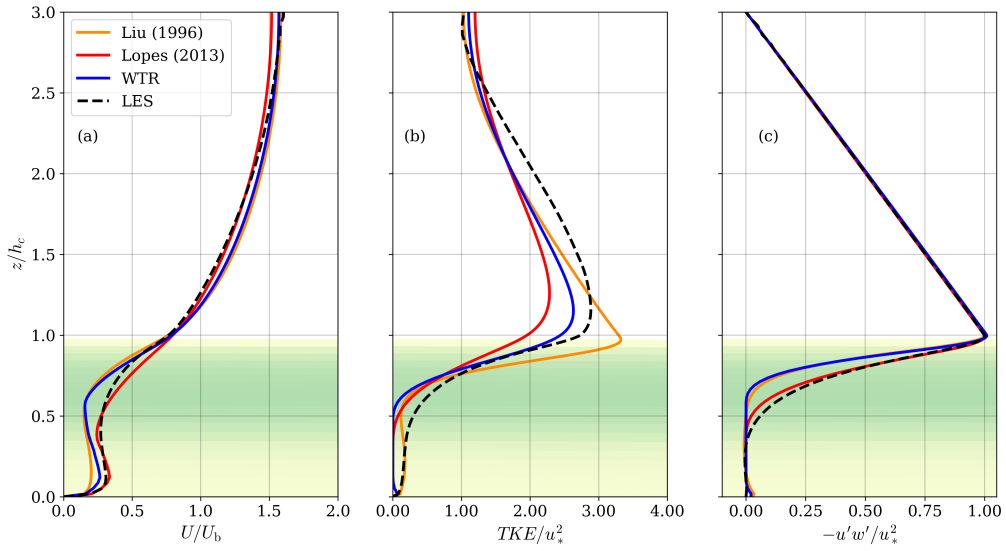


Figure 4.1: Flow across a homogeneous canopy: profiles of RANS $k-\varepsilon$ canopy models and LES: (a) streamwise velocity; (b) turbulent kinetic energy; (c) Reynolds shear stress. The green shading denotes the homogeneous LAD distribution.

and also shows the smallest velocity BIAS, though with a moderate RMSE for U/U_b and the highest RMSE for momentum flux. In contrast, the Liu (1996) model generally produces higher RMSE values across variables, although its momentum flux bias is comparable to that of the WTR model.

Overall, the WTR model provided a good representation of both the mean and turbulent flow fields, with reasonable RMSE and BIAS (Table 4.2), especially when compared to the Lopes model, which was calibrated for this flow scenario.

4.4.2 Forest edge

Flow over a forest edge is a more complex modelling scenario due to the combined effects of vertical and streamwise transport processes. To analyse this evolution, seven streamwise locations were selected—two upstream of and five within the forest (Figure 4.2, Appendix B.2). All results were normalised following Lopes et al. (2013). The main modelling challenge lies in capturing the turbulent field, which is far more sensitive to model assumptions than the mean flow.

Figure 4.2 shows the vertical profiles of mean velocity, TKE, Reynolds shear stress, and dissipation, with corresponding error statistics summarised in Table B.2 (Appendix B.2). WTR delivered the most accurate predictions across wind speed and Reynolds shear stress, closely matching LES results for mean velocity (average RMSE = 0.038, BIAS = 0.005), comparable to Liu. For TKE, Lopes achieved the lowest RMSE (0.241) and BIAS (0.129), although WTR still outperformed Liu (RMSE = 0.297 vs. 0.568; BIAS = –0.217 vs. –0.308). A similar trend was observed for TKE dissipation and Reynolds shear stress, highlighting persistent limitations in Liu's model, which notably overestimated both quantities at $x/h_c = 1$ and 3.

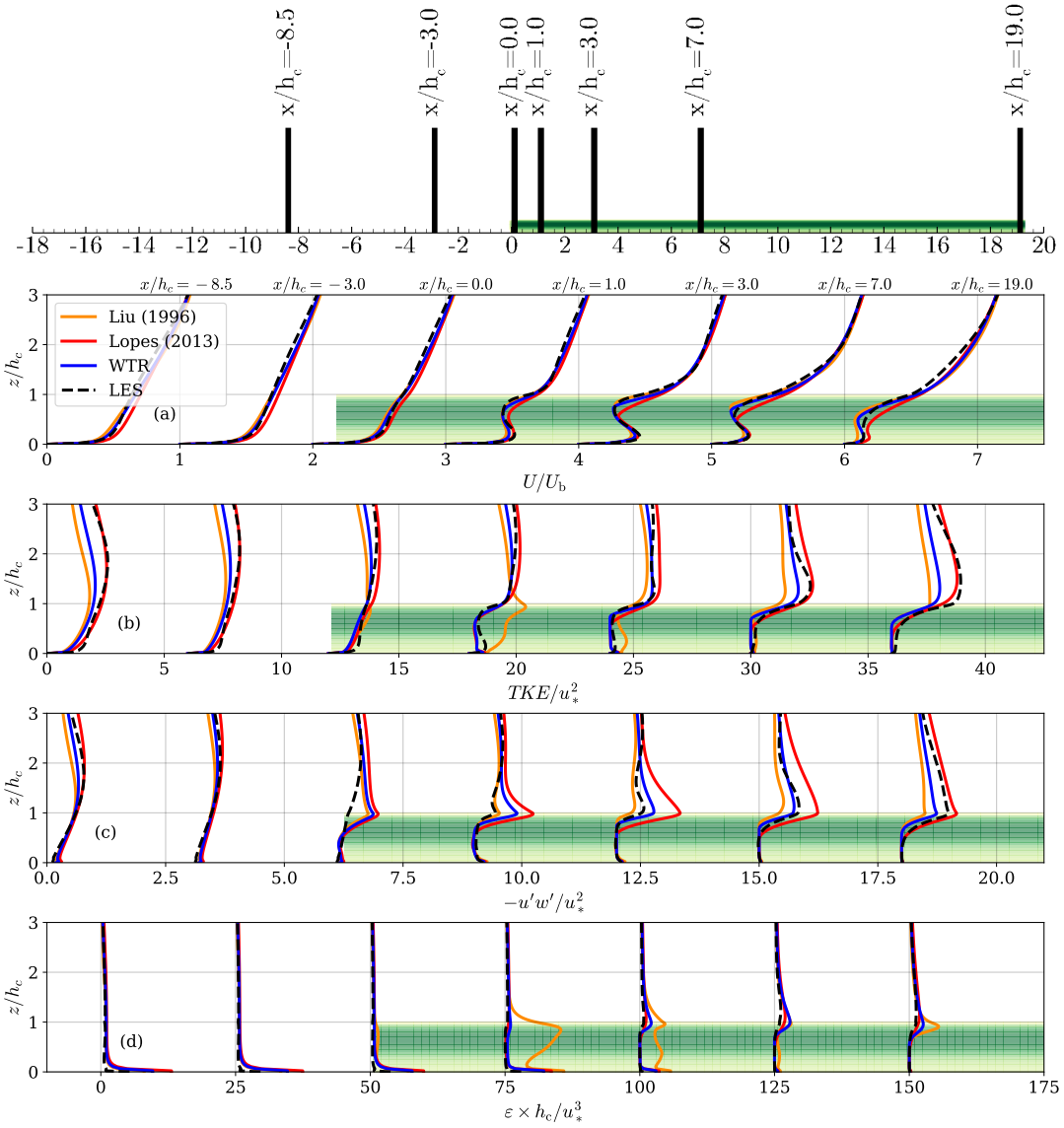


Figure 4.2: Flow across a forest edge: profiles of RANS $k-\varepsilon$ canopy models and LES. Profiles shifted right by 1, 6, 3 and 25 units for clarity: (a) streamwise velocity; (b) turbulent kinetic energy; (c) Reynolds shear stress; (d) turbulent kinetic energy dissipation. The green shading denotes the homogeneous LAD distribution.

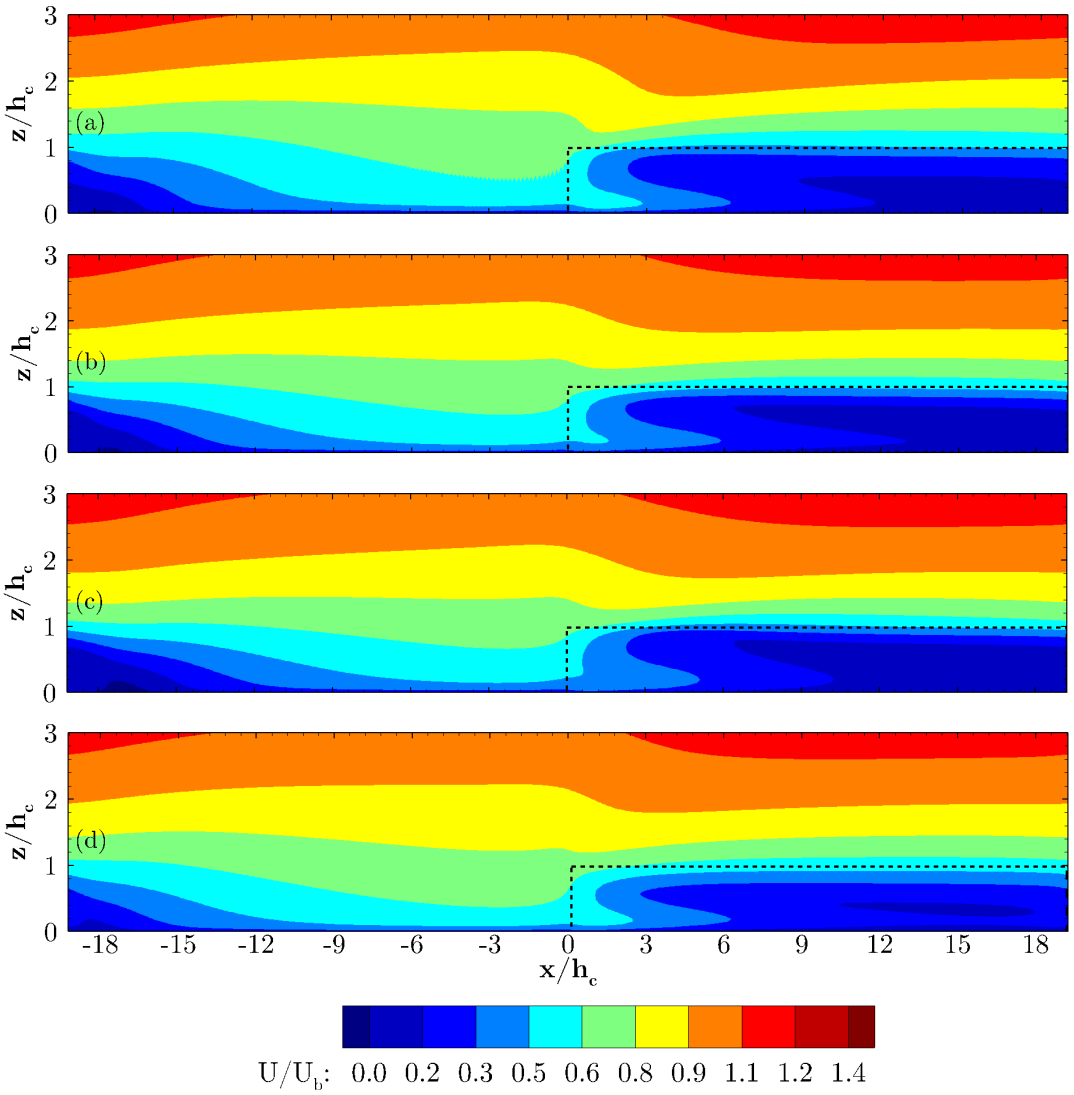


Figure 4.3: Edge case wind speed (U/U_b): (a) LES; (b) WTR; (c) Liu; (d) Lopes (2013).

LES results for the normalised streamwise velocity (U/U_b, Figure 4.3) show a clear wind speed inflexion near the canopy edge, consistent with Yang et al. (2006a). This marks the shift from slower flow inside the canopy to faster flow above and downstream. All models produced similar velocity magnitudes, but the Lopes model showed a stronger acceleration after the edge than the LES. For TKE (TKE/u_*^2, Figure 4.4), Lopes matched the LES pattern and values well, capturing the turbulence peak at the canopy top and its decay downstream. WTR reproduced the overall shape but underestimated values above the canopy, while Liu generally predicted lower TKE except close to the edges. For Reynolds shear stress ($\overline{u'w'}/u_*^2$, Figure B.1), all models reproduced the near-zero values inside the canopy. Above the canopy, Lopes tended capture the shape but overestimate the intensity, whereas WTR and Liu did not follow the LES shape.

To provide a spatial overview, contour plots were used to visualise deviations between RANS models and LES (Appendix B.3). These reveal that both WTR and Lopes overestimated wind speed near the canopy top at $x/h_c \approx 3$ by up to 0.4 $\mathrm{m\,s^{-1}}$ (Figure B.3.1), while Liu

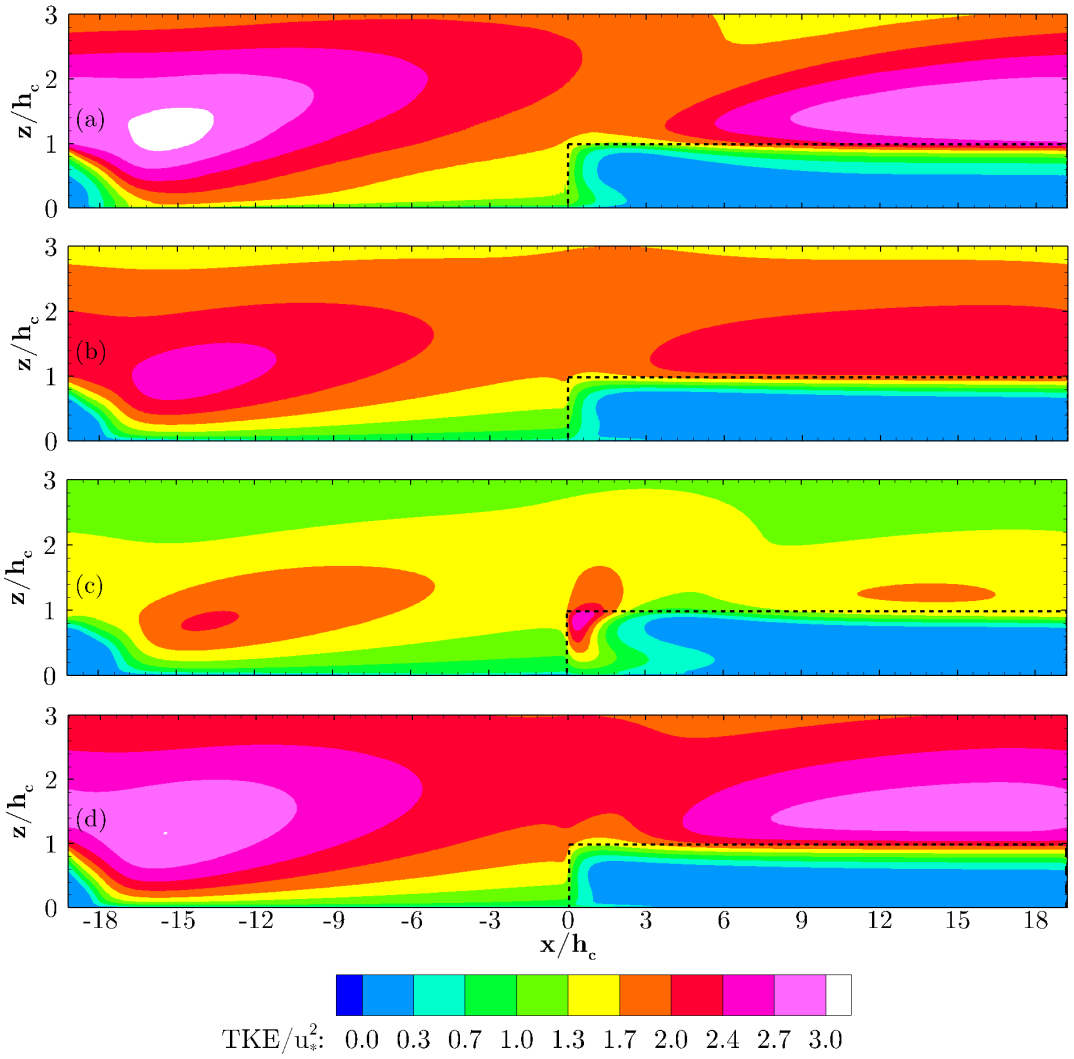


Figure 4.4: Edge case TKE/u_*^2: (a) LES; (b) WTR; (c) Liu; (d) Lopes (2013).

underestimated it below the canopy for $x/h_c < -13$. Among the models, WTR achieved the lowest overall BIAS, whereas Lopes consistently overpredicted. For TKE, WTR and Liu underestimated turbulent energy above the canopy, while Lopes remained within ± 0.1 m^2 s^{-2} (Figure B.3.2). In the case of Reynolds shear stress, WTR aligned best with LES, while Liu and Lopes showed larger discrepancies, with BIAS values exceeding 0.1 m^2 s^{-2} (Figure B.3.3).

Table 4.3 shows the global differences between LES and RANS for mean velocity, TKE, and Reynolds shear stress across the domain. For U/U_b, all models matched the LES average well. WTR had the lowest RMSE (0.043) and a small positive BIAS (0.007), followed by Liu, while Lopes had the largest RMSE (0.061) and a higher positive BIAS (0.035), reflecting its stronger acceleration downstream of the forest edge. TKE showed larger differences: Liu strongly underpredicted turbulence intensity (mean = 1.179 vs. 1.723 in LES; RMSE = 0.716; BIAS = –0.549), Lopes gave the closest match (RMSE = 0.231; BIAS = 0.097), and WTR fell in between, capturing the pattern but overestimating on average (BIAS = 0.361). For Reynolds shear stress, all models reproduced the negative mean values and range. WTR had the smallest

Table 4.3: Edge flow: global differences between LES and RANS

	Model	Mean	Min	Max	stdev	RMSE	BIAS
U/U_b	Liu	**0.743**	-0.056	1.339	**0.367**	0.046	**0.001**
	Lopes	0.777	0.000	**1.348**	0.329	0.061	0.035
	WTR	0.749	**-0.031**	1.334	0.351	**0.043**	0.007
	LES	0.742	-0.024	1.437	0.366	-	-
$\mathrm{TKE}/\mathrm{u}_*^2$	Liu	1.179	0.000	2.627	0.538	0.716	-0.549
	Lopes	**1.819**	0.000	**3.031**	**0.791**	**0.231**	**0.097**
	WTR	1.367	0.000	2.352	0.641	0.468	0.361
	LES	1.723	0.000	3.133	0.834	-	-
$\overline{u'w'}/u_*^2$	Liu	-0.339	-0.769	0.129	0.209	0.209	0.135
	Lopes	-0.619	-1.340	**0.032**	0.371	0.209	-0.139
	WTR	**-0.425**	**-0.931**	0.102	**0.253**	**0.129**	**0.048**
	LES	-0.479	-1.039	0.022	0.296	-	-

Note: The best values are bold, and the worst are in underlined.

RMSE (0.129) and a BIAS close to zero (0.048). Liu and Lopes had the same RMSE (0.209) but with opposite biases—Liu overpredicted and Lopes underpredicted the magnitude. Overall, WTR gave the best balance across the three variables but still underestimated turbulence above the canopy. Liu struggled with TKE, while Lopes was better for turbulence intensity but less accurate for velocity and shear stress.

4.4.3 Forested hill

For flow over a forested hill, wind speed increases as the flow approaches the hill summit and drops on the lee side, where flow separation occurs. This pattern was captured by the LES, WTR, and Liu models, while the Lopes model did not reproduce the recirculation region (Figure 4.5). These findings are in line with those of Lopes et al. (2013), but differ from Lopes et al. (2016), where the WTR model failed to represent the separated flow. Similar wind speed profiles were also reported by Ma et al. (2020), based on LES results. The data presented in Table C.2 (Appendix C.2) supports these observations, showing that both the WTR and Liu models outperformed Lopes in predicting velocity, achieving the lowest average RMSE (0.046) and BIAS (0.003), respectively.

In contrast to the forest edge case—where the Lopes model gave the best TKE predictions—the forested hill scenario showed WTR to be the most reliable in capturing both TKE and its dissipation. At the downstream position $x/L = 1.4$, however, the Liu model aligned more closely with LES for TKE, while Lopes continued to overestimate. For TKE dissipation, Liu also performed well at both $x/L = 0.431$ and $x/L = 1.4$. Regarding Reynolds shear stress, WTR showed good agreement with LES across all locations, while the Lopes model again overpredicted values, repeating the trend observed in the forest edge case. This overestimation likely stems from its known tendency to exaggerate eddy viscosity, as noted by Lopes et al. (2013). In line with these results, Table C.2 further highlights the WTR model's consistent accuracy across second-order flow statistics—TKE, $\overline{u'w'}$, and ε—achieving the lowest RMSE and BIAS values

of 0.338 (–0.060), 0.118 (–0.025), and 0.725 (0.367), respectively. These findings reinforce the model's robustness and reflect improvements over earlier applications, such as those reported in Lopes et al. (2016).

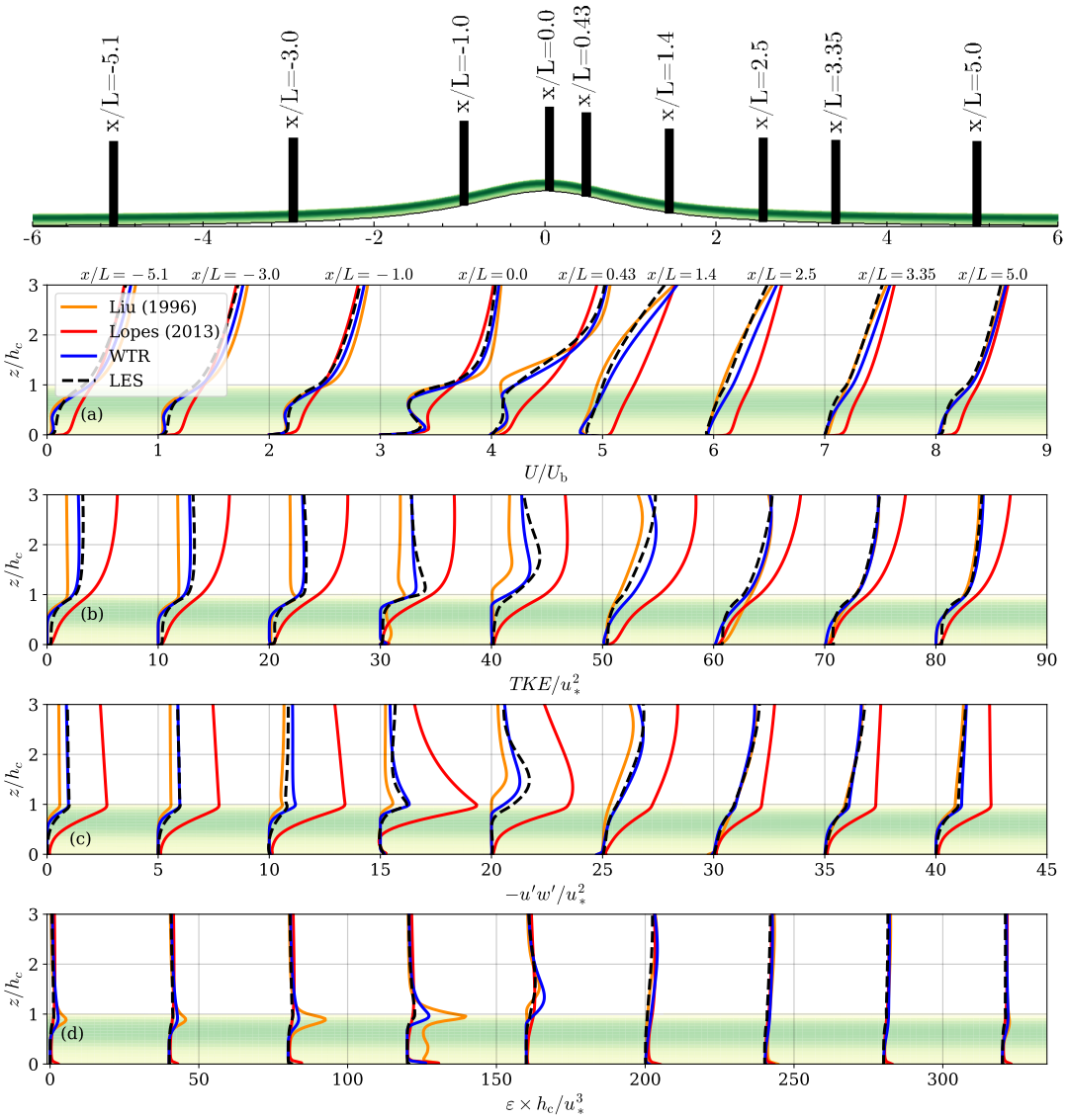


Figure 4.5: Flow across a forested hill: profiles of RANS $k-\varepsilon$ canopy and LES model. Profiles shifted right by 1, 10, 5 and 40 units for clarity: (a) streamwise velocity; (b) turbulent kinetic energy; (c) Reynolds shear stress; (d) turbulent kinetic energy dissipation.

The mean wind speed, turbulent kinetic energy, and Reynolds shear stress over the forested hill exhibit spatial variations that are consistent with established flow behaviour reported in earlier studies (e.g., Belcher et al., 2012, Dupont et al., 2008). On the upwind slope, the mean flow is relatively well predicted, and all RANS models show close agreement with LES for U/U_b (Figure 4.6), indicating limited sensitivity to canopy parameterisation under accelerating conditions. The WTR model showed only a slight underestimation (less than –0.1 $\mathrm{m\,s^{-1}}$, Figure C.3.1), while the Lopes model overestimated wind speed by more than 0.3 $\mathrm{m\,s^{-1}}$ within

the canopy. Differences among models become more pronounced near the hill crest and downstream, where adverse pressure gradients and flow separation dominate. In these regions, the ability to represent the recirculation zone governs model performance, with discrepancies in both the extent and depth of reversed flow leading to systematic deviations in the predicted wind speed within and above the canopy.

For the turbulence field (TKE/u_*^2, Figure 4.7 and $\overline{u'w'}/u_*^2$, Figure C.1), WTR performed best, matching LES patterns on both slopes and achieving smaller errors across all metrics (Figures C.3.2 and C.3.3). The Liu model underestimated TKE and overpredicted Reynolds shear stress, while the Lopes model overestimated TKE and shear stress—especially near the canopy top. These biases reflect differences in how each model represents canopy-induced turbulence production and dissipation, affecting flow predictions over complex terrain.

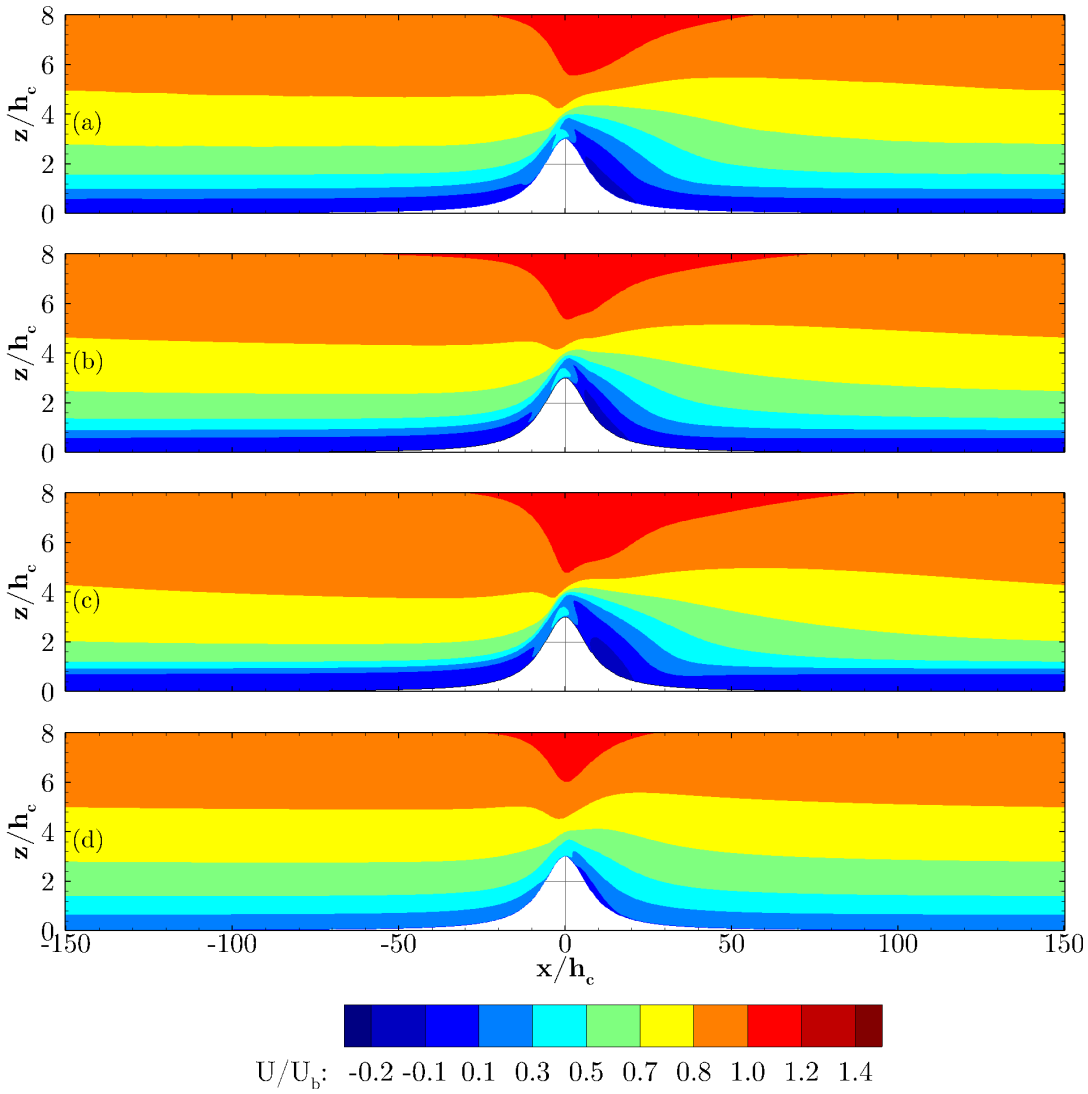


Figure 4.6: Hill case wind speed (U/U_b): (a) LES; (b) WTR; (c) Liu; (d) Lopes (2013).

Compared to the edge case, the WTR model performs more consistently across the hill

site. It matches the LES results well for the mean, minimum, and maximum values of wind speed, TKE, and shear stress (Table 4.4), and has the lowest RMSE and BIAS for all three variables. This agreement holds in key flow regions, including the upwind slope, crest, and lee-side recirculation zone. The Liu model underestimates TKE, mainly because it produces weaker turbulence at the canopy top and less mixing in the separated wake. The Lopes model shows the opposite pattern, overestimating TKE and shear stress.

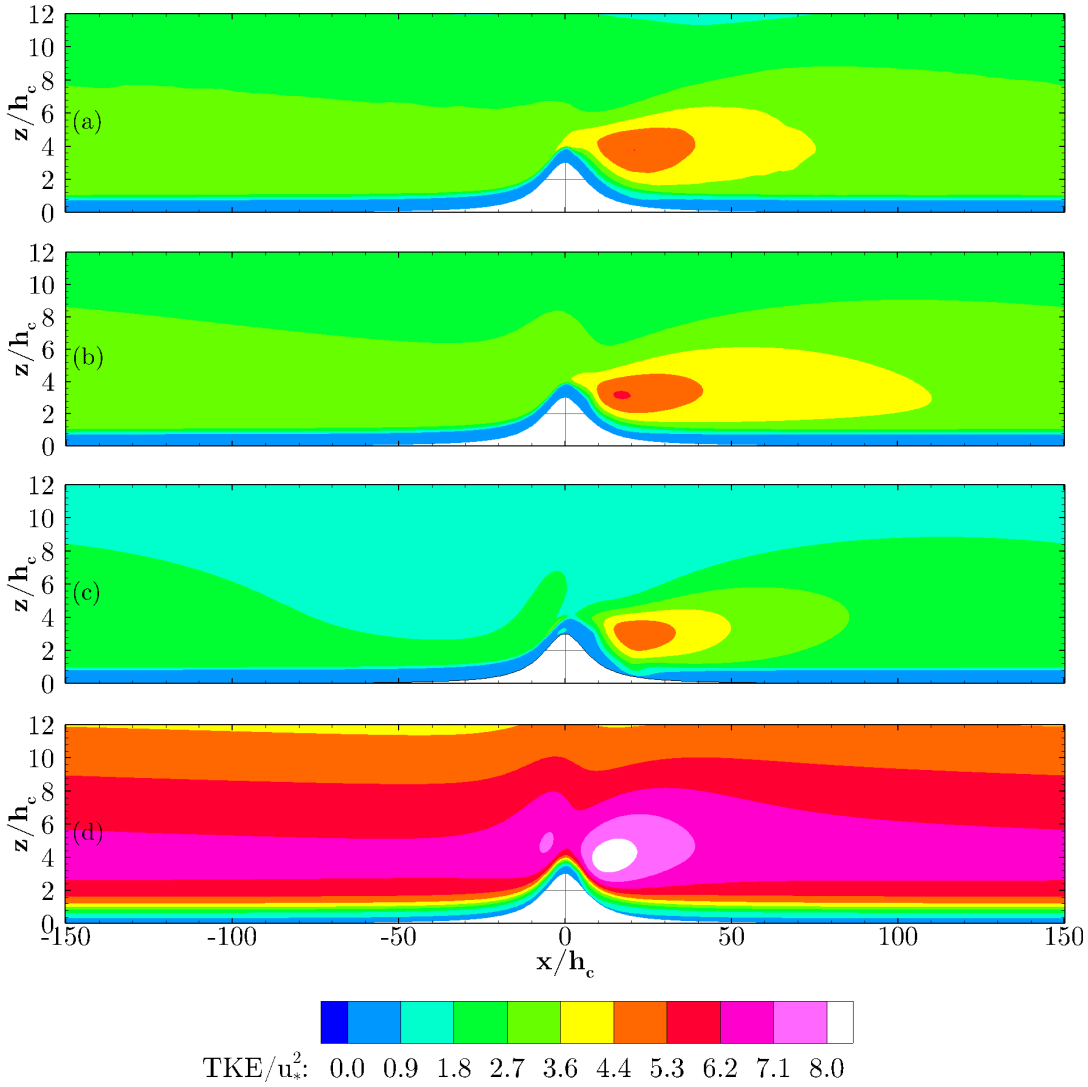


Figure 4.7: Hill case TKE/u_*^2: (a) LES; (b) WTR; (c) Liu; (d) Lopes (2013).

The WTR model handles the short-circuiting of the turbulence cascade inside the canopy more realistically. This helps it balance turbulence production and dissipation in areas with strong shear and separation. Over hills, these effects are strengthened by the interaction between canopy turbulence and pressure gradients caused by the terrain. There is still scope to improve the WTR model by adding higher-order closure terms. As noted by Lopes et al. (2021), third-order terms can help capture turbulent transport and pressure–velocity effects in separation zones, though these are difficult to represent accurately in RANS models. Even without them,

the current second-order version is a clear improvement in robustness and reliability across different terrain types.

Table 4.4: Forested hill: global differences between LES and RANS

	Model	Mean	Min	Max	stdev	RMSE	BIAS
U/U_b	Liu	**0.752**	**-0.183**	1.319	**0.394**	0.065	**0.008**
	Lopes	0.776	-0.0005	**1.376**	0.359	0.077	0.032
	WTR	**0.753**	-0.238	1.347	**0.394**	**0.039**	**0.008**
	LES	0.744	-0.143	1.433	0.415	-	-
TKE/u_*^2	Liu	1.555	0.000	5.218	0.878	0.853	-0.702
	Lopes	4.591	0.000	8.429	1.806	2.534	2.358
	WTR	**2.333**	0.000	**5.393**	**1.154**	**0.251**	**0.100**
	LES	2.233	0.000	5.343	1.104	-	-
$\overline{u'w'}/u_*^2$	Liu	-0.426	-1.906	0.301	0.301	0.226	0.201
	Lopes	-1.656	-4.365	**0.125**	0.903	1.229	-1.079
	WTR	**-0.702**	**-1.982**	0.326	**0.426**	**0.125**	**-0.075**
	LES	-0.627	-1.982	0.050	0.376	-	-

Note: The best values are bold, and the worst are in underlined.

4.5 Conclusion

The second-order terms of the weak turbulence regime (WTR) approach were integrated into the RANS $k-\varepsilon$ model and evaluated in three distinct scenarios: a homogeneous forest, a forest edge, and a forested hill. Performance was assessed against LES data from Lopes et al. (2013) and benchmarked against two RANS models, those of Liu et al. (1996) and Lopes et al. (2013).

The main findings are summarised as follows:

1. The WTR model showed consistent and reliable performance across all test cases, particularly in high-turbulence regions such as the forest edge and the lee of the hill, where it captured the dominant flow structures.
2. Over the forest edge, it closely followed the LES results for wind speed, turbulent kinetic energy (TKE), shear stress, and dissipation rate, with small discrepancies in terms of TKE near the canopy top immediately downstream of the edge.
3. In the forested hill scenario, the WTR model delivered improvements in the recirculation region when compared to reference RANS formulations.

Solving the dissipation equation as proposed by Lopes et al. (2021) led to improved accuracy over earlier results from Lopes et al. (2016), which were based on a time-scale formulation. These results highlight the potential of the WTR approach, particularly if future developments incorporate higher-order terms. Although modelling third-order statistics remains a challenge within the RANS framework, the present second-order formulation already marks a significant step forward in both accuracy and robustness for flows over forested terrain.

CHAPTER 5

Weak Turbulence Regime Approach–3D Flow Modelling

Abstract

The WTR approach was tested for neutral flow over flat forested terrain with a forest edge. Forest effects were included in the VENTOS®/2 CFD model by adding source terms to the $k-\varepsilon$ equations and a momentum body force. The simulations reproduced key conditions at the benchmark site and captured important flow features: reduced wind speed and TKE inside the canopy, a wind jet near the ground, and a high-TKE layer just above the canopy. The WTR performed similarly to the Lopes model, and the results showed that it was well implemented in VENTOS®/2, reproducing well-known features of forest edge flow.

5.1 Introduction

Before applying the WTR model to complex terrain (Chapter 6), it was first tested over flat terrain with a forest-edge configuration. The objective was to evaluate the model's ability to reproduce key flow features observed in real forested environments, including mean wind speed profiles and TKE. Simulation results were compared with anemometer measurements collected downstream of a forest edge on the Island of Falster (Dellwik et al., 2014). For reference, the canopy models assessed in Chapter 3 were also included. Unlike Chapter 3, which examined flow both entering and leaving the forest, the present study focused exclusively on flow approaching the forest edge, with the specific aim of validating the implementation of the three-dimensional WTR model in VENTOS®/2.

The chapter begins with an introduction in Section 5.1, followed by a the 3D formulation of the WTR approach (Section 5.2). An overview of the experimental data and numerical methods are in Section 5.3, results and discussion are presented in Section 5.4, with key conclusions summarised in Section 5.5.

5.2 The weak turbulence regime approach: 3D mathematical formulation

Most of the variables employed herein were introduced previously in Chapter 4, where the foundational aspects of the WTR model and its application to an idealised flow configuration were first presented and discussed in detail.

5.2.1 Transport of momentum

The canopy drag force (4.4) follows the same formulation used in Chapter 4, as defined in equations (4.6) and (4.7), with an additional drag term applied in the vertical direction, corresponding to the z-component of the Cartesian coordinate system.

$$s_W(2) = \frac{U}{Q}\left(\overline{wu}_s - \frac{Uw}{2Q^2}\overline{u}_{sq}\right) \tag{5.1}$$

The directional derivatives of the Reynolds stress tensor components along a specified direction $\mathbf{s} = (s_x, s_y, s_z)$, with $s_z = wU^{-1}$, are given by $\overline{wu}_s = \overline{wu}s_x + \overline{wv}s_y + \overline{ww}s_z$.

The full projection of the Reynolds stress tensor is given by

$$\overline{u}_{sq} = \overline{uu}s_x^2 + 2\overline{uv}s_x s_y + 2\overline{uw}s_x s_z + 2\overline{vw}s_y s_z + \overline{vv}s_y^2 + \overline{ww}s_z^2. \tag{5.2}$$

5.2.2 Transport of turbulent kinetic energy

The canopy terms in the turbulent kinetic energy equation (4.9) are defined as in Subsection 4.2.2, with $\overline{u}_{sq}$ represented as in (5.2).

5.2.3 Transport of the dissipation rate of turbulent kinetic energy

The canopy terms in the TKE dissipation rate (4.12) are split as in 2D version, into large-scale contribution ($S_\varepsilon^{\mathsf{L}}(n)$)

$$
\begin{aligned}
s_\varepsilon^{\mathsf{L}}(2) = {} & \frac{\partial}{\partial x}\left[a(z)\,Q\left(\frac{u^2}{Q^2}+1\right)\right]\frac{\partial\overline{u'u'}}{\partial x} + \frac{\partial}{\partial y}\left[a(z)\,Q\left(\frac{u^2}{Q^2}+1\right)\right]\frac{\partial\overline{u'u'}}{\partial y} \\
& + \frac{\partial}{\partial z}\left[a(z)\,Q\left(\frac{u^2}{Q^2}+1\right)\right]\frac{\partial\overline{u'u'}}{\partial z} + 2\,\frac{\partial}{\partial x}\left[a(z)\,\left(\frac{u\,v}{Q}\right)\right]\frac{\partial\overline{u'v'}}{\partial x} \\
& + 2\,\frac{\partial}{\partial y}\left[a(z)\,\left(\frac{u\,v}{Q}\right)\right]\frac{\partial\overline{u'v'}}{\partial y} + 2\,\frac{\partial}{\partial z}\left[a(z)\,\left(\frac{u\,v}{Q}\right)\right]\frac{\partial\overline{u'v'}}{\partial z} \\
& + 2\,\frac{\partial}{\partial x}\left[a(z)\,\left(\frac{u\,w}{Q}\right)\right]\frac{\partial\overline{u'w'}}{\partial x} + 2\,\frac{\partial}{\partial y}\left[a(z)\,\left(\frac{u\,w}{Q}\right)\right]\frac{\partial\overline{u'w'}}{\partial y} \\
& + 2\,\frac{\partial}{\partial z}\left[a(z)\,\left(\frac{u\,w}{Q}\right)\right]\frac{\partial\overline{u'w'}}{\partial z} + 2\,\frac{\partial}{\partial x}\left[a(z)\,\left(\frac{v\,w}{Q}\right)\right]\frac{\partial\overline{v'w'}}{\partial x} \\
& + 2\,\frac{\partial}{\partial y}\left[a(z)\,\left(\frac{v\,w}{Q}\right)\right]\frac{\partial\overline{v'w'}}{\partial y} + 2\,\frac{\partial}{\partial z}\left[a(z)\,\left(\frac{v\,w}{Q}\right)\right]\frac{\partial\overline{v'w'}}{\partial z} \\
& + \frac{\partial}{\partial x}\left[a(z)\,Q\left(\frac{v^2}{Q^2}+1\right)\right]\frac{\partial\overline{v'v'}}{\partial x} + \frac{\partial}{\partial y}\left[a(z)\,Q\left(\frac{v^2}{Q^2}+1\right)\right]\frac{\partial\overline{v'v'}}{\partial y} \\
& + \frac{\partial}{\partial z}\left[a(z)\,Q\left(\frac{v^2}{Q^2}+1\right)\right]\frac{\partial\overline{v'v'}}{\partial z} + \frac{\partial}{\partial x}\left[a(z)\,Q\left(\frac{w^2}{Q^2}+1\right)\right]\frac{\partial\overline{w'w'}}{\partial x} \\
& + \frac{\partial}{\partial y}\left[a(z)\,Q\left(\frac{w^2}{Q^2}+1\right)\right]\frac{\partial\overline{w'w'}}{\partial y} + \frac{\partial}{\partial z}\left[a(z)\,Q\left(\frac{w^2}{Q^2}+1\right)\right]\frac{\partial\overline{w'w'}}{\partial z}
\end{aligned}
\tag{5.3}
$$

and small-scale contribution ($S_\varepsilon^{\mathsf{s}}(n)$),

$$
\begin{aligned}
s_\varepsilon^{\mathsf{s}}(2) = {} & 2\,a(z)\,Q\left(1+\frac{u^2}{Q^2}\right)\left(\overline{\frac{\partial u'}{\partial x}\frac{\partial u'}{\partial x}} + \overline{\frac{\partial u'}{\partial y}\frac{\partial u'}{\partial y}} + \overline{\frac{\partial u'}{\partial z}\frac{\partial u'}{\partial z}}\right) \\
& + 4\,a(z)\left(\frac{u\,v}{Q}\right)\left(\overline{\frac{\partial u'}{\partial x}\frac{\partial v'}{\partial x}} + \overline{\frac{\partial u'}{\partial y}\frac{\partial v'}{\partial y}} + \overline{\frac{\partial u'}{\partial z}\frac{\partial v'}{\partial z}}\right) \\
& + 4\,a(z)\left(\frac{u\,w}{Q}\right)\left(\overline{\frac{\partial u'}{\partial x}\frac{\partial w'}{\partial x}} + \overline{\frac{\partial u'}{\partial y}\frac{\partial w'}{\partial y}} + \overline{\frac{\partial u'}{\partial z}\frac{\partial w'}{\partial z}}\right) \\
& + 4\,a(z)\left(\frac{v\,w}{Q}\right)\left(\overline{\frac{\partial v'}{\partial x}\frac{\partial w'}{\partial x}} + \overline{\frac{\partial v'}{\partial y}\frac{\partial w'}{\partial y}} + \overline{\frac{\partial v'}{\partial z}\frac{\partial w'}{\partial z}}\right) \\
& + 2\,a(z)\,Q\left(1+\frac{v^2}{Q^2}\right)\left(\overline{\frac{\partial v'}{\partial x}\frac{\partial v'}{\partial x}} + \overline{\frac{\partial v'}{\partial y}\frac{\partial v'}{\partial y}} + \overline{\frac{\partial v'}{\partial z}\frac{\partial v'}{\partial z}}\right) \\
& + 2\,a(z)\,Q\left(1+\frac{w^2}{Q^2}\right)\left(\overline{\frac{\partial w'}{\partial x}\frac{\partial w'}{\partial x}} + \overline{\frac{\partial w'}{\partial y}\frac{\partial w'}{\partial y}} + \overline{\frac{\partial w'}{\partial z}\frac{\partial w'}{\partial z}}\right)
\end{aligned}
\tag{5.4}
$$

5.3 Experimental data and numerical techniques

The site, described in Chapter 3, features an average canopy height of 24 m and an LAI of approximately 6 $m^2\,m^{-2}$. Sonic anemometers were placed: M1 ($1.5h_c$ upstream of the forest edge) and M2 ($1.5h_c$ downstream of the forest edge). Measurements were taken under neutral atmospheric conditions (Dellwik et al., 2014).

The computational domain measured $40h_c$ (streamwise), $5h_c$ (spanwise), and $8h_c$ (vertical). A uniform mesh was used in the x and y directions, while in the z direction, regular spacing extended up to $z = 3h_c = 72$ m, followed by a geometric expansion with a factor of $f_z = 1.0018$. The grid consisted of $120 \times 30 \times 96$ nodes, with spatial resolutions of $4 \times 4 \times 2$ m in the x, y, and z directions, respectively. The inlet conditions, detailed in Chapter 3, employed LAD profiles based on the "scaled ratios" algorithm from Arnqvist et al. (2020), as presented in Paper II. A maximum forest height of 27.5 m was used, with a drag coefficient (C_d) of 0.2 and a homogeneous roughness length of 0.2 m.

5.4 Results and discussion

The simulations were carried out under steady conditions. For streamwise velocity (Figure 5.1a), all models showed comparable performance; however, none accurately captured the observed values at $1.04h_c$ and $0.78h_c$. This discrepancy likely arises from uncertainties in the representation of the leaf area density (LAD) profile and forest height near the edge. In contrast, the Liu model exhibited greater deviation in predicting the turbulent kinetic energy (Figure 5.1b), while the Lopes and WTR models displayed similar behaviour—except below $0.78h_c$, where Lopes underestimated the measurements. This underprediction reflects known limitations in capturing turbulence within this region, as previously noted by Lopes et al. (2013).

Model performance, evaluated using RMSE and BIAS (Table 5.1), showed that all models predicted streamwise velocity with similar accuracy, yielding RMSE and BIAS values around 0.30 and 0.20. For turbulent kinetic energy, the WTR and Lopes models achieved the lowest RMSE (0.004) and BIAS (0.001), while the Liu model produced RMSE value nearly twice as high, indicating a poorer fit to the observations.

Table 5.1: RMSE and BIAS at mast M2.

	Model	RMSE	BIAS
U/U_{ref}	Liu (1996)	<u>0.30</u>	<u>0.18</u>
	Lopes (2013)	**0.29**	0.17
	WTR	**0.29**	**0.16**
$\text{TKE}/U_{\text{ref}}^2$	Liu (1996)	0.007	**-0.001**
	Lopes (2013)	**0.004**	**0.001**
	WTR	**0.004**	**0.001**

Note: The best values are in bold, and the worst are underlined.

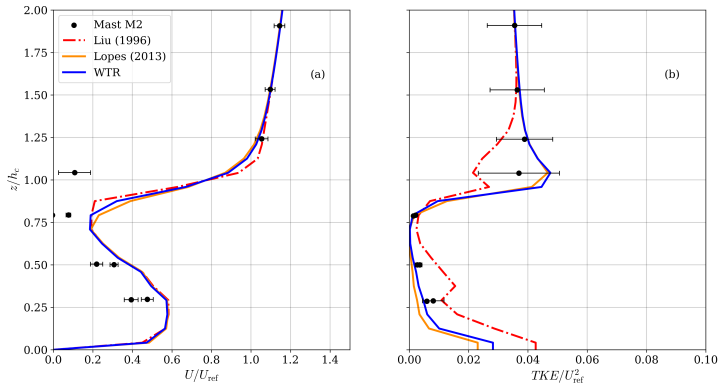


Figure 5.1: Measurements and computational results of flow towards the forest at M2: (a) streamwise velocity; (b) turbulent kinetic energy. The black horizontal lines are the variability bars.

Figure 5.2 shows the spatial distribution of streamwise velocity and TKE for the WTR approach. Results for the other models discussed in Chapter 3 are not shown here. The WTR model produced streamwise velocity patterns consistent with those previously described, showing a reduction in velocity up to $z/h_c \leq 1$ due to canopy drag, followed by acceleration above the canopy and the formation of wind jets in regions with lower leaf density. For TKE, the WTR approach captured the expected decrease within the canopy and an increase above it, inside the internal boundary layer. These trends were also seen in the Lopes model, as noted in Chapter 3.

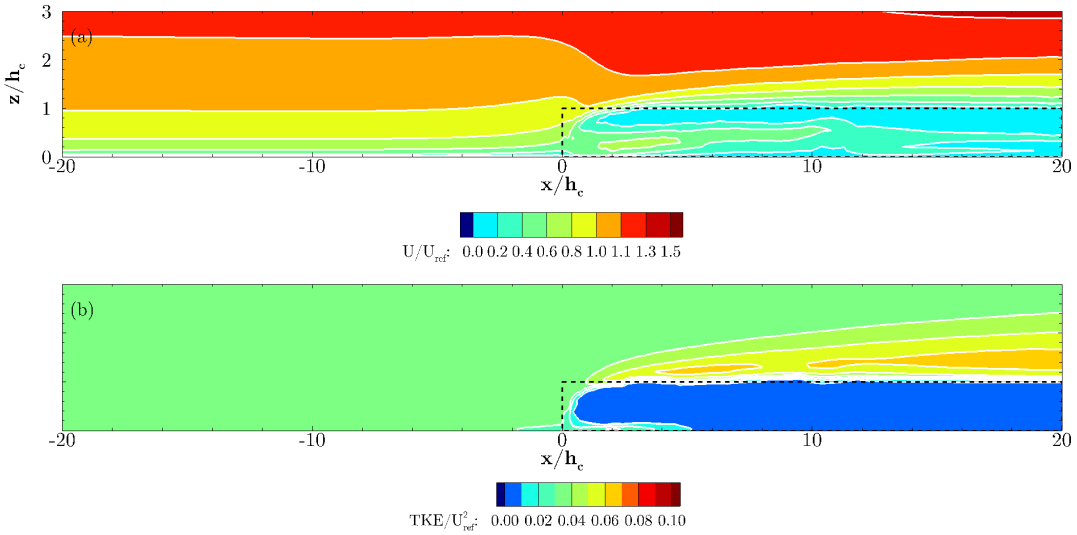


Figure 5.2: Flow towards the forest: mean streamwise velocity (a) and turbulent kinetic energy (b) of WTR model.

In terms of computational time (CPU), the WTR model required approximately the same

processing time as the Lopes and Liu models (8 minutes). Overall, the WTR approach captures the key dynamics of airflow and turbulence within the forest canopy.

5.5 Conclusion

The WTR was evaluated for a neutrally stratified flow over flat terrain covered by a forest in an edge configuration. Additional terms were added to the transport equations for TKE and its dissipation rate ($k - \varepsilon$), as well as a body force in the momentum equations, to represent forest–atmosphere interactions. The results of mean streamwise velocity and TKE were used to evaluate model performance.

The results from the WTR approach are consistent with the finding from Chapter 3. The model results showed some well known features, previous discussed:

- Strong damping of wind speed and TKE inside the forest;
- Wind jet at sub-canopy layer due to low canopy leaf density;
- Presence of high turbulence layer above the canopy.

In summary, the performance of the WTR approach was comparable to the Lopes et al. (2013) model in capturing both mean flow and turbulence characteristics. The results demonstrated that the WTR model represents the key dynamics of streamwise velocity and TKE, striking a balance between accuracy and computational efficiency. Furthermore, the WTR model was successfully implemented within the VENTOS®/2 (Castro et al., 2003) framework. However, further evaluation in more complex topography is required, which will be addressed in the Chapter 6.

CHAPTER 6

Assessing the WTR Model over Complex Terrain: Perdigão Case Study

Abstract

This chapter evaluates the WTR canopy model under quasi-neutral conditions for forested complex terrain, using the VENTOS®/2 CFD code, benchmarked against southwesterly and northeasterly winds (225° and 45°) during the Perdigão 2017 campaign. Two conventional canopy models—Liu and Lopes—and a no canopy model parametrisation case were also used. Key variables analysed include wind speed, turbulent kinetic energy (TKE), and wind direction. Results showed that vegetation affects horizontal wind speed, namely on downhill slopes and in the valley. Wind jets occur in areas with less vegetation.TKE generally increases with height, except in recirculation zones, with a local maximum at 98 m a.g.l. linked to enhanced turbulence above the canopy. The three models reproduced wind speed similarly. However, in terms of TKE, Liu predicted lower values than Lopes, with WTR yielding intermediate results. Topography dominates flow patterns. The WTR model appears to be suitable for complex terrain.

6.1 Introduction

The WTR approach has improved the robustness of the RANS model in handling challenging flow conditions, as demonstrated in Chapter 4. However, its performance in complex environments—such as the Perdigão site (Fernando et al., 2019)—has yet to be fully evaluated. Perdigão was selected for this purpose due to its intricate orography and the availability of detailed forest descriptions from aerial LIDAR surveys (Batista and Palma, 2021, Palma et al., 2020). Most existing modelling studies at this site adopt simplified representations of vegetation, often assuming homogeneous forest cover or uniform tree height (Quimbayo-Duarte et al., 2022, Venkatraman et al., 2023). These simplifications reduce model complexity but neglect spatial variability, which can obscure key flow features driven by canopy gaps, edges, or density variations—features that are crucial for accurately resolving turbulence and momentum exchange (Ma et al., 2020). To address this limitation, the present chapter evaluates the WTR approach over forested complex terrain using a more realistic vegetation representation.

In terms of terrain and flow complexity, the configurations considered in Chapters 3–5 represent relatively simple and idealised cases. In contrast, the Perdigão site introduces a higher level of complexity, characterised by steep terrain, pronounced elevation changes, opposing ridges, and strong three-dimensional flow interactions. These features give rise to accelerated flow along valleys and ridges, persistent separation, and enhanced turbulence production, placing greater demands on the turbulence and canopy modelling approaches.

Following the WTR integration into the VENTOS®/2 CFD framework (Chapter 5), the WTR approach was applied to the Perdigão site to assess its ability to capture essential flow characteristics such as wind speed attenuation, turbulence distribution, and terrain–canopy interactions. For benchmarking purposes, simulations were also performed using the reference RANS $k-\varepsilon$ formulations described in Chapter 5. This study builds on the work of Palma et al. (2020), which modelled the Perdigão terrain with a uniform roughness length (z_0) and without explicit forest parametrisation. In contrast, the present study includes a more detailed representation of surface cover, with a particular focus on the spatial heterogeneity of the forest canopy.

Section 6.1 presents the motivation and objectives of the study. The Perdigão field campaign is introduced in Section 6.2. Section 6.3 outlines the numerical setup, including the computational domain, boundary conditions, and surface cover representation. Results and discussion are provided in Section 6.4, with conclusions in Section 6.5.

6.2 The Perdigão field campaign

The Perdigão site (Palma et al., 2020) is located in Vila Velha de Ródão, Portugal, at UTM coordinates 4396621 m N and 608250 m E in the ED50 datum, Zone 29N. The site comprises two parallel ridges—southwest (SW) and northeast (NE)—rising approximately 250 m above the surrounding terrain, separated by a 1.4 km-wide valley, and extending over 4km in length. The SW ridge has an average elevation of 231 m a.g.l. with a slope of 33.3°, while the NE ridge averages 218 m a.g.l. with a 28.5° slope. The valley floor lies an elevation of approximately 42 m a.g.l. Land cover in the region includes agricultural fields, scrubland, and eucalyptus and pine forests.

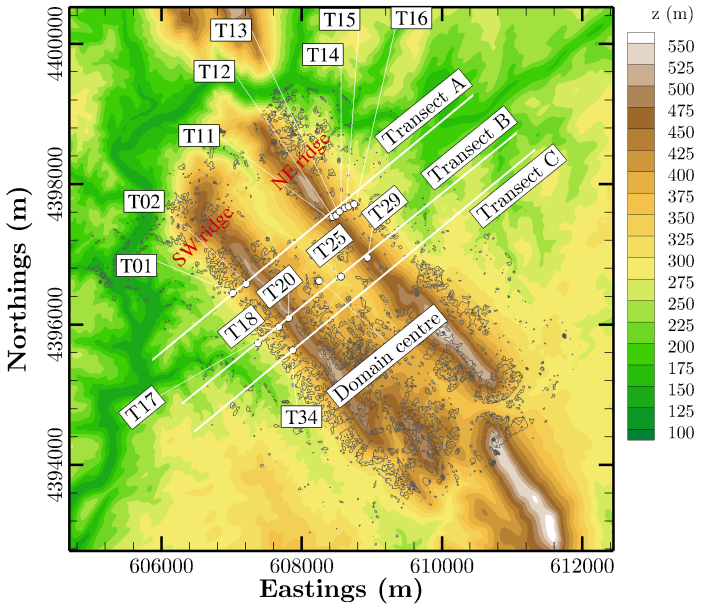


Figure 6.1: Perdigão site overview. Gray contour lines represent forested areas.

The campaign deployed 195 sonic anemometers across 49 towers, along with 26 LIDAR

systems and additional remote sensing instruments, including SODAR/RASS and radiosondes, to characterise the flow and atmospheric conditions (Fernando et al., 2019). The area of interest (AOI)—a 4 km×6 km region between the ridges—was densely instrumented to enable high-resolution atmospheric observations (Figure 6.1).

6.2.1 Measurement data

The Perdigão-2017 campaign, conducted from May 1 to June 15, 2017, offered high-resolution atmospheric data during the intensive observational period (IOP), which forms the basis of this study. The analysis focuses on measurements from sensors mounted on fourteen towers at heights of 100, 60, 30, and 20 m. Wind dynamics at Perdigão are mostly perpendicular to the double-ridge terrain (Fernando et al., 2019), but measurements reveal complex patterns: the wind aligns with the valley axis in the valley and shifts to perpendicular over the ridges (Coimbra et al., 2024).

Table 6.1: Points of interest (POIs) in the PT-TM06/ETRS89 coordinate system and elevation above sea level.

Station number	Station abbreviation	Easting (m)	Northing (m)	Elevation (m)
01	tnw01/T01	32 611.3	4623.2	297.9
02	tnw02/T02	32 804.8	4749.9	392.4
11	tnw11/T11	34 043.0	5696.3	437.0
12	tnw12/T12	34 095.8	5717.1	421.4
13	tnw13/T13	34 140.9	5777.1	384.6
14	tnw14/T14	34 222.8	5816.6	349.0
15	tnw15/T15	34 272.9	5843.3	330.4
16	tnw16/T16	34 349.8	5868.9	306.7
17	tse01/T17	32 960.9	3942.3	252.7
18	tse02/T18	33 260.1	4138.3	372.3
20	tse04/T20	33 394.2	4258.9	473.0
25	tse09/T25	34153.0	4844.8	305.3
29	tse13/T29	34 536.0	5111.6	452.9
34	rsw03/T34	33 569.9	4006.8	472.9

Measurements for this study were taken from instrumented towers along transects A, B, and C (Figure 6.1, Table 6.1), oriented nearly perpendicular to the ridges. The setup included three 20 m towers (tnw01/T01, tnw02/T02, tnw11/T11) with 3D sonic anemometers (RMY8100, CSAT3), seven 30 m towers (tse01/T17, tse02/T18, twn12/T12-tnw16/T16) with CSAT3 and CSI IRGA anemometers, one 60 m tower (rsw03/T34) with a Gill Windtowerer anemometer, and three 100 m towers (tse04/T20, tse09/T25, tse13/T29) with Gill 3D Windtowerer Pro anemometers. All anemometers operated at 20 Hz.

The measurement towers were at key locations: tnw01/T01, tnw02/T02, tse01/T17, tse02/T18, rsw03/T34, and tse04/T20 on the SW ridge; tse09/T25 in the valley; and twn11/T11, twn12/T12 twn13/T13, twn14/T14, twn15/T15, twn16/T16, and tse13/T29 on the NE ridge. Each tower was equipped with temperature and humidity sensors (NCAR SHT75) mounted at six heights

above ground level: 10, 20, 40, 60, 80, and 100 m. For this study, only the minimum and maximum heights (10 and 100 m) were considered. The 20, 30, and 60 m towers were selected due to their close proximity to the forest, while the 100 m towers, which have been widely used in previous Perdigão studies for flow characterisation(Menke et al., 2019, Palma et al., 2020), were included to ensure consistency and comparability.

6.2.2 Atmospheric stability

Neutral stratified atmospheric conditions were determined for each 30-minute averaging period using the Obukhov length (L, [6.1], Table 6.2) calculated at 10 m a.g.l.. The classification followed Wharton and Lundquist (2012), with neutral stability identified using the threshold $|L| > 600$,

$$L = -\frac{\Theta_v \, u_*^3}{\kappa \, g \, \overline{w'\Theta_v'}} \tag{6.1}$$

where $\Theta_v \approx T_v + \frac{g}{C_p} Z$ is the virtual potential temperature, and T_v is the virtual temperature [K] measured by the sonic anemometer. The von Kármán constant is $\kappa = 0.4$, and $u_* = \left(\overline{u'w'}^2 + \overline{v'w'}^2\right)^{1/4}$ represents the friction velocity. The covariance $\overline{w'\Theta_v'}$ corresponds to the kinematic sensible heat flux (Albornoz et al., 2022, Wharton and Lundquist, 2012).

Table 6.2: Period with near-neutral condition at selected POIs for SW winds.

Date (UTC)	Towers	$\overline{U}(\mathrm{m\,s^{-1}})$	$u_*(\mathrm{m\,s^{-1}})$	$\overline{w'\Theta_v'}(\mathrm{K\,m\,s^{-1}})$	L(m)
2017-05-04 23:00-23:30	tnw01/T01	1.716	0.448	-0.045	142
	tnw02/T02	1.734	0.450	-0.038	250
	tse01/T17	2.186	0.456	0.005	-12295
	tse02/T18	1.418	0.288	0.002	-868
	tse04/T20	7.339	0.672	0.022	-989
	tse09/T25	2.036	0.642	-0.006	3235
	tse13/T29	5.489	0.621	0.022	-800
	rsw03/T34	2.870	0.425	0.015	-382

The remaining towers are not listed in Table 6.2 because no wind measurements were available for them during this period. These towers were only used in cases with NE winds, for which it was not possible to identify a near-neutral period to the lack of suitable data. Nevertheless, based on the information in Vilaça (2018) and considering the stability parameter $L = 742$ m at tower tse04/T20, the interval from 2017-05-20 22:30 to 23:00 was selected to represent near-neutral conditions for NE winds.

6.3 Numerical techniques

The simulations used the VENTOS®/2 CFD model (Castro et al., 2003), which solves the RANS equations with $k - \varepsilon$ turbulence model. Canopy effects were included via additional terms in the momentum, TKE, and dissipation rate equations, based on the drag coefficient (C_d), leaf area density ($a(x, y, z)$), and the chosen canopy parameterisation.

Four simulations were performed under near-neutral atmospheric conditions (Subsection 6.2.2; Table 6.2). One excluded canopy parametrisation, while the others applied different parametrisations: Liu et al. (1996), Lopes et al. (2013), and WTR (Chapter 5). The Liu and Lopes models were selected based on previous studies (Paper I and Paper II) on forested flat terrain, with canopy coefficients $\beta_p, \beta_d, C_{\varepsilon 4}$, and $C_{\varepsilon 5}$ defined as in Chapter 3.

6.3.1 Computational domain and inlet conditions

The boundary conditions, domain, and numerical mesh were configured similarly to Palma et al. (2020). The computational domain covered an area of 19 km × 18.8 km, centred at 4396621 m N, 608250 m E (ED50 UTM29N), with the x-axis aligned with the inflow direction. Within this domain, an AOI, of 4 km × 6 km, was defined with a constant horizontal resolution of 20 m, expanding geometrically towards the boundaries. The vertical mesh followed a similar expansion, starting from 2 m at the bottom-most control volume, and constant resolution up to 90 m, expanding above it. The terrain representation within the domain was based on a blend of a 2-m aerial LIDAR survey (ALS) derived Digital Terrain Model, 10-m military charts, and $\sim$ 30-m SRTM data (Palma et al., 2020).

The ground surface was treated as rough, with wall functions used to impose constant tangential Reynolds stress, a logarithmic velocity profile, and near-wall turbulence properties. A zero shear stress condition was set at the upper boundary, and equilibrium profiles for velocity, TKE, and its dissipation were prescribed at the inlet. For SW wind the friction velocity, $u_* = \left(\overline{u'w'}^2 + \overline{v'w'}^2\right)^{1/4}$, was derived from measurements, with a representative value of $u_* = 0.4\ \mathrm{m\,s^{-1}}$ assumed for near-neutral conditions (Table 6.2) and applied uniformly throughout the domain. For NE wind, the value $u_* = 0.25\ \mathrm{m\,s^{-1}}$, as used in Palma et al. (2020), was retained.

6.3.2 Terrain coverage

The ALS was conducted on 15 March 2015 (Palma et al., 2020). The survey was carried out at an altitude of 500 m using a TopEye system equipped with a camera mounted on a helicopter, covering an area of approximately 22,071,075 $\mathrm{m^2}$. The resulting point cloud contained approximately 993,198,375 points, with an average density of 45 points/$\mathrm{m^2}$ across the project area and 12.6 points/$\mathrm{m^2}$ when limited to ground-classified points (Batista and Palma, 2021, Palma et al., 2020).

After filtering the ALS data to remove power lines and buildings (Batista and Palma, 2021), the LAD distribution used in the simulations was defined at a horizontal resolution of 10 m and a vertical resolution of 1 m, following the methodology of Arnqvist et al. (2020). This distribution was then resampled onto the computational mesh in both directions while ensuring conservation

of the total LAI (Figure 6.2b). Figure 6.2a illustrates the heterogeneity of the Perdigão forest, characterised by relatively short trees with an average height of 9.8m (considering only areas where $h_c \geq 5$ m) and a maximum of 30 m, although such tall trees are rare. Towers T14, T15, and T16 are located in areas where tree height falls below 5m. The site is also characterised by a relatively low LAI, with a mean of 0.64, a standard deviation of 0.9, and a maximum of 8.86. Notably, the same towers (T14, T15, and T16) are situated in regions where LAI remains below 0.8. The LAD profile (Figure 6.2c) corresponds to the site-average vertical distribution, along with its standard deviation.

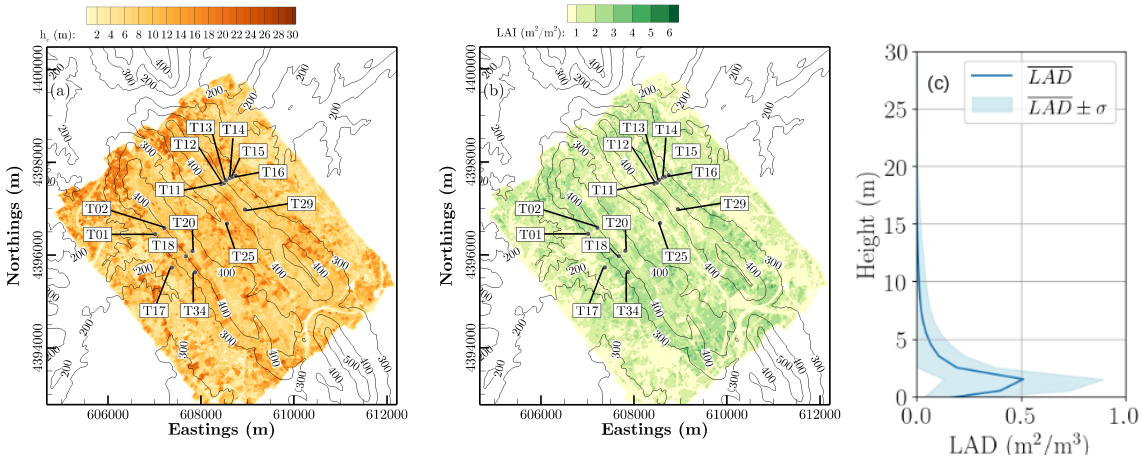


Figure 6.2: Forest characteristics over the AOI: (a) Tree height (h_c), (b) Leaf area index (LAI) and (c) Leaf area density (LAD).

A constant roughness length of $z_0 = 0.1$ m was applied across the domain, following Palma et al. (2020), except in tree-covered areas, where $z_0 = 0.03$ m was used. A drag coefficient of $C_d = 0.15$ was assumed, consistent with values reported by Bannister et al. (2022) for mixed vegetation (shrubs, pine, and eucalyptus). This value also aligns with estimates from measurements using $C_d = (u_*/U)^2$ (Wyngaard, 2010).

6.4 Results and discussion

Given the ALS coverage, the canopy is expected to influence the flow mainly in the central part of the domain. For SW winds, the main differences between the models (Figures 6.3a1, b1, and c1) at 17 m a.g.l.—around twice the average canopy height ($2h_c$)—appear along the upwind slope of the SW ridge. In this region, the Liu model predicts higher velocity deficits, while the Lopes and WTR models show similar results. However, no towers were installed in this area, so it was not possible to directly validate the model predictions. Wind jets (blue areas) appear in similar locations across all models, especially in the valley and on the downwind slope of the NE ridge, likely due to lower vegetation. At 98 m a.g.l. (Figures 6.4a1, b1, and c1), the canopy no longer affects the upwind slope of the SW ridge. Instead, flow differences are only seen on the downwind side, where all models produce a similar pattern.

For TKE at 17 m a.g.l. (Figures 6.3a2, b2 and c2), the canopy models predicted higher values (blue regions) across most areas, except where flow recirculation is likely. The Lopes

model showed the widest extent of elevated TKE, followed by WTR, which is consistent with the findings discussed in Subsection 4.4.3. This overall trend also aligns with results from previous studies over simple terrain (Papers I and II). In contrast, the Liu model tended to predict less TKE. At 98 m a.g.l. (Figures 6.4a2, b2 and c2), the blue contours became more pronounced—particularly for the Lopes model—indicating increased TKE from canopy effects, likely linked to enhanced turbulence within the IBL above the canopy.

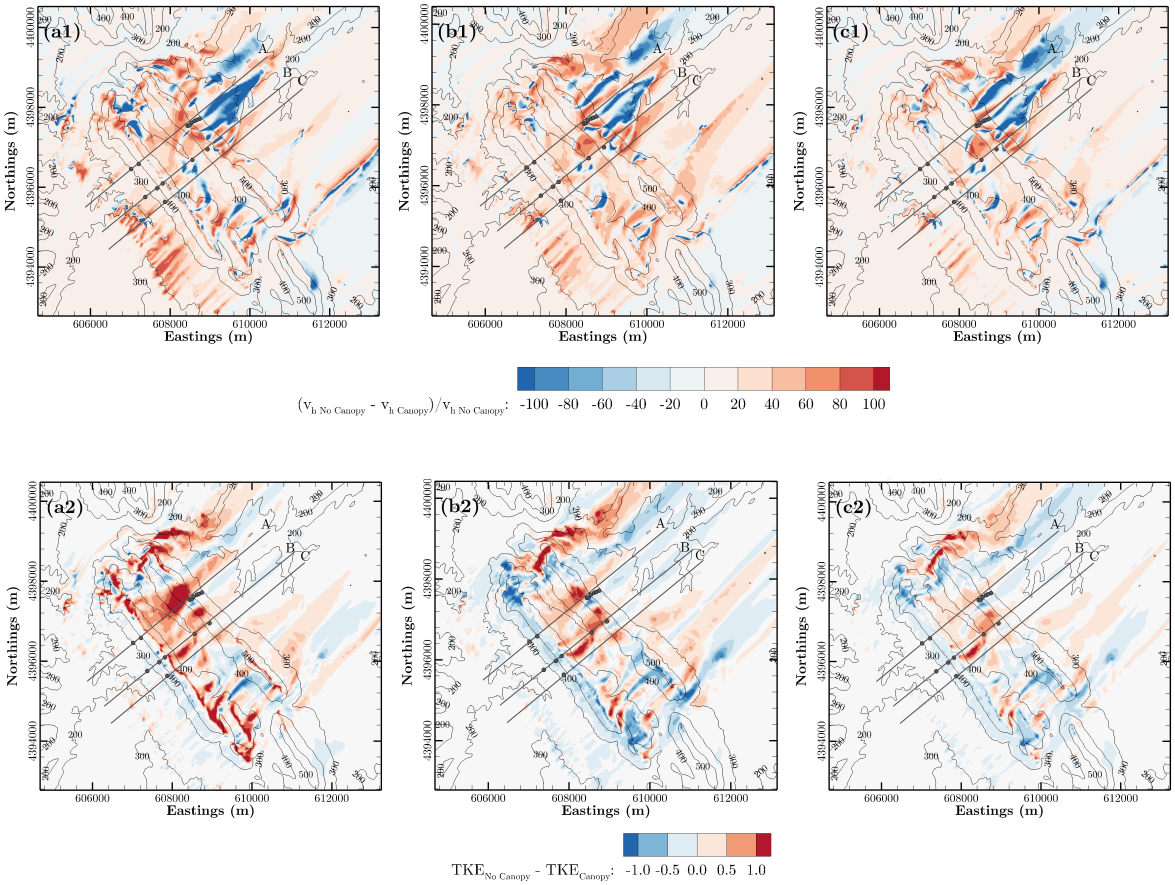


Figure 6.3: Velocity deficit ($(V_{h\ \text{No Canopy}} - V_{h\ \text{Canopy}})/V_{h\ \text{No Canopy}} \times 100$ %) and turbulent kinetic energy difference ($TKE_{\text{No Canopy}} - TKE_{\text{Canopy}}$, in $\text{m}^2\,\text{s}^{-2}$) at 17 m a.g.l. for SW winds, highlighting the effects of the forested regions. The upper row (a1–c1) shows the velocity deficit, and the lower row (a2–c2) shows the turbulent kinetic energy difference for: (a) Liu; (b) Lopes; (c) WTR. Transects A, B, and C are shown. Grey dots mark the tower locations along each transect, consistent with Figure 6.1, and black labels indicate the terrain elevation.

A pronounced recirculation zone developed behind the SW ridge along transect A and B (Figures 6.5 and 6.7), accompanied by a reduction in mean wind speed. This pattern highlights how canopy effects propagate through the vertical structure of the flow. The Liu model predicted a longer recirculation region than any other model. Both transects A and B indicate that towers tnw11/T11–tnw16/T16 and tse09/T25 lie within this recirculation zone and are therefore not suitable for evaluating canopy model performance. The recirculation zone on the downwind side of the NE ridge, along transect B became less pronounced, indicating that the presence of vegetation may have altered where and how the flow slows down across the terrain. Results

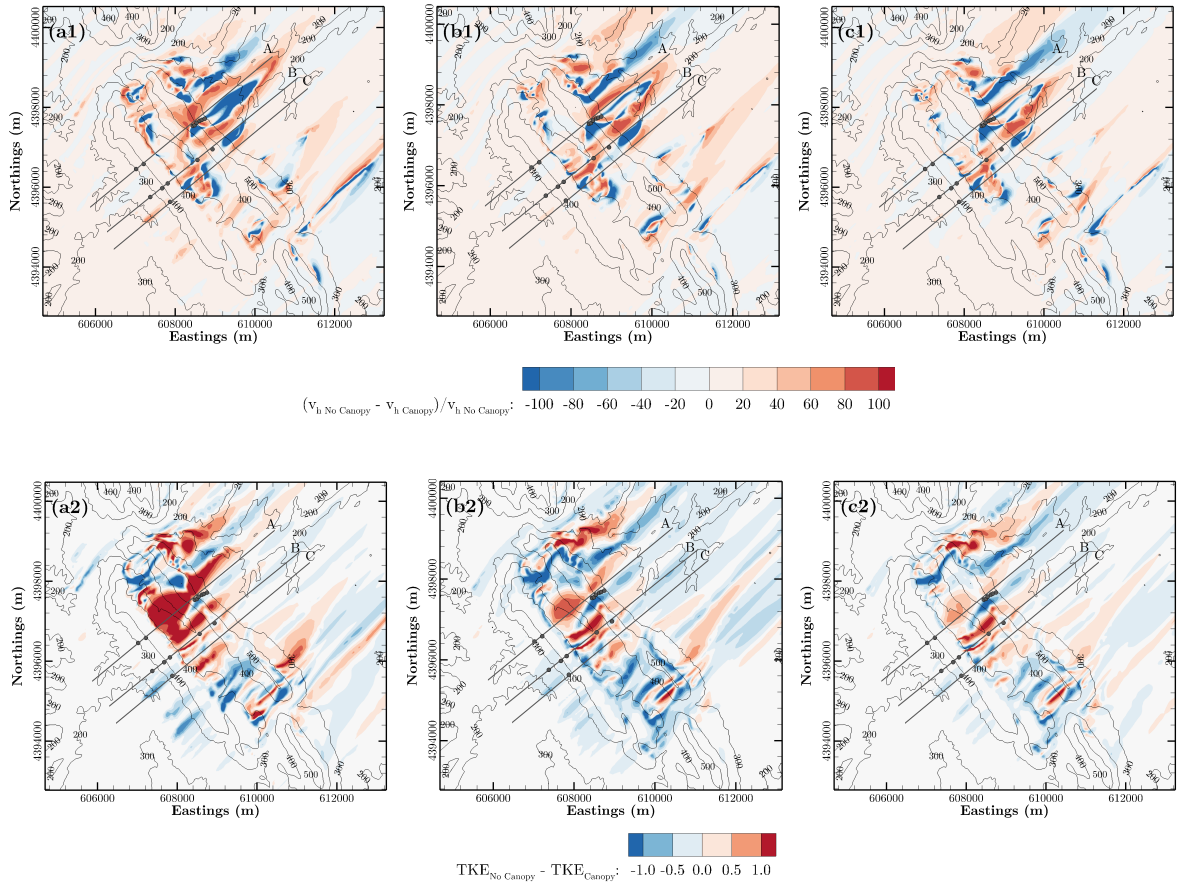


Figure 6.4: Velocity deficit ($(V_{h\ \text{No Canopy}} - V_{h\ \text{Canopy}})/V_{h\ \text{No Canopy}} \times 100$ %) and turbulent kinetic energy difference ($TKE_{\text{No Canopy}} - TKE_{\text{Canopy}}$, in $\text{m}^2\,\text{s}^{-2}$) at 98 m a.g.l. for SW winds, highlighting the effects of the forested regions. The upper row (a1–c1) shows the velocity deficit, and the lower row (a2–c2) shows the turbulent kinetic energy difference for: (a) Liu; (b) Lopes; (c) WTR. Transects A, B, and C are shown. Grey dots mark the tower locations along each transect, consistent with Figure 6.1, and black labels indicate the terrain elevation.

from Menke et al. (2019) along the same transects A and B reported recirculation occurring 51% of the time, mainly for SW winds with speeds above 8 $\mathrm{m\,s^{-1}}$, conditions that correspond closely to the present simulation. Overall, in contrast to the Liu model, both the Lopes and WTR models exhibited a similar recirculation pattern. However, this zone could not be validated at the time of the study. The behaviour along Transect C closely resembled that of Transect B and is therefore not shown.

Vertical profiles along transects A and B showed that the canopy models improved the results near ground-level measurement positions (Figures 6.6 and 6.8). At tnw01/T01, the WTR, Lopes, and Liu models accurately predicted the wind speed at 10 m a.g.l., with negligible differences in TKE. At tnw02/T02, the simulated flow accelerated more than observed, although the transport of the high-TKE layer from the upwind trees was evident in both the WTR and Lopes models, resulting in values closer to the measurements. Wind direction remained nearly constant with height, and all canopy models reproduced this trend, indicating that the flow alignment was well represented despite the differences on wind speed. A similar improvement was observed at tse01/T17, tse02/T18, and tse04/T20, where the WTR and especially the Lopes model closely matched the TKE profiles, while wind direction stayed aligned with the measurements throughout the canopy and above. At tse13/T29, the canopy models produced less flow acceleration compared to the simulation without a canopy, consistent with a more pronounced recirculation zone predicted in the valley; nevertheless, wind direction deviations were small, reflecting the dominant SW flow orientation. A similar analysis at the Perdigão site is presented in Venkatraman et al. (2023), where, using a different period and assuming a homogeneous LAD and h_c, the simulations with a canopy approach underestimated the measurements.

For NE winds, both the forest density and tree height are lower compared to the SW side (Figures 6.2a and b). As a result, the forest impact on the velocity deficit and TKE differences at 17 m a.g.l. was less pronounced on the uphill side (Figure 6.9), with most of the effects observed on the downhill side of the NE ridge. All three models exhibited similar patterns, except in the upper region on the northern side, where the WTR model predicted higher wind speeds than the others. At 98 m a.g.l., an increase in TKE was also observed (Figure 6.10), consistent with the behaviour seen under SW winds. Overall, the velocity deficit and TKE patterns predicted by the WTR model at both 17 and 98 m a.g.l. closely matched those from the Lopes and Liu models. This similarity is related to the lower vegetation density and shorter tree height in NE uphill side.

Results of streamwise wind speed along transects A and B (Figures 6.11 and 6.13) show that applying canopy parametrisation noticeably expands the recirculation zone for transect B compared to simulations without canopy effects. For transect A, differences were negligible, mainly due to lower vegetation on the uphill side. Among the models tested for transect B, the Liu formulation predicted a taller recirculation zone, suggesting stronger canopy-induced flow separation and vertical mixing. In contrast, the WTR and Lopes models produced similar patterns in both the horizontal extent and vertical structure of the recirculation zone, indicating comparable sensitivity to canopy effects. Towers located further downstream along the recirculation zone were excluded from the model evaluation to avoid bias from secondary flow features, such as flow reattachment, terrain-induced acceleration, and valley-driven channeling, which are not directly associated with the primary canopy-induced recirculation. Therefore, only towers tnw11/T11 to tnw15/T15 and tse13/T29 were included in the performance assessment. Tower tnw16/T16 was not shown due to its similarity with tower tnw15/T15.

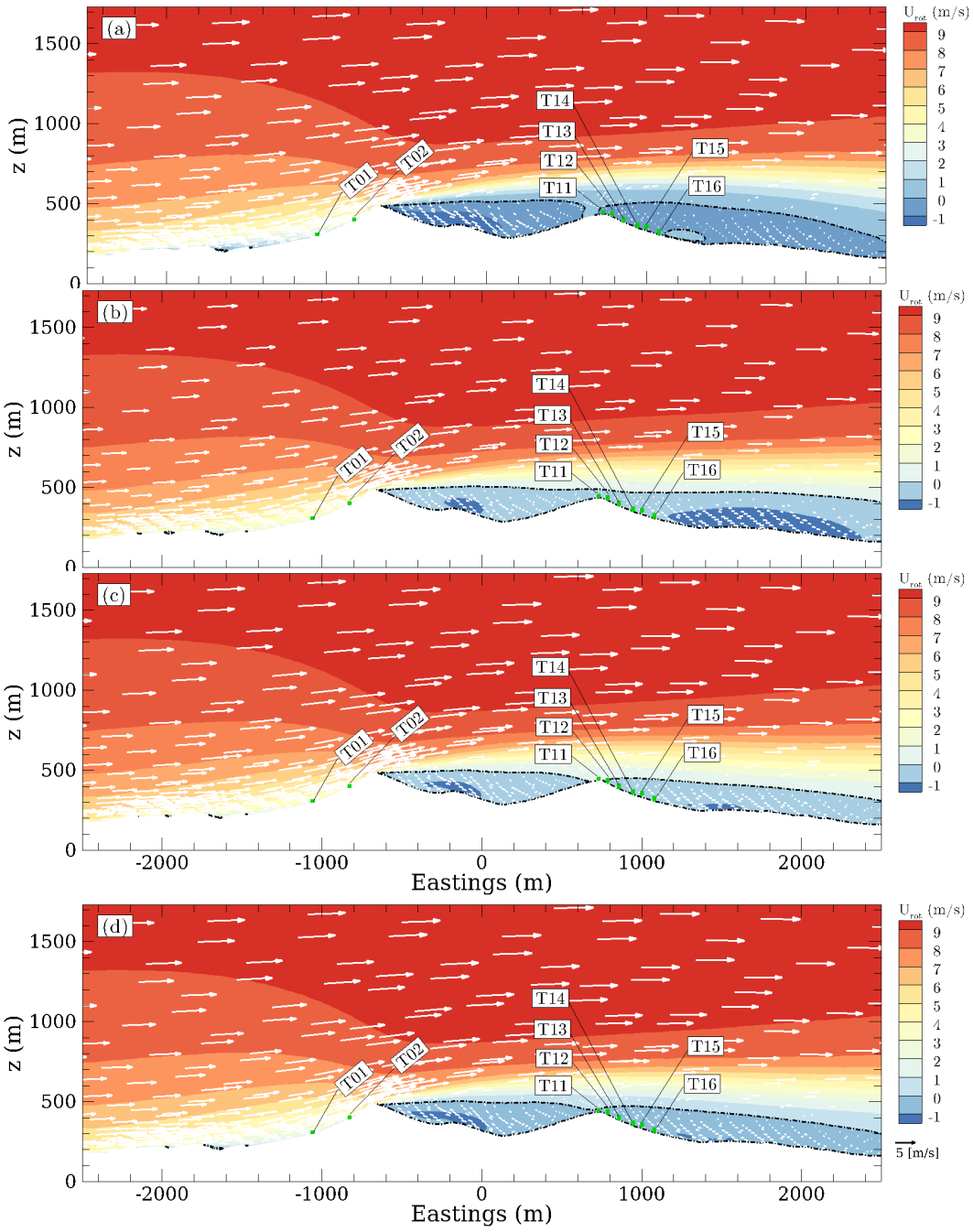


Figure 6.5: Streamwise wind along transect A for SW winds: (a) without canopy parametrisation, (b) Liu, (c) Lopes and (d) WTR model.

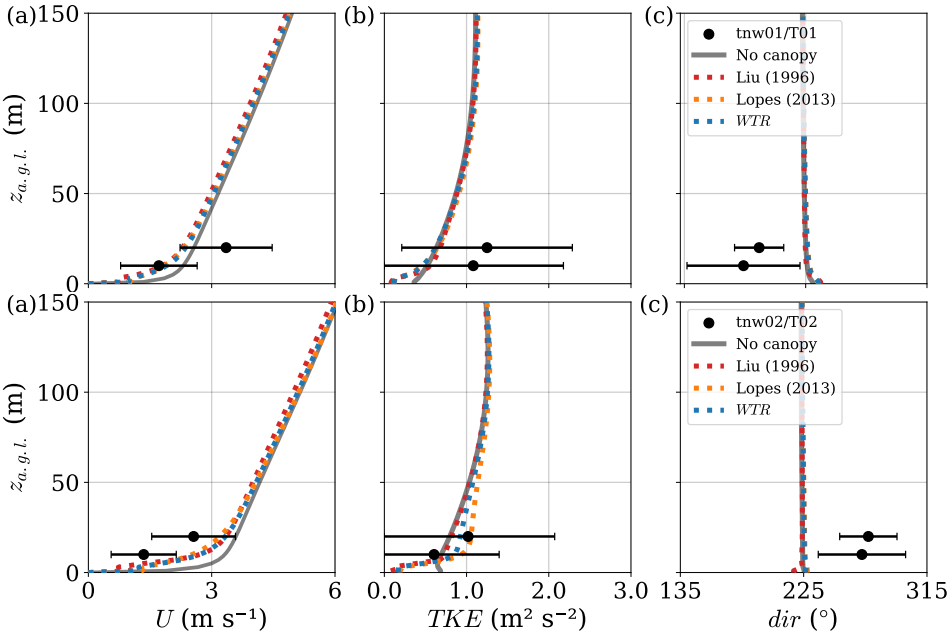


Figure 6.6: SW wind measurements and computational results for transect A: (a) wind speed; (b) turbulent kinetic energy; (c) wind direction. Black horizontal lines indicate the standard deviations of the measurements.

The wind profiles along transect A (tnw11/T11–tnw15/T15; Figure 6.12) and transect B (tse13/T29; Figure 6.14) show good agreement in wind speed among the canopy models. In contrast, simulations without canopy parametrisation tend to overestimate wind speed at towers tnw11/T11 to tnw14/T14. For TKE, all canopy models performed reasonably well, although the Lopes model generally overestimated measurements, while Liu gave a better prediction followed by WTR. Regarding wind direction, the measurements at towers tnw13/T13 to tnw15/T15 showed shifts not captured by any model. Overall, large differences between the models were not expected due to lower LAD and shorter tree height. At tower tse13/T29 (Figure 6.14), only the Liu model was able to replicate the shape of the measured TKE profile.

Collectively, the analysis of the SW and NE wind cases shows that forest effects are most noticeable on the downhill slopes, within the valley, and in specific regions of the NE ridge under SW winds—and vice versa—where terrain-induced acceleration interacts with vegetation drag. In contrast, most towers along transects A, B, and C show limited sensitivity to forest representation, highlighting the dominant influence of topography on local flow dynamics, as also observed by Arroy et al. (2014).

From the perspective of the canopy models, all three exhibited similar performance in reproducing wind speed when compared with measurements. However, differences emerged in the TKE predictions: the Liu model acted more as a sink, the Lopes model tended to predict higher TKE, and the WTR model provided intermediate results. Overall, the models demonstrated comparable performance against observations. Nevertheless, it is important to emphasise that these results suggest the WTR model is well suited for application in more complex terrain. It offers a good balance between accurately representing both the mean flow and second-order statistics over forested regions, without relying on fixed model constants, unlike conventional

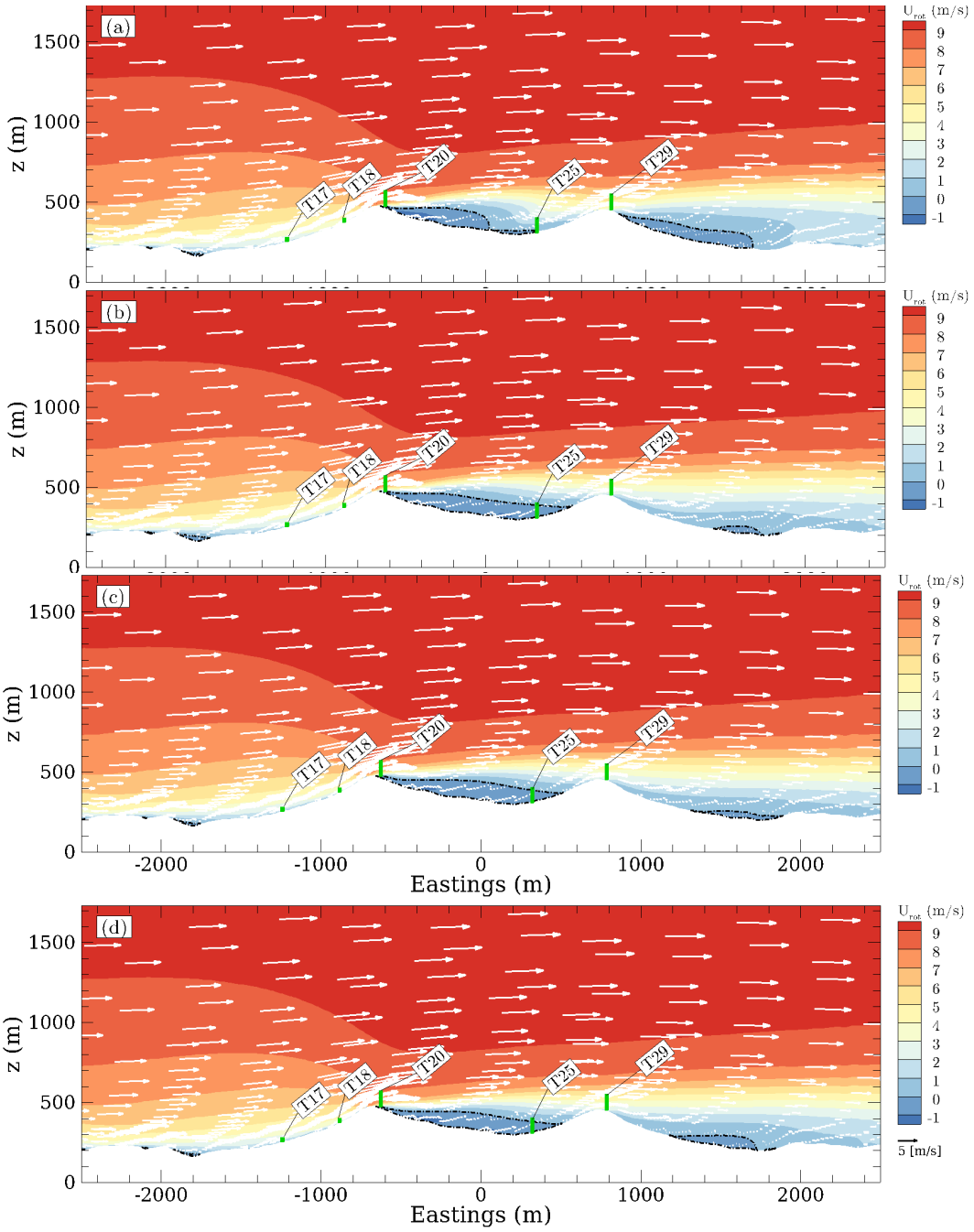


Figure 6.7: Streamwise wind along transect B for SW winds: (a) without canopy parametrisation, (b) Liu, (c) Lopes and (d) WTR model.

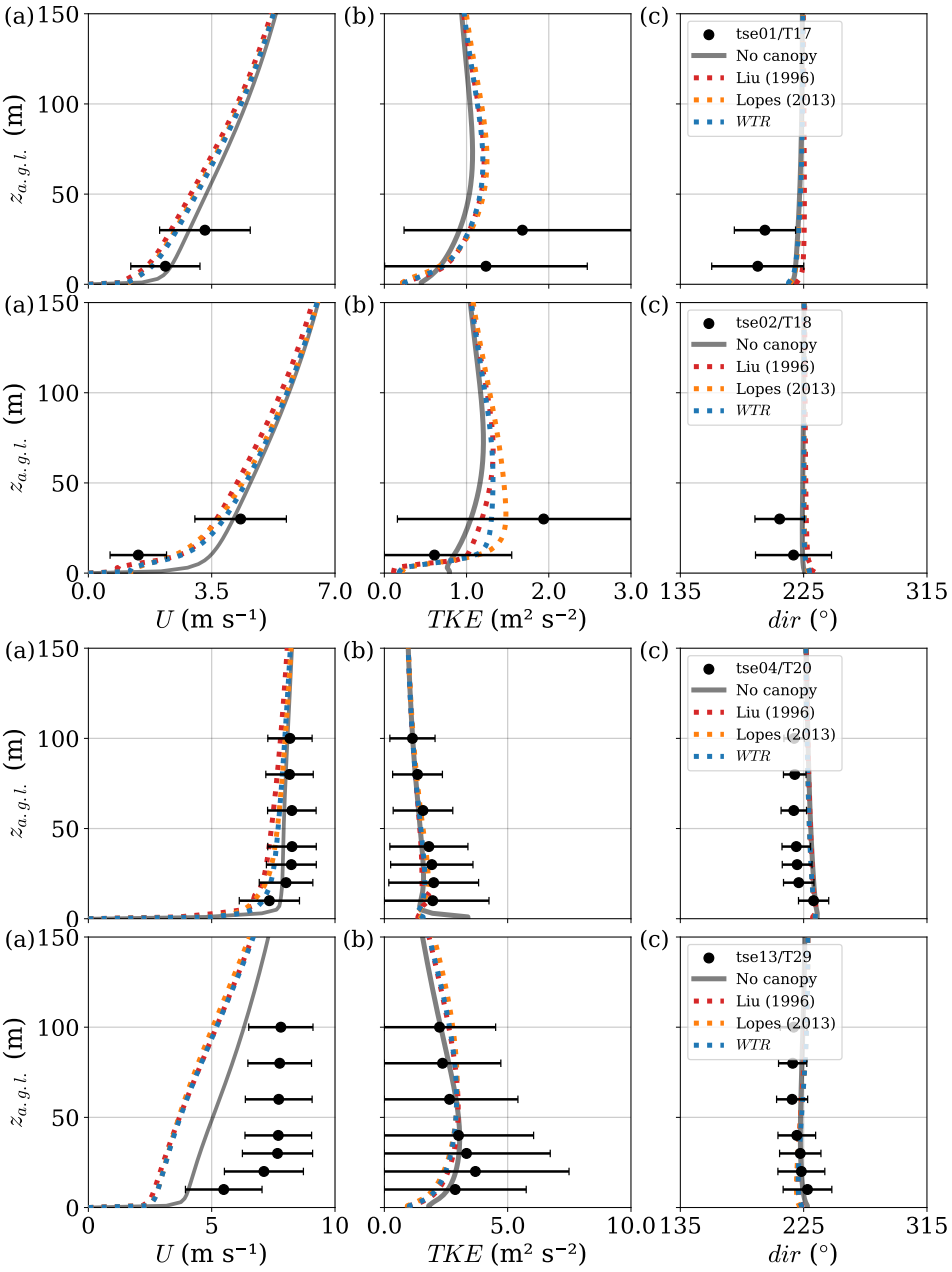


Figure 6.8: SW wind measurements and computational results for transect B: (a) wind speed; (b) turbulent kinetic energy; (c) wind direction. Black horizontal lines indicate the standard deviations of the measurements.

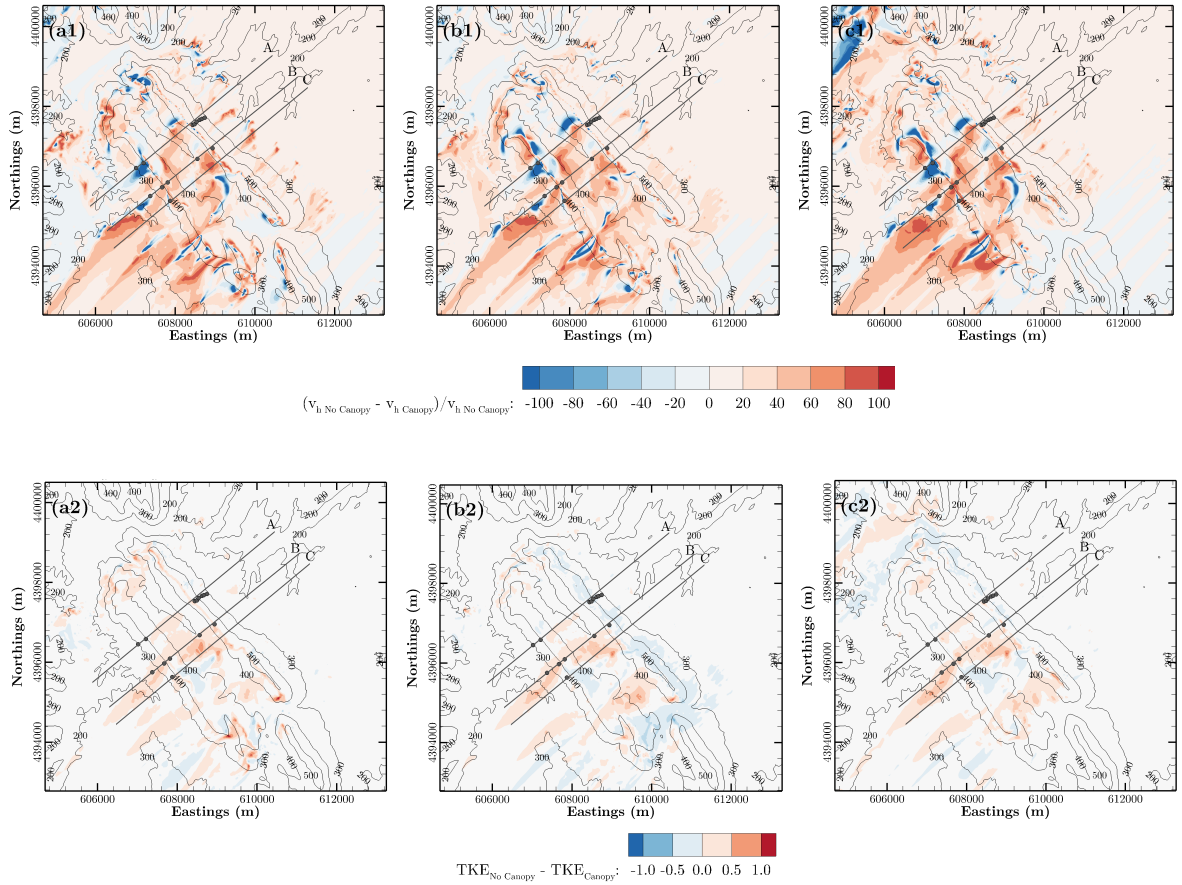


Figure 6.9: Velocity deficit ($(V_{h\ \text{No Canopy}} - V_{h\ \text{Canopy}})/V_{h\ \text{No Canopy}} \times 100$ %) and turbulent kinetic energy difference ($TKE_{\text{No Canopy}} - TKE_{\text{Canopy}}$, in $\text{m}^2\,\text{s}^{-2}$) at 17 m a.g.l. for NE winds, highlighting the effects of the forested regions. The upper row (a1–c1) shows the velocity deficit, and the lower row (a2–c2) shows the turbulent kinetic energy difference for: (a) Liu; (b) Lopes; (c) WTR. Transects A, B, and C are shown. Grey dots mark the tower locations along each transect, consistent with Figure 6.1, and black labels indicate the terrain elevation.

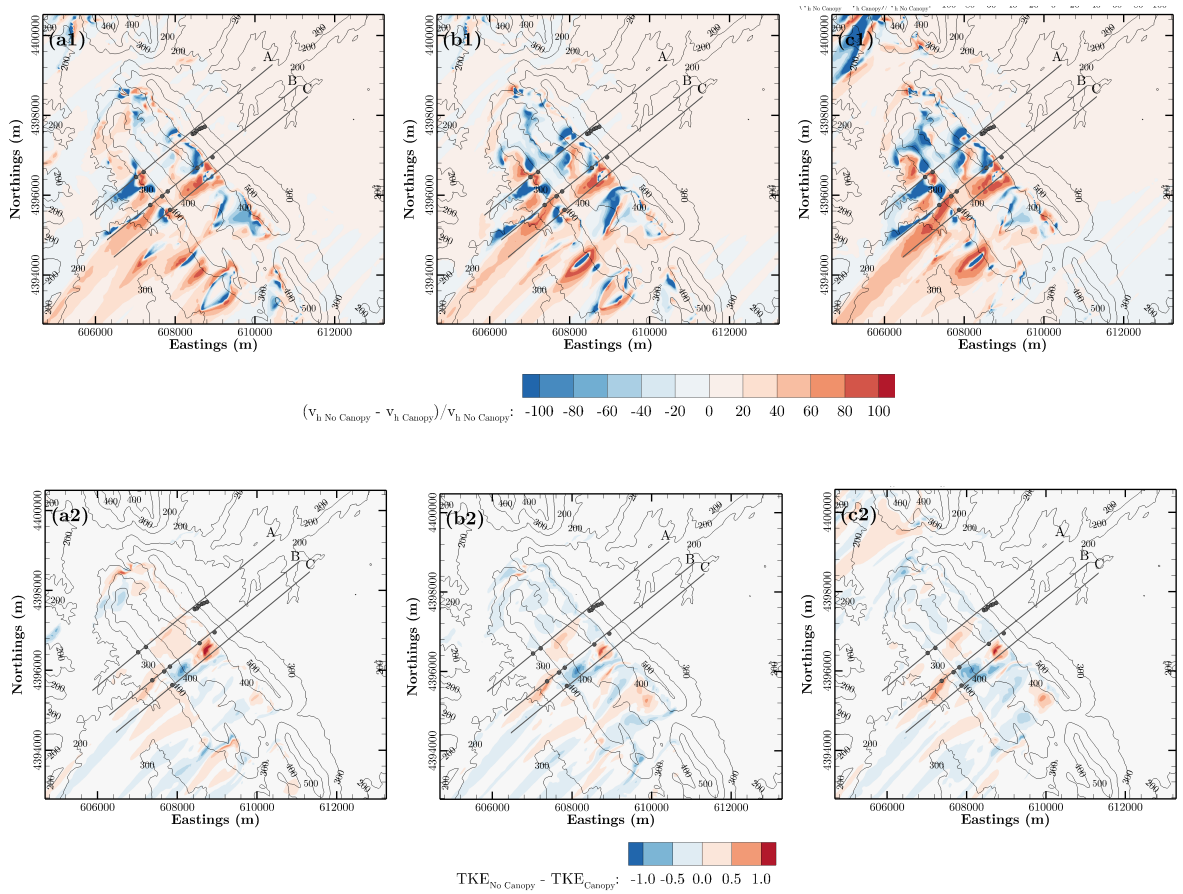


Figure 6.10: Velocity deficit ($(V_{h\ \text{No Canopy}} - V_{h\ \text{Canopy}})/V_{h\ \text{No Canopy}} \times 100\ \%$) and turbulent kinetic energy difference ($TKE_{\text{No Canopy}} - TKE_{\text{Canopy}}$, in $\text{m}^2\,\text{s}^{-2}$) at 98 m a.g.l. for NE winds, highlighting the effects of the forested regions. The upper row (a1–c1) shows the velocity deficit, and the lower row (a2–c2) shows the turbulent kinetic energy difference for: (a) Liu; (b) Lopes; (c) WTR. Transects A, B, and C are shown. Grey dots mark the tower locations along each transect, consistent with Figure 6.1, and black labels indicate the terrain elevation.

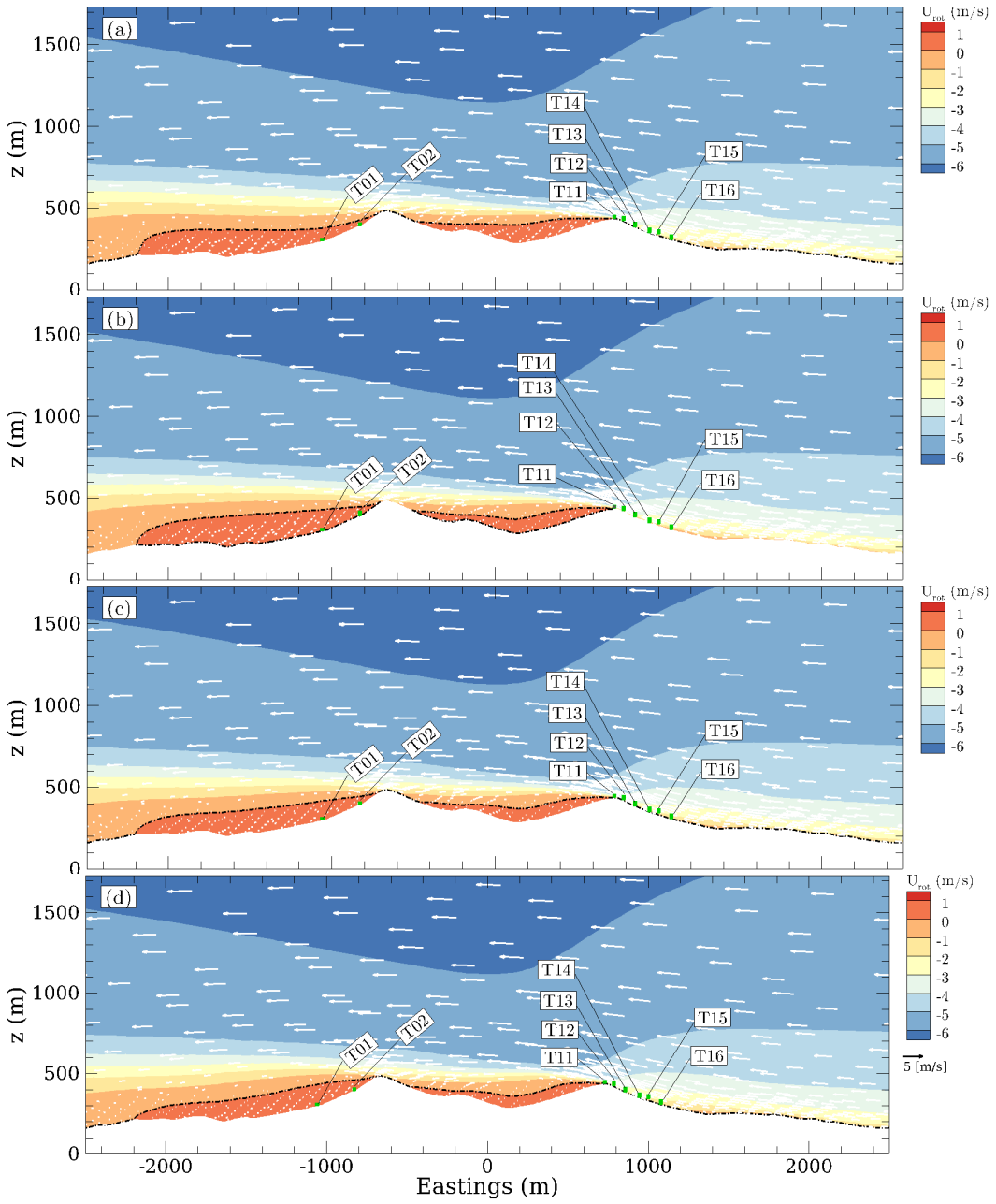


Figure 6.11: Streamwise wind along transect A for NE winds: (a) without canopy parametrisation, (b) Liu, (c) Lopes and (d) WTR model.

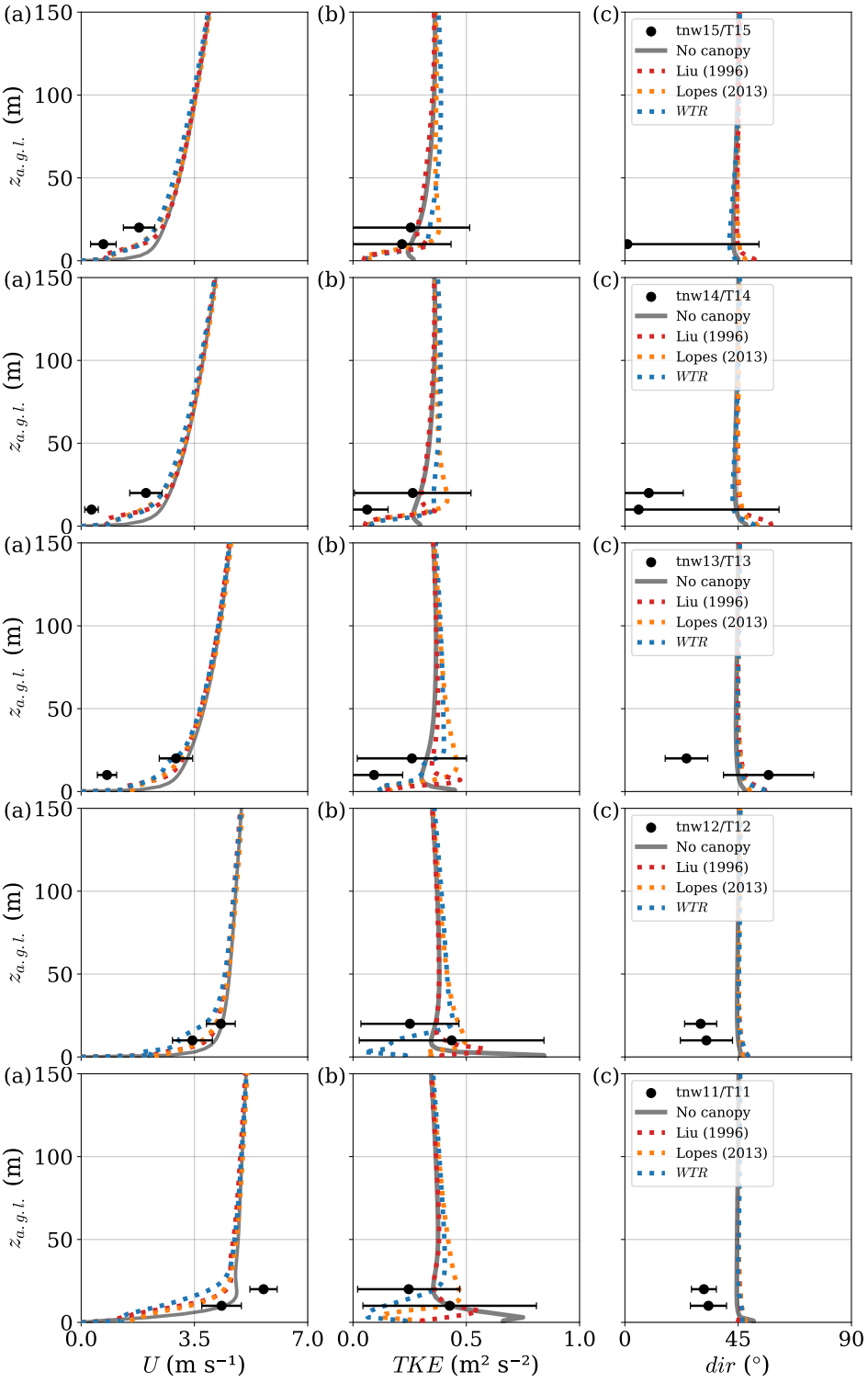


Figure 6.12: NE wind measurements and computational results for transect A: (a) wind speed; (b) turbulent kinetic energy; (c) wind direction. Black horizontal lines indicate the standard deviations of the measurements.

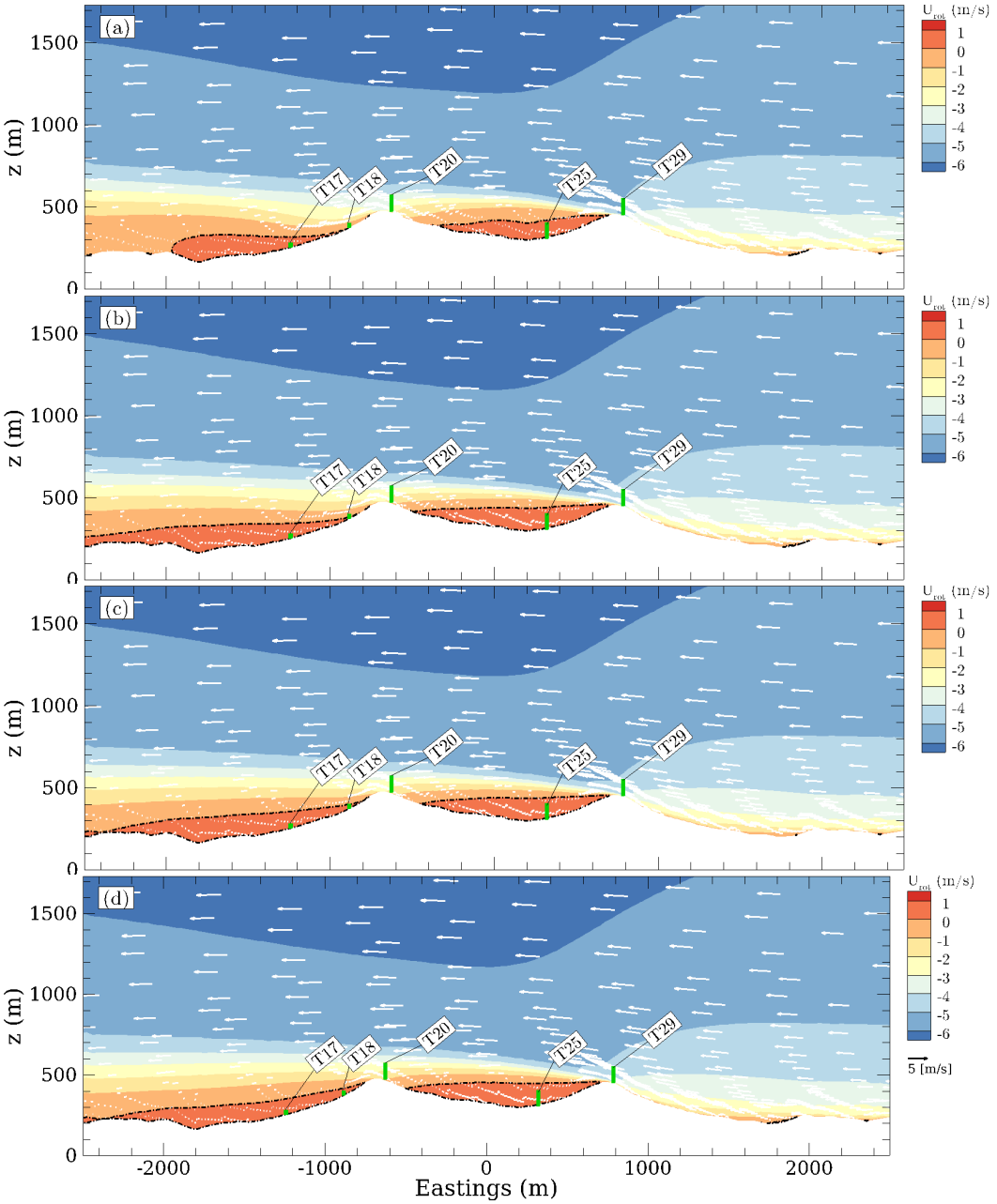


Figure 6.13: Streamwise wind along transect B for NE winds: (a) without canopy parametrisation, (b) Liu, (c) Lopes and (d) WTR model.

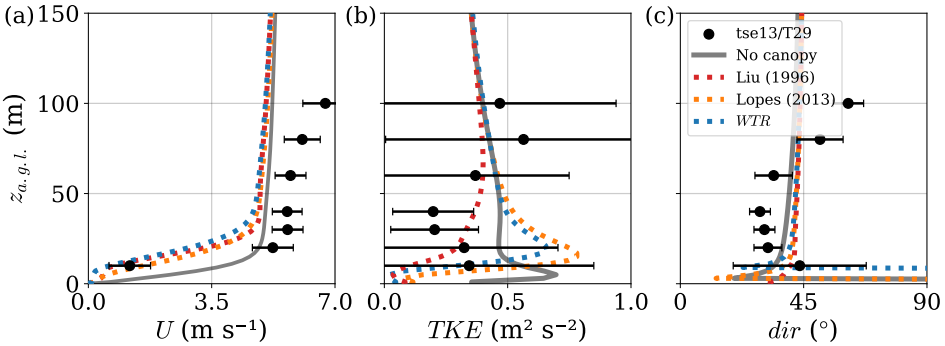


Figure 6.14: NE wind measurements and computational results for transect B: (a) wind speed; (b) turbulent kinetic energy; (c) wind direction. Black horizontal lines indicate the standard deviations of the measurements.

approaches such as Liu or Lopes.

These results are subject to uncertainties. To enhance the representativeness of the validation process, additional simulations under a broader range of atmospheric conditions and times of day are recommended. Moreover, the classification of near-neutral conditions remains uncertain, highlighting the need to explore alternative stability metrics. Coupling the microscale model with mesoscale simulations would help better constrain upstream flow characteristics and boundary-layer properties. In addition, incorporating a more detailed and spatially variable surface roughness map—such as the CORINE Land Cover dataset—alongside complementary tree height data from sources like the Sentinel-2 database, potentially combined with the 2015 ALS survey, could improve the realism of the canopy representation and extend the effective forest cover. Altogether, these enhancements would support a more robust and comprehensive evaluation of model performance over forested, complex terrain.

6.5 Conclusion

This study evaluates the WTR approach in the Perdigão site under quasi-neutral, and southwesterly and northeasterly wind conditions (225° and 45°). Computational results were benchmarked against observational data to assess model performance. Two alternative models—Liu et al. (1996) and Lopes et al. (2013)—and one case without canopy parametrisation were also used for comparison. Wind speed, turbulent kinetic energy, and wind direction were the variables of interest.

The results revealed:

- Wind speed was influenced by vegetation, particularly along the downhill slopes and within the valley, with all models showing similar performance in reproducing it;
- Wind jets appeared across all models, mainly in the valley and on the downwind side, in regions of lower forest density;
- The canopy enhanced the separated flow regions in the valley and downwind of the second ridge;

- TKE was generally higher across most areas, except within flow recirculation regions;
- An increase in TKE at 98 m a.g.l. is likely linked to enhanced turbulence within the internal boundary layer above the canopy;
- The Liu et al. (1996) model predicted lower TKE, the Lopes et al. (2013) model tended to produce higher values, and the WTR model gave intermediate results;
- The flow patterns of WTR and Lopes et al. (2013) were similar and different from Liu et al. (1996)'s, consistent with findings presented in Chapter 5.
- Local misrepresentation of forest structure led to increased bias in the results.
- Topography plays a stronger role, making it hard to isolate forest effects—especially under near-neutral conditions.
- Towers inside or next to forests are better for testing canopy models. This shows the importance of choosing sensor locations carefully when studying how vegetation affects the flow.

This work shows that the WTR model, as implemented in the VENTOS®/2 CFD code, captures canopy-induced flow modifications across complex terrain. The results also emphasise the importance of representing heterogeneous vegetation to resolve key flow features in complex, forested terrain, supporting ongoing efforts to include detailed canopy structure in atmospheric modelling for better accuracy.

CHAPTER 7

Conclusions

This study aimed to improve the knowledge of atmospheric flow over forested terrain, supporting more efficient wind turbine and wind farm operations. This was achieved by carrying out microscale computational modelling and comparing the results with site measurements. Several established RANS canopy models were tested over flat terrain with a forest edge. In addition, the weak turbulence regime (WTR) assumption was introduced into the RANS $k-\varepsilon$ formulation to explore canopy effects in three setups: a homogeneous forest, a forest edge, and a forested hill. The WTR approach was then implemented in the in-house VENTOS®/2 CFD framework and applied to simulations over both forest edge and complex forested terrain.

7.1 Main contributions

Results from eight common canopy models–Costa et al. (2006), Green (1992), Lopes et al. (2013), Lopes et al. (2021), Liu et al. (1996), Sanz (2003), Sogachev and Panferov (2006) and Svensson and Häggkvist (1990)–showed minor differences in streamwise velocity, demonstrating reliable predictions independent of the model used. Models that account mainly for the dissipation of turbulent kinetic energy (TKE) by short-circuiting the energy cascade–Lopes et al. (2013) and Lopes et al. (2021)– provide a more physically accurate representation of turbulence. In contrast, models treating the forest canopy mainly as a net source of TKE tended to diverge from field observations. Except for the models by Svensson and Häggkvist (1990) and Green (1992), the remaining six approaches were suitable for wind resource assessments over forested flat terrain, offering insight into both the horizontal and vertical extent of the internal boundary layer (IBL) above the canopy.

The WTR approach was integrated into the two-dimensional RANS $k-\varepsilon$ model and tested in three idealised configurations: a homogeneous forest, a forest edge, and a forested hill. Its performance was evaluated against LES results from Lopes et al. (2013) and benchmarked against two reference RANS models (Liu et al. (1996) and Lopes et al. (2013)). The WTR model captured key flow features, in high-turbulence regions such as forest edges and hill wakes. It reproduced LES predictions for wind speed, TKE, Reynolds shear stress, and dissipation near the forest edge, with minor differences near the canopy top. In the forested hill case, it provided a better representation of the recirculation zone and improved the overall prediction of both first- and second-order flow statistics compared to the reference models.

Results using the WTR approach within the VENTOS®/2 CFD framework over flat terrain reproduced key flow features reported in LES simulations and earlier RANS studies. These included the reduction of wind speed and TKE within the canopy, the development of a sub-canopy wind jet caused by low leaf density, and a well defined IBL above the canopy top. Overall, the performance of the WTR approach was comparable to the Lopes et al. (2013) model in capturing both mean flow and turbulence characteristics. The results demonstrated

that the WTR model represents the key dynamics of streamwise velocity and TKE, striking a balance between accuracy and computational efficiency.

Over complex terrain, the WTR model showed similar performance to the Liu et al. (1996) and Lopes et al. (2013) models in predicting both mean and turbulent flow. It compared well with measurements from the Perdigão site, showing good agreement with observations. Unlike the reference models, the WTR approach does not rely on fixed constants, yet it still captures key flow features across forested slopes, hilltops, and valleys. These results indicate that the WTR model is well suited for use in complex terrain. They also highlight the importance of accounting for changes in vegetation, which helps to reproduce critical flow patterns in forested landscapes. Overall, the findings support further development of flow models that include detailed canopy structure to improve accuracy in atmospheric simulations.

7.2 Future work

The findings in this thesis highlight several opportunities to increase the accuracy of flow predictions over forested terrain. Key areas for future work include:

- Higher-order terms in WTR: building on the observations by Lopes et al. (2021), incorporating third-order terms into the WTR approach (to be addressed in Paper III) might improve the agreement with LES results, particularly in complex flow regimes. However, this remains challenging within the RANS framework and requires new closure strategies.
- More detailed surface data, including spatially varying surface roughness and vegetation characteristics—drawing on sources such as the CORINE Land Cover dataset, Sentinel-2-derived tree heights, and the 2015 ALS Perdigão data (to be addressed in Paper IV)—could improve the canopy representation and extend the forested area explicitly represented within the simulation domain, particularly in regions where forest canopy assumptions are currently not applied.
- Improved characterisation of atmospheric stability: reducing uncertainty in stability classification is essential. This could involve testing alternative parameters and extending the analysis across a broader range of simulation periods.
- Coupling with mesoscale models: linking microscale simulations to mesoscale outputs can provide more realistic boundary conditions and capture upstream flow and boundary-layer dynamics more accurately. This would require using the in-house tool VENTOS®/M CFD (Rodrigues et al., 2016).
- Recirculation zone validation: results from the Perdigão site (Chapter 6) revealed a strong recirculation zone under canopy parametrisation. These findings could be validated using LIDAR measurements from the Perdigão-2017 campaign (to be addressed in Paper IV).

These developments would contribute to more physically accurate canopy models and support improved wind resource assessments in forested and complex terrain.

Appendices

Appendices

APPENDIX A

Results from Falster Case of Study

This appendix presents supplementary results from the Falster case study discussed in Chapter 3. The analyses provided here complement the main results by offering additional spatial information on the flow behaviour near the forest edge. These results are included in the appendix to preserve clarity and focus in the main chapter. The emphasis is on the spatial distribution of the flow both towards and from the forest, supporting the interpretation and discussion presented in Section 3.4.

A.1 Spatial distribution of flow towards the forest

A.1.1 Wind speed distribution

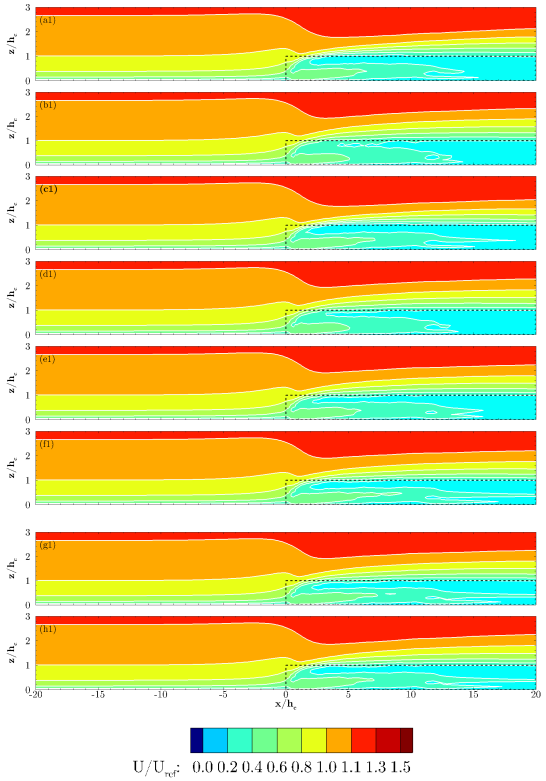


Figure A.1.1: Flow towards the forest: streamwise velocity (a1) Svensson, (b1) Green, (c1) Liu, (d1) Sanz, (e1) Costa, (f1) Lopes, (g1) Viana, (h1) Sogachev. U_{ref} denotes the reference velocity, and h_c the average tree height.

A.1.2 Turbulent kinetic energy distribution

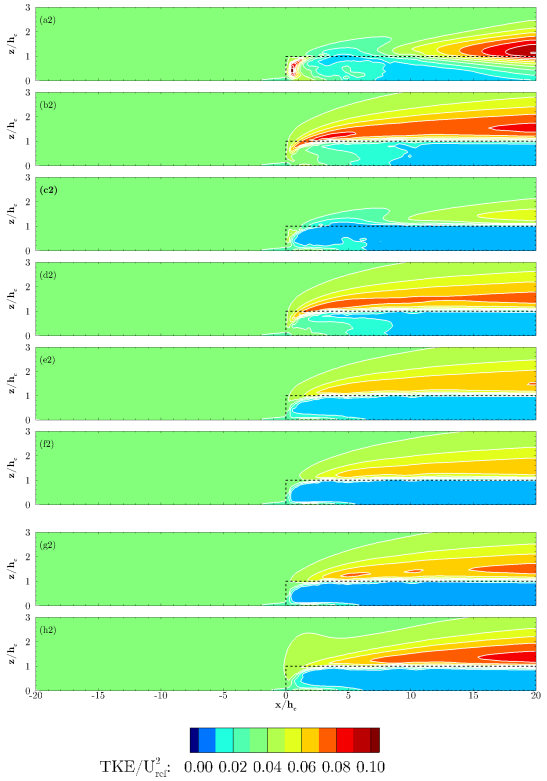


Figure A.1.2: Flow towards the forest: turbulent kinetic energy (a2) Svensson, (b2) Green, (c2) Liu, (d2) Sanz, (e2) Costa, (f2) Lopes, (g2) Viana, (h2) Sogachev. U_{ref} denotes the reference velocity, and h_c the average tree height.

A.2 Spatial distribution of flow from the forest

A.2.1 Wind speed distribution

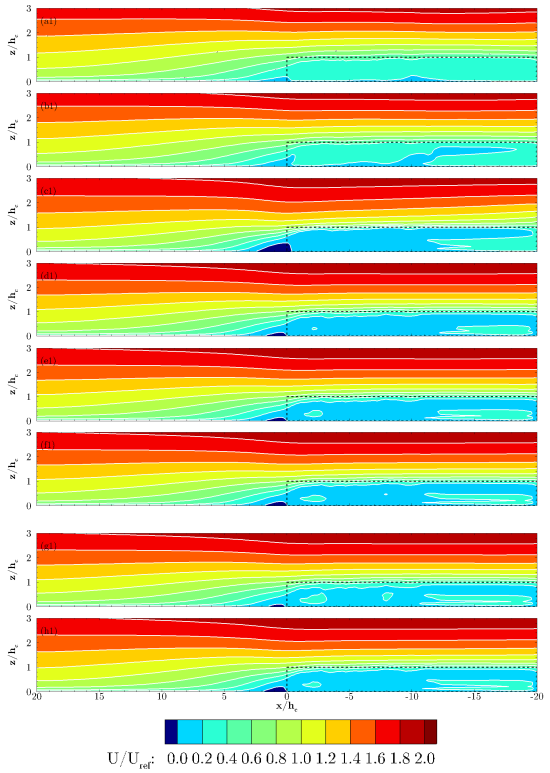


Figure A.2.1: Flow from the forest: streamwise velocity (a1) Svensson, (b1) Green, (c1) Liu, (d1) Sanz, (e1) Costa, (f1) Lopes, (g1) Viana, (h1) Sogachev. U_{ref} denotes the reference velocity, and h_c the average tree height.

A.2.2 Turbulent kinetic energy distribution

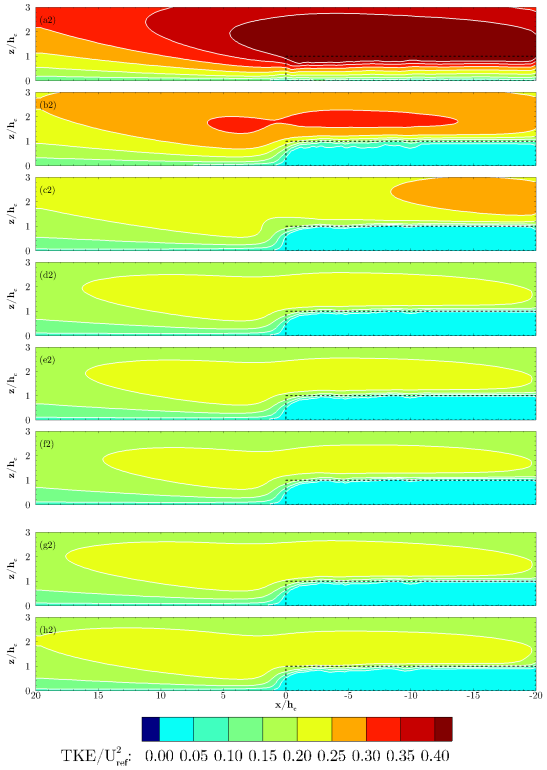


Figure A.2.2: Flow from the forest: turbulent kinetic energy (a2) Svensson, (b2) Green, (c2) Liu, (d2) Sanz, (e2) Costa, (f2) Lopes, (g2) Viana, (h2) Sogachev. U_{ref} denotes the reference velocity, and h_c the average tree height.

APPENDIX B

Results from Forest Edge Flow Case

This appendix presents a detailed comparison of RANS predictions against LES results for the forest edge flow case, complementing the analyses presented in Chapter 4. The tests focus on key flow quantities—wind speed, turbulent kinetic energy (TKE), and Reynolds shear stress—along the domain. The results include direct comparisons of RANS models (Liu, Lopes, and the weak turbulence regime, WTR) with LES outputs, as well as error metrics such as RMSE and bias. These analyses aim to evaluate the performance of the WTR approach relative to established RANS models in capturing the spatial structure of turbulence across a forest edge.

B.1 Reynolds shear stress along domain

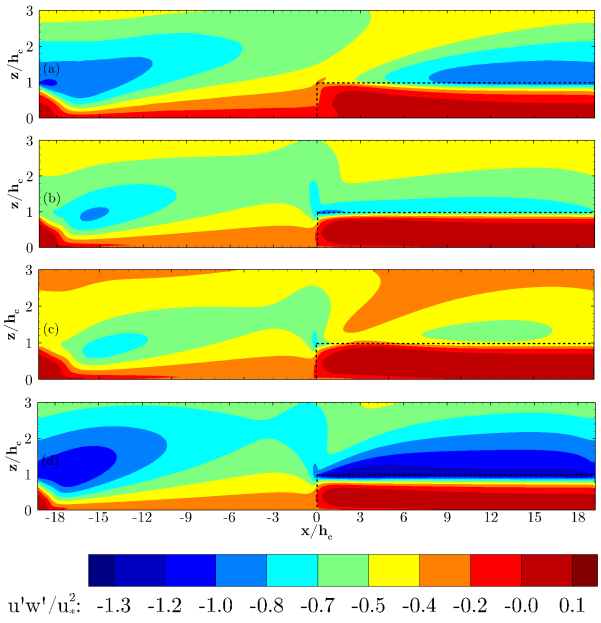


Figure B.1: Edge case Reynolds shear stress: (a) LES; (b) WTR; (c) Liu; (d) Lopes (2013).

B.2 Table of RMSE and BIAS between LES and RANS

Table B.2: Error indicator of the flow across a forest edge

Variable	x/h_c	Liu (1996)		Lopes (2013)		WTR	
		RMSE	BIAS	RMSE	BIAS	RMSE	BIAS
U/U_b	-8.5	0.041	**0.003**	0.053	0.033	**0.037**	0.007
	-3.0	0.032	**-0.002**	0.046	0.028	**0.030**	**0.002**
	0.0	0.031	-0.007	0.040	0.023	**0.029**	**-0.003**
	1.0	**0.032**	-0.004	0.051	0.027	0.035	**0.0002**
	3.0	**0.029**	**-0.001**	0.076	0.038	0.047	0.009
	7.0	**0.038**	**-0.007**	0.071	0.039	0.039	**0.007**
	19.0	0.057	**0.007**	0.065	0.039	**0.049**	0.011
	Avg.	**0.037**	**-0.002**	0.057	0.032	0.038	0.005
	Std.	0.010	0.005	0.013	0.007	0.008	0.005
TKE/u_*^2	-8.5	0.605	-0.541	**0.186**	**0.098**	0.376	-0.319
	-3.0	0.457	-0.414	**0.176**	**0.103**	0.278	-0.236
	0.0	0.330	-0.177	0.224	0.151	**0.196**	**-0.134**
	1.0	0.787	0.316	0.248	0.138	**0.185**	**-0.072**
	3.0	0.334	-0.136	0.332	0.259	**0.154**	**-0.034**
	7.0	0.618	-0.503	**0.260**	**0.183**	0.286	-0.231
	19.0	0.844	-0.704	**0.259**	**-0.031**	0.601	-0.496
	Avg.	0.568	-0.308	**0.241**	**0.129**	0.297	-0.217
	Std.	0.205	0.341	0.053	0.089	0.154	0.158
$\overline{u'w'}/u_*^2$	-8.5	0.117	-0.074	0.071	0.050	**0.065**	**-0.030**
	-3.0	0.074	-0.036	0.074	0.064	**0.041**	**-0.001**
	0.0	**0.190**	**0.090**	0.311	0.240	0.241	0.153
	1.0	**0.072**	**-0.011**	0.383	0.252	0.213	0.107
	3.0	**0.126**	-0.099	0.434	0.300	0.129	**0.062**
	7.0	0.226	-0.178	0.266	0.208	**0.079**	**-0.052**
	19.0	0.314	-0.258	**0.109**	**0.089**	0.182	-0.151
	Avg.	0.160	-0.081	0.235	0.089	**0.136**	**0.013**
	Std.	0.089	0.113	0.151	0.102	0.078	0.103
$\varepsilon h_c/u_*^3$	-8.5	**0.813**	**0.231**	1.536	0.538	1.029	0.323
	-3.0	**0.892**	**0.245**	1.486	0.499	1.068	0.321
	0.0	0.901	0.462	1.189	0.464	**0.879**	**0.338**
	1.0	4.947	3.249	1.018	**0.363**	**0.884**	0.428
	3.0	2.372	1.754	**0.545**	**0.324**	0.739	0.466
	7.0	0.948	0.657	**0.524**	**0.422**	0.886	0.568
	19.0	1.492	0.724	**0.382**	**0.321**	0.674	0.405
	Avg.	1.766	1.046	0.954	0.419	**0.880**	**0.407**
	Std.	1.508	1.100	0.476	0.086	0.141	0.090

Note: The best values are bold, and the worst are in underlined.

B.3 Differences between RANS and LES

B.3.1 Wind speed differences along domain

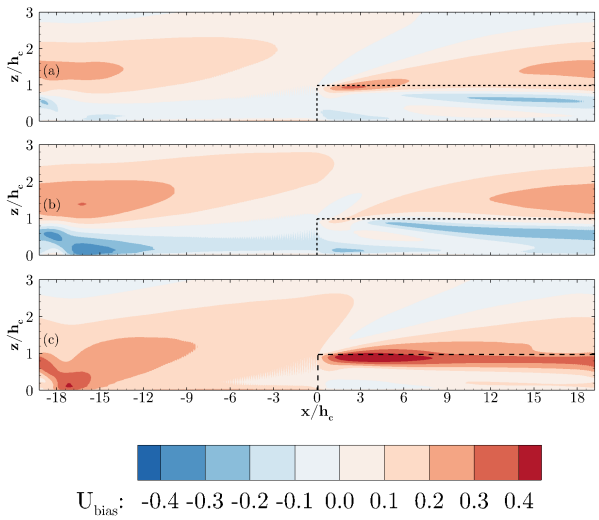


Figure B.3.1: Wind speed differences ($\mathrm{m\,s^{-1}}$): (a) WTR; (b) Liu; (c) Lopes (2013).

B.3.2 Turbulent kinetic energy differences along domain

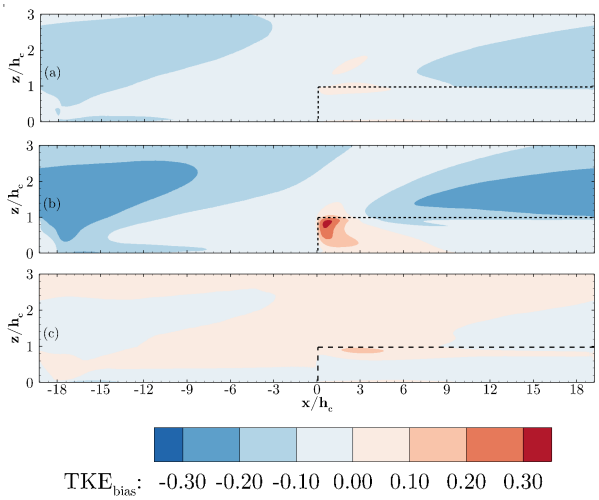


Figure B.3.2: Turbulent kinetic energy differences($\mathrm{m^2\,s^{-2}}$): (a) WTR; (b) Liu; (c) Lopes (2013).

B.3.3 Reynolds shear stress differences along domain

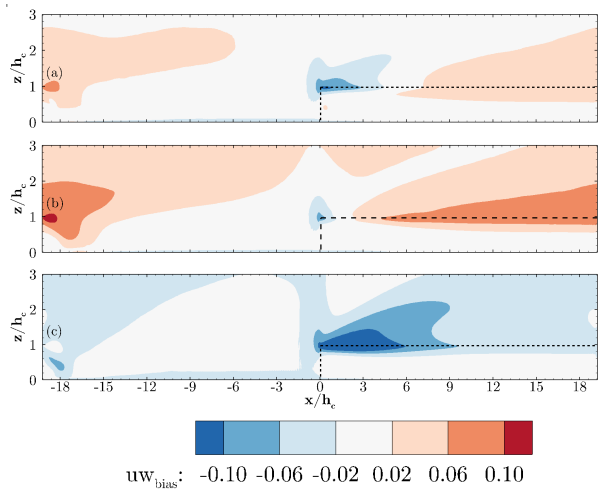


Figure B.3.3: Reynolds shear stress differences ($m^2\,s^{-2}$): (a) WTR; (b) Liu; (c) Lopes (2013).

APPENDIX C

Results from Forested Hill Case

This appendix presents a detailed evaluation of RANS model predictions for the forested hill case, complementing the analyses discussed in Chapter 4. The focus is on key flow quantities—wind speed, turbulent kinetic energy (TKE), and Reynolds shear stress—along the hill domain. Comparisons are made between LES reference data and three RANS approaches: Liu, Lopes, and the weak turbulence regime (WTR). The appendix includes both the spatial distribution of Reynolds shear stress and error metrics, such as RMSE and bias, to assess model performance. The aim is to characterise how well each RANS model captures the complex flow dynamics induced by the hill, including recirculation regions and turbulence enhancement in the lee of the hill.

C.1 Reynolds shear stress along domain

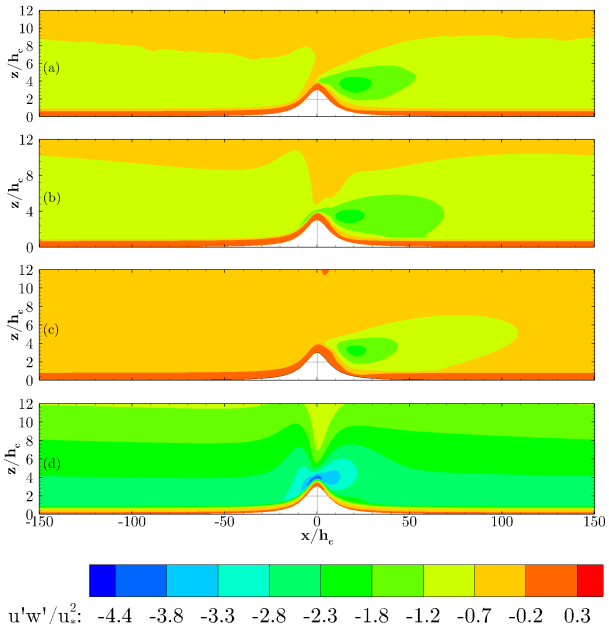


Figure C.1: Hill case Reynolds shear stress: (a) LES; (b) WTR; (c) Liu; (d) Lopes (2013).

C.2 Table of RMSE and BIAS between LES and RANS

Table C.2: Error indicator of the flow across a forested hill

Variable	x/L	Liu (1996)		Lopes (2013)		WTR	
		RMSE	BIAS	RMSE	BIAS	RMSE	BIAS
U/U_b	-5.1	0.074	0.014	0.063	0.025	**0.045**	**0.009**
	-3.0	0.074	0.013	0.063	0.024	**0.045**	**0.009**
	-1.0	0.066	0.011	0.053	0.016	**0.039**	**0.006**
	0.0	0.059	**0.006**	0.086	0.023	**0.039**	0.007
	0.431	0.064	**-0.003**	0.118	0.046	**0.042**	0.007
	1.4	**0.059**	**-0.015**	0.171	0.083	0.055	**0.011**
	2.5	**0.052**	**-0.006**	0.147	0.075	0.059	0.021
	3.349	**0.051**	**0.002**	0.110	0.058	**0.051**	0.017
	5.0	0.049	**0.004**	0.075	0.039	**0.040**	0.008
	Avg.	0.061	**0.003**	0.098	0.043	**0.046**	0.011
	Std.	0.009	0.010	0.041	0.024	0.007	0.005
TKE/u_*^2	-5.1	0.953	-0.833	2.476	2.316	**0.271**	**-0.174**
	-3.0	0.947	-0.828	2.539	2.364	**0.268**	**-0.165**
	-1.0	0.884	-0.742	2.886	2.666	**0.239**	**-0.076**
	0.0	0.979	-0.626	2.767	2.540	**0.309**	**-0.061**
	0.431	1.226	-0.919	2.733	2.564	**0.424**	**-0.178**
	1.4	0.867	-0.654	3.220	3.069	**0.545**	**0.165**
	2.5	0.939	-0.178	2.647	2.408	**0.404**	**0.011**
	3.349	0.749	-0.382	2.482	2.233	**0.325**	**-0.057**
	5.0	0.627	-0.436	2.404	2.214	**0.254**	**-0.009**
	Avg.	0.908	-0.622	2.684	2.486	**0.338**	**-0.060**
	Std.	0.165	0.245	0.256	0.267	0.1101	0.110
$\overline{u'w'}/u_*^2$	-5.1	0.286	-0.246	1.176	1.044	**0.054**	**-0.024**
	-3.0	0.263	-0.221	1.244	1.109	**0.061**	**0.005**
	-1.0	**0.168**	-0.141	1.641	1.402	0.178	**0.116**
	0.0	0.333	-0.280	1.401	0.968	**0.163**	**-0.084**
	0.431	0.498	-0.377	1.349	1.037	**0.219**	**-0.166**
	1.4	0.354	-0.306	1.301	1.133	**0.118**	**-0.037**
	2.5	0.240	-0.123	0.991	0.868	**0.105**	**-0.036**
	3.349	0.200	-0.124	0.950	0.849	**0.093**	**-0.021**
	5.0	0.177	-0.144	1.010	0.915	**0.069**	**0.019**
	Avg.	0.280	-0.218	1.229	1.036	**0.118**	**-0.025**
	Std.	0.104	0.091	0.225	0.170	0.057	0.076
$\varepsilon h_c/u_*^3$	-5.1	0.925	0.227	0.609	0.489	**0.524**	**0.259**
	-3.0	0.953	0.234	0.628	0.505	**0.537**	**0.265**
	-1.0	2.356	0.725	0.835	0.650	**0.704**	**0.353**
	0.0	4.368	1.967	1.408	0.623	**1.397**	**0.555**
	0.431	**0.535**	**-0.037**	0.625	0.502	1.031	0.375
	1.4	**0.499**	**0.179**	1.173	0.949	0.899	0.553
	2.5	0.934	0.529	0.668	0.561	**0.561**	**0.365**
	3.349	0.488	**0.278**	0.621	0.498	**0.428**	0.289
	5.0	0.544	**0.285**	0.598	0.487	**0.442**	0.287
	Avg.	1.289	0.487	0.796	0.585	**0.725**	**0.367**
	Std.	1.293	0.595	0.295	0.149	0.325	0.114

Note: Best and worst values are bold and underlined.

C.3 Differences between RANS and LES

C.3.1 Wind speed differences along domain

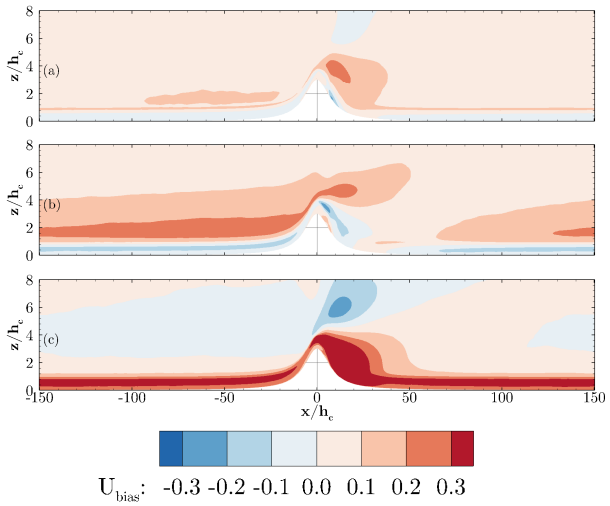


Figure C.3.1: Wind speed differences ($\mathrm{m\,s^{-1}}$): (a) WTR; (b) Liu; (c) Lopes (2013).

C.3.2 Turbulent kinetic energy differences along domain

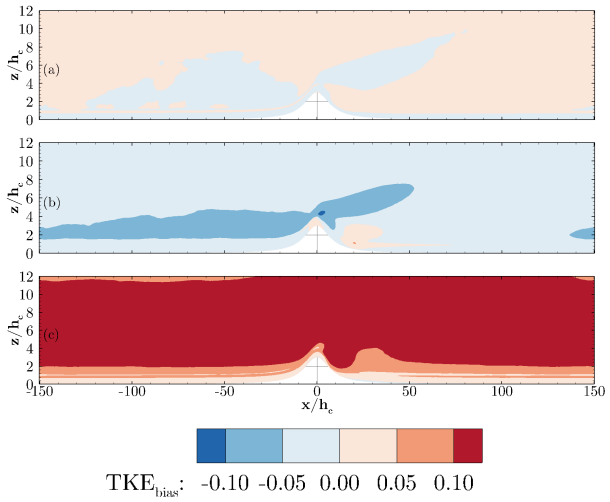


Figure C.3.2: Turbulent kinetic energy differences ($\mathrm{m^2\,s^{-2}}$): (a) WTR; (b) Liu; (c) Lopes (2013).

C.3.3 Reynolds shear stress differences along domain

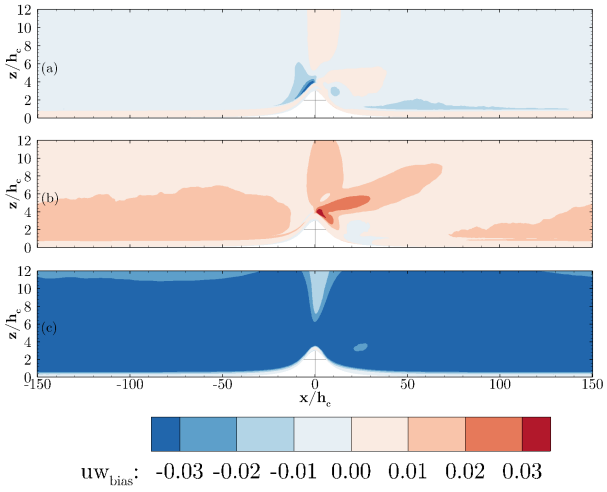


Figure C.3.3: Reynolds shear stress differences ($m^2\,s^{-2}$): (a) WTR; (b) Liu; (c) Lopes (2013).

APPENDIX D

Publications

D.1 Paper I: Assessing canopy models across forest edges on flat terrain

This paper has been published in *Journal of Physics: Conference Series*, 2024 (Monteiro et al., 2024).

Journal of Physics: Conference Series **2767** (2024) 092011 doi:10.1088/1742-6596/2767/9/092011

Assessing canopy models across forest edges on flat terrain

J R Monteiro, V T P Batista and J M L M Palma

Faculdade de Engenharia da Universidade do Porto, Rua Dr Roberto Frias, s/n, 4200-465 Porto, Portugal

E-mail: `jesus.monteiro@fe.up.pt`

Abstract. Computational modelling of atmospheric flows in forested areas is crucial for wind resource assessment, wind farm design and turbine siting, enabling the identification of low wind speed and high turbulence regions. However, when setting up a RANS simulation in a forested area, the question arises: what is the most appropriate canopy model? In this study, employing VENTOS-2D (RANS with k-ε turbulence model), we identified the most suitable of seven canopy models to simulate the mean flow characteristics (wind speed) and second-order flow statistics (turbulent kinetic energy and shear stress) of the flow over a forest edge at the Island of Falster, by comparing against anemometer measurements and LES results. All models exhibited similar profiles for the mean wind speed, with a normalised RMSE of approximately 0.300. Regarding turbulent kinetic energy, the Lopes model outperformed the others, achieving an RMSE of 0.002. Lastly, for the Reynolds shear stress, Liu and Svensson's models showed the lowest RMSE values (1.756 and 1.609), while others were over 4× larger (RMSE > 7). In summary, the performance of each model varies with the variable in focus, which is related to the model's derivation method. However, considering all three analysed variables, Liu emerged as the most effective.

1. Introduction

Computational modelling of atmospheric flows in forested areas is relevant to wind energy applications, namely in resource assessment and wind park design, to identify regions of low wind speed or high turbulence. Turbulence decreases the performance and lifetime of wind turbines, and canopy models must be able to correctly predict the turbulent layer extension above and after the forest. A wrong prediction of the turbulence field may lead the wind site engineering to bad decisions—e.g., wind turbine sector shutdown, changes in the turbine power curve, or even changes in the turbine position—, and lower average energy production.

The forest's effect on atmospheric turbulence has been the subject of many studies, of which the recent review paper [1] offers an overview of how our understanding and modelling of forest flows have developed. In particular, the forest edge effect on the flow, which has been studied using wind tunnels, numerical and field experiments [2, 3, 4], depends on the foliage density and canopy vertical structure [3]. In the case of a uniform vegetation density, an internal boundary layer forms from the leading edge, with high turbulence intensity above the canopy, and the flow may reach equilibrium at approximately ten canopy heights from the edge. For a deep and sparse trunk space with foliage density concentrated at the top, the appearance and growth of a highly turbulent layer occurs close to the leading edge, with a wind jet at the canopy sub-layer

Content from this work may be used under the terms of the Creative Commons Attribution 4.0 licence. Any further distribution of this work must maintain attribution to the author(s) and the title of the work, journal citation and DOI.
Published under licence by IOP Publishing Ltd

(trunk space), and the flow equilibrium is expected after 20 canopy heights [3].

Large-eddy simulations (LES) can effectively model the complex turbulent flow above canopies, reproducing the velocity, turbulent kinetic energy (k or TKE), and Reynolds shear stress profiles without the need for a tuned canopy model. However, in wind energy applications [5, 6], due to its more affordable computational cost, Reynolds-averaged Navier-Stokes (RANS) with k-εturbulence model is usually employed with additional terms [7] in the momentum (1), turbulent kinetic energy (2) and its dissipation rate (ε) (3) to model the canopy's effect. The approach relies on the mean scalar velocity $|U|$ and six parameters: C_d, the mean drag coefficient, which depends on the forest characteristics; $a(z)$, the leaf area density (LAD) that represents the area of canopy leaves per unit volume (i.e., foliage density over the height of the forest or tree $\mathrm{m}^2\,\mathrm{m}^{-3}$); β_p that sets the fraction of mean flow kinetic energy converted to turbulent kinetic energy (a source term); β_d, the fraction of TKE dissipated (a sink term) by short-circuiting of the energy cascade; and $C_{\varepsilon 4}$ and $C_{\varepsilon 5}$ in the transport equation of ε.

$$F_i = -0.5\,\rho\,C_d\,a(z)\,|U|\,\overline{U_i} \tag{1}$$

$$S_{C_k} = 0.5\,\rho\,C_d\,a(z)\left(\beta_p|U|^3 - \beta_d|U|k\right) \tag{2}$$

$$S_{C_\varepsilon} = 0.5\,\rho\,C_d\,a(z)\left(C_{\varepsilon 4}\beta_p|U|^3\frac{\varepsilon}{k} - C_{\varepsilon 5}\beta_d|U|\varepsilon\right) \tag{3}$$

Many works have tried to adapt canopy model constants ($\beta_p, \beta_d, C_{\varepsilon 4}$ and $C_{\varepsilon 5}$) to reference data in the form of wind tunnel experiments, on-site measurements, or reference simulations (e.g., LES). The multitude of canopy models based on RANS equations, as listed in Ref. [7], of which seven are presented in Table 1, poses the ever-long question of which is the most suitable to simulate the flow's mean characteristics and second-order statistics [8].

Table 1: Canopy model coefficients for the RANS k-ε model.

Model	Svensson [9]	Green [10]	Liu [11]	Sanz [12]	Costa [13]	Lopes [14]	Viana [7]
β_p	1.00	1.00	1.00	1.00	0.17	0.00	0.00
β_d	0.00	4.00	4.00	5.10	3.37	4.00	2.67
$C_{\epsilon 4}$	1.95	1.50	1.50	0.90	0.90	0.00	0.00
$C_{\epsilon 5}$	0.00	1.50	0.60	0.90	0.90	0.90	1.00

The earlier RANS k-ε models used wind tunnel experiment data to obtain and validate the model constants [9, 11]. Svensson [9] simulated the mean wind speed, shear stress, and turbulence intensity sufficiently downwind from a forest edge to fully develop the flow (analogous to a homogeneous forest case) without accounting for additional TKE dissipation due to the canopy, which Green [10] did. Liu [11] used the terms of Green [10] to obtain wind speed and TKE profiles, validating the results against wind-tunnel flow just downwind (half a tree height) of a homogeneous forest, overestimating the eddy viscosity (μ_t) in this region, where the presence of the canopy is still very much felt. To correct this overprediction, they enhanced the dissipation rate caused by the forest by reducing the sink contribution to S_{C_ε} (i.e., $C_{\varepsilon 5}$). Sanz [12] proposed model constants based on an analytical solution within a dense and homogeneous canopy, far enough from any boundary (where the mixing length does not vary significantly), obtaining the highest turbulence sink-term contribution ($\beta_d = 5.1$). Costa [13] presents some similarities to Sanz [12], since their validation was based on the latter's analytical solutions and LES results. Contrasting the previous models, Lopes [14] considers a null fraction of mean flow kinetic energy converted to wake-generated TKE by canopy drag (a null production term, β_p). This model was calibrated using LES flow results over a homogeneous canopy and evaluated against LES results over a forest edge and a forested hill. In Viana [7], the canopy-related terms in the

momentum, TKE, and dissipation transport equations were approximated using a Taylor series expansion of the velocity magnitude, with a velocity scale based on the total kinetic energy and assuming a weak turbulence regime (WTR), where turbulent fluctuations are much smaller than the magnitude of mean-flow velocity. A zero-order WTR approximation was considered for the canopy drag, and a second-order approximation for the effect on the transport of TKE and its dissipation rate, resulting in a null source term ($\beta_p = 0$), with the canopy acting solely as a dissipative agent of turbulence, similarly to Lopes [14].

Unlike most studies of edge flow that rely on wind tunnels and numerical experiments [3, 4] in the development of RANS-based models, in this study, we use field measurements [15] and LES results [4]. We aimed to identify one of seven canopy models (Table 1) across a forest edge on flat terrain, where the RANS results of streamwise wind speed, turbulent kinetic energy, and Reynolds shear stress best agreed with the field and LES data. For this purpose, the flow governing equations (mass, momentum, and k-ε turbulence model) were solved for a neutrally stratified, statistically steady turbulent boundary layer.

In what follows, we present a brief description of the experimental data (Section 2), the fundamental equations of the mathematical models (Section 3), the numerical techniques (Section 4), the results and discussion (Section 5), and conclusions (Section 6).

2. Experimental data

The measurements in the Island of Falster [15] were selected because the site enables the 2D interpretation of the flow and it is a well-reported field experiment with available LES results [4] that we could compare with our RANS outputs. The site consisted of trees with average height, h_c, of about 24 m, and leaf area index (LAI $= \int_0^{h_c} a(z)dz$) of approximately 6 $\mathrm{m^2\,m^{-2}}$. Two masts (45.9 m) with sonic anemometers were deployed: M1 on the grass field at approximately $1.5h_c$ upstream from the forest leading edge and M2 inside the forest at approximately $1.5h_c$ from the edge. The atmosphere was assumed neutrally stratified.

3. Governing equations

The simulations employed the VENTOS-2D model, a simplified VENTOS®/2 CFD code [16], to solve for a turbulent flow under a neutrally stratified atmosphere. The flow governing equations –mass(4), momentum(5), and k-ε turbulence model(6,7)– in RANS formulation were used:

$$\frac{\partial\left(\rho U_i\right)}{\partial x^i} = 0 \tag{4}$$

$$\frac{\partial\left(\rho U_j U_i\right)}{\partial x^j} = -\frac{\partial p}{\partial x^i} + \frac{\partial \tau_{ij}}{\partial x^j} + F_i \tag{5}$$

$$\frac{\partial\left(\rho U_j k\right)}{\partial x^j} = \frac{\partial}{\partial x^j}\left[\left(\mu + \frac{\mu_t}{\sigma_k}\right)\frac{\partial k}{\partial x^j}\right] + P_k - \rho\varepsilon + S_{C_k} \tag{6}$$

$$\frac{\partial\left(\rho U_j \varepsilon\right)}{\partial x^j} = \frac{\partial}{\partial x^j}\left[\left(\mu + \frac{\mu_t}{\sigma_\varepsilon}\right)\frac{\partial \varepsilon}{\partial x^j}\right] + \frac{C_1\varepsilon}{k}P_k - \frac{C_2\rho\varepsilon^2}{k} + S_{C_\varepsilon} \tag{7}$$

where U_i is the Cartesian component of the velocity in the x^i direction, ρ and μ represent the air density and dynamic or turbulence viscosity ($\mu_t = \rho\, C_\mu k^2/\varepsilon$), and p is the pressure. τ_{ij} represents the Reynolds stress tensor, F_i(1) is a force term accounting for the effects of the canopy, P_k is the turbulence production term, and S_{C_k}(2) and S_{C_ε}(3) account for turbulence production and dissipation inside the canopy.

4. Numerical techniques

The computational domain was identical to that of the LES [4], both in size ($40h_c$ in the streamwise, x, and $8h_c$ vertical, z, directions), Fig. 1, and mesh type—structured, with regular

control volumes in the x-direction, and in z up to $z = 3h_c = 72$ m, above which a constant geometric expansion factor (f_z) was employed. Mesh resolution differed from the LES, and a mesh sensitivity study was carried out (Section 4.2).

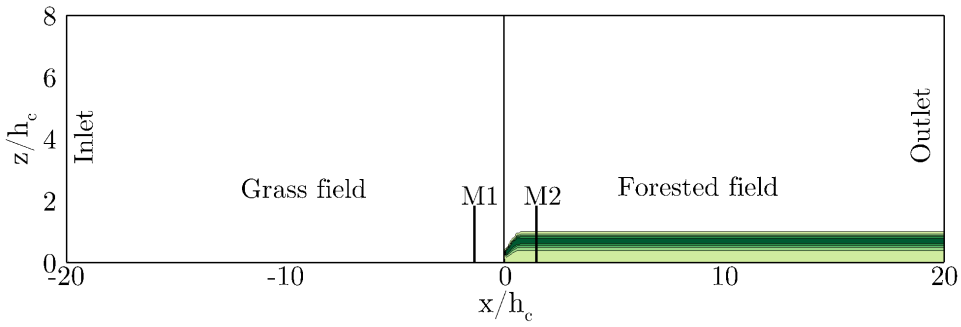


Figure 1: Computational domain, with the forested region and mast locations.

The inlet conditions, as in Ref. [17], were: $u(z) = u_* \log(1 + z/z_0)/\kappa$, $k = u_*^2/\sqrt{C_\mu}$ and $\varepsilon = u_*^3/(\kappa(z + z_0))$, where u_* and z_0 (Section 4.1) are the friction velocity and aerodynamic roughness length, and $\kappa = 0.4$ is the von Kárman constant. The ground was modelled as a rough surface with constant tangential Reynolds stress ($\sigma_t = \rho u_*^2$) and log-law tangential velocity. Constant shear stress and zero gradients for turbulent kinetic energy and its dissipation rate were considered at the top boundary.

4.1. Inlet conditions calibration

The inlet conditions ($u_* = 0.6$ m s^{-1} and $z_0 = 0.2$ m) were set so that streamwise velocity and turbulent kinetic energy, normalised with a streamwise velocity component (U_{ref}) at 30.9 m height on the M1 mast position [4], could replicate (root mean square error, RMSE = 0.016 and 0.001, Appendix A) the experimental values at M1 (Fig. 2). This combination is close to the values observed in the site: a friction velocity ($u_* = k^{0.5} C_\mu^{0.25}$) equal to 0.7 m s^{-1}, and a roughness length (z_0) of 0.3 m, estimated (coefficient of determination, $R^2 = 0.94$) via logarithmic fitting of function $U/u_* = 1/\kappa \log(z/z_0)$.

4.2. Grid refinement

To assess mesh sensitivity, Coarse, Medium, and Fine meshes (Table 2) were defined by doubling the spatial resolution in all directions, starting with $\Delta_x = 8$ m and $\Delta_z = 4$ m for the coarser mesh, down to 2 m horizontally and 1 m vertically for the finest mesh.

Table 2: Domain and grid characteristics for the grid sensitivity tests.

Grid	Nodes	Δ_x	Δ_z	f_z
Coarse	60×48	8 m	4 m	1.0075
Medium	120×96	4 m	2 m	1.0018
Fine	240×192	2 m	1 m	1.0004

Figure 3 conveys the effect of grid refinement on the wind speed and TKE profiles at $x = 1.5h_c$ downstream of the edge. The impact is greater near the ground and tree-top, where the Coarse mesh results stand out from the other two, namely for the TKE. The increasing TKE with grid resolution at the tree-top can also be observed in Ref. [14].

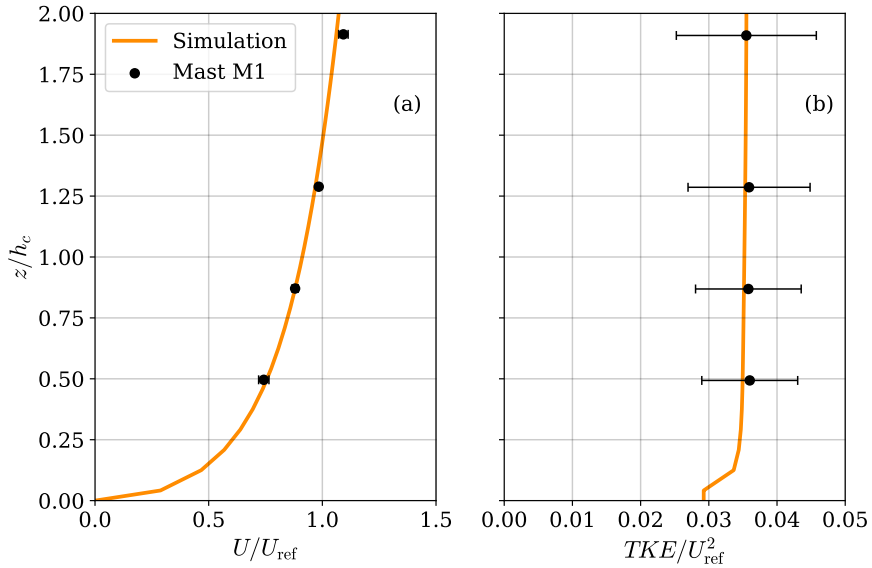


Figure 2: Longitudinal velocity (a) and turbulent kinetic energy (b) at mast M1. The black horizontal lines are the error bars as in [15].

The results were insensitive to mesh refinement above $z = 1.3h_c$. The Medium mesh was selected for the model comparison since it yielded similar results to the Fine mesh, with differences of 0.3% and 3.8% for U and TKE.

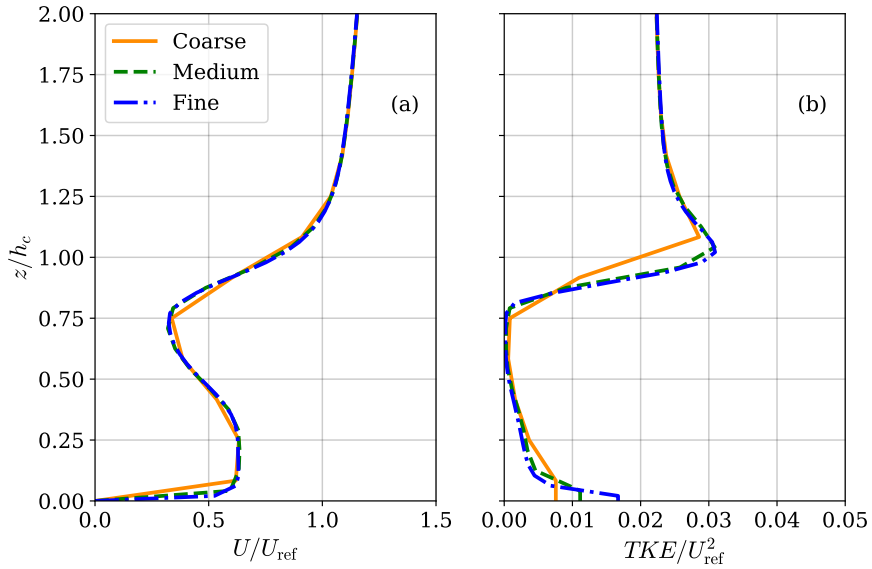


Figure 3: Mesh impact for the high-LAI period at $x = 1.5h_c$: normalised (a) U and (b) TKE.

4.3. Canopy description

The LAD (or $a(z)$, Fig. 4) is represented by a smooth, span-wise averaged distribution to reduce the heterogeneity inherent to the forest at the site [4]. Defined initially in $\Delta z = 1$ m vertical bins, $a(z)$ was redistributed to the computational mesh through a polynomial fitting, guaranteeing

the preservation of the leaf area index. The maximum forest height was fixed at 24 m, the average at the site. The drag coefficient C_d was set to 0.2 [4] and a roughness length of 0.2 m was used for the whole domain.

In the leading 48 m of the forest edge, the forest height follows an approximately parabolic shape, varying between 11 m and 24 m [4, 15]. In this region, the LAD polynomial was re-scaled from 24 m to the local height to preserve the forest characteristic LAI of 6 $m^2\,m^{-2}$.

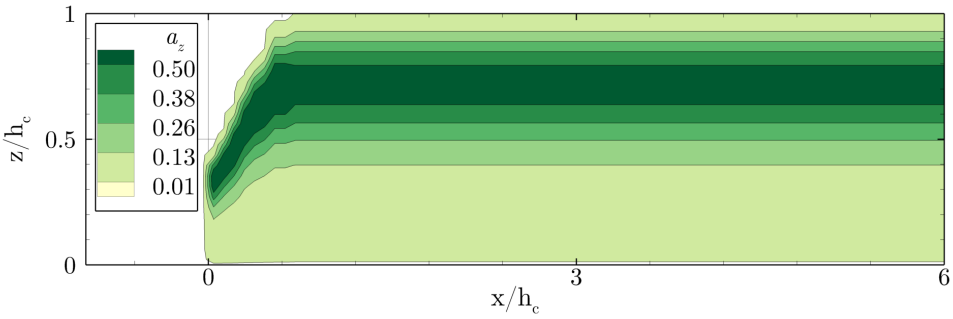


Figure 4: Leaf area density ($m^2\,m^{-3}$) of the forest, mapped onto the fine mesh.

5. Results and discussion

The root mean square error and Bias (see Appendix A) between the RANS k-ε and measurement results of normalised (Section 4.1) streamwise velocity, TKE, and Reynolds shear stress ($u'w'$) at mast M2 (Fig. 5) were the indicators of the models' quality. Additionally, the LES results [4], of which only U and $u'w'$ were available, were compared against our RANS simulations.

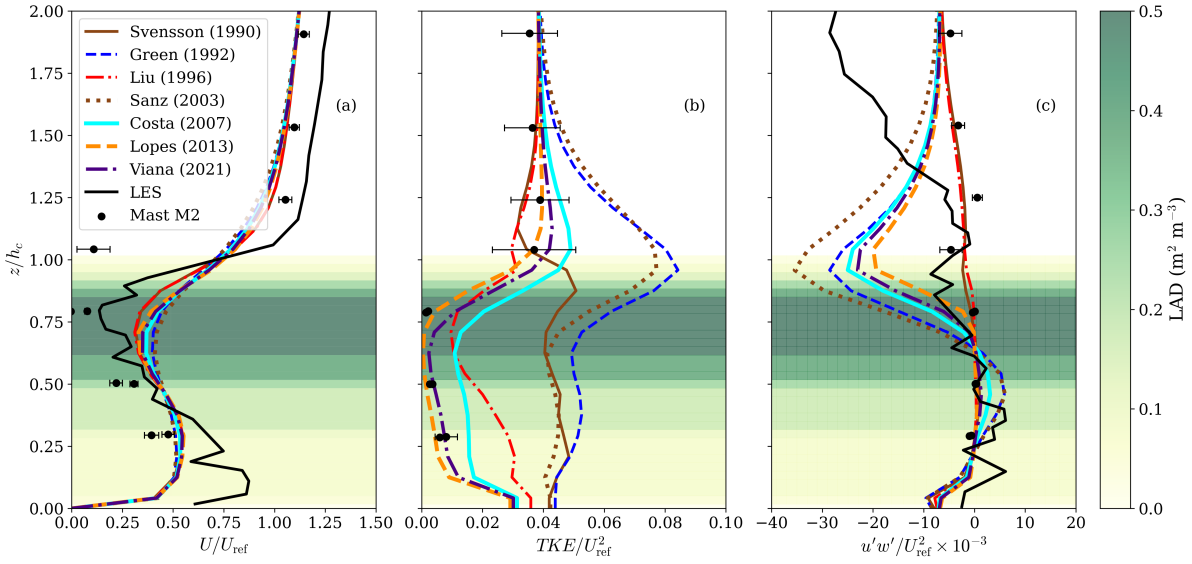


Figure 5: Measurements and computational results at M2: (a) streamwise velocity; (b) turbulent kinetic energy; (c) Reynolds shear stress. The black horizontal lines are the error bars.

Regarding streamwise velocity (Fig. 5a), all models showed similar trends and maximum and minimum values at $z/h_c \approx 0.2$ and 0.7 in regions of low and high foliage density. The LES results better resembled the experimental minimum wind speed at $z/h_c = 0.8$, but they

deviated the most from the maximum measured wind speed inside the forest (at $z/h_c = 0.3$). Above $z = 1.5h_c$, the forest's effect on U is negligible. The differences among the models are shown mainly in the turbulent field, where in the case of turbulent kinetic energy (Fig. 5b), four models (Lopes, Viana, Costa, and Liu) displayed a trend similar to the experimental data and different from the remaining three (Svensson, Sanz and Green), whereas in the case of the shear stress, only Svensson and Liu, together with the LES, resembled the measured values (Fig. 5c).

The models' performance based on RMSE and Bias (Table 3) showed that, when predicting the velocity, all models were similar, with RMSE and Bias of approximately 0.30 and 0.16. In the case of TKE, models Lopes and Viana allowed for RMSE (Bias) values to be accurate down to the third decimal digit, equal to 0.002 (0.001) and 0.004 (0.004). The remaining five models, however, displayed slightly higher RMSE: 0.01 with Costa and Liu, and ≈ 0.03 with Svensson, Green, and Sanz. Liu and Svensson depicted the lowest RMSE for $\overline{u'w'}$ (1.756 and 1.609), followed by Lopes with 7.951, while the remaining models displayed RMSE > 9.

Table 3: RMSE and Bias at mast M2.

	Model	RMSE	Bias
U/U_{ref}	Svensson (1990)	**0.291**	**0.156**
	Green (1992)	0.299	0.153
	Liu (1996)	**0.293**	**0.156**
	Sanz (2003)	0.303	0.152
	Costa (2007)	0.302	0.158
	Lopes (2013)	0.304	0.161
	Viana (2021)	0.304	0.160
	LES [4]	<u>0.333</u>	<u>0.230</u>
$\text{TKE}/U_{\text{ref}}^2$	Svensson (1990)	0.027	0.017
	Green (1992)	<u>0.038</u>	<u>0.033</u>
	Liu (1996)	0.011	0.006
	Sanz (2003)	0.034	0.030
	Costa (2007)	0.010	0.009
	Lopes (2013)	**0.002**	**0.001**
	Viana (2021)	**0.004**	**0.004**
	LES [4]	-	-
$\overline{u'w'}/U_{\text{ref}}^2$	Svensson (1990)	**1.609**	**-0.204**
	Green (1992)	11.904	-7.444
	Liu (1996)	**1.756**	**-0.370**
	Sanz (2003)	<u>15.405</u>	<u>-9.987</u>
	Costa (2007)	10.213	-6.720
	Lopes (2013)	7.951	-5.248
	Viana (2021)	9.253	-6.271
	LES [4]	10.922	-5.548

Note: The best values are in bold, and the worst are underlined.

The similarity found in U, TKE, and $\overline{u'w'}$ between some models can also be seen by the contributions of the S_k and k-ε terms in the equations for k and ε (Fig. 6). Sanz and Green performed as a source term up to the canopy midpoint and as a sink up to $\approx 0.95h_c$. Lopes and Viana acted exclusively as sink terms in both equations, whereas Liu and Svensson acted as source terms. At the top 20% of the canopy, the contribution of S_ε from these two former

models in the ε equation was almost 43 times greater than the other models.

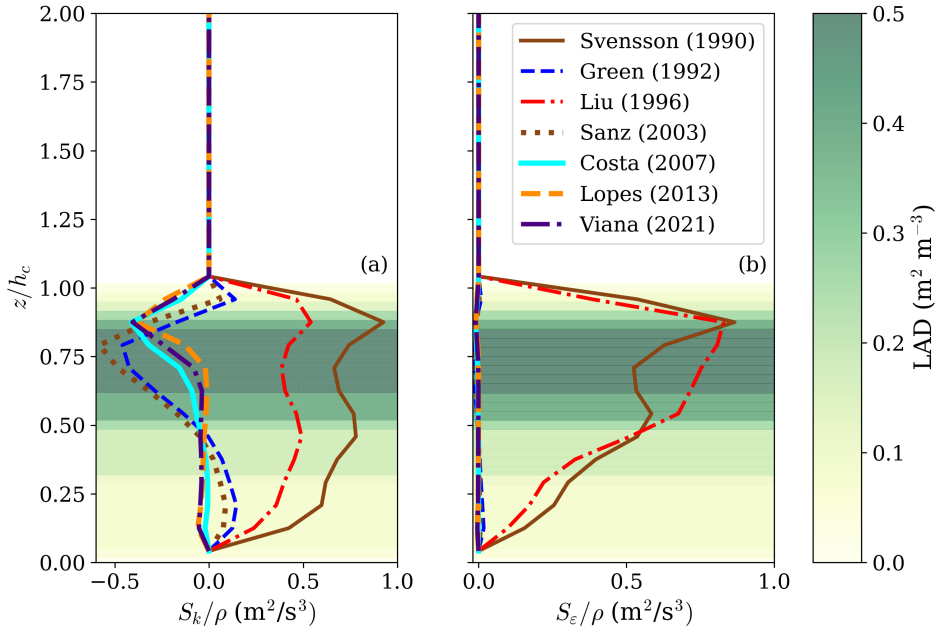


Figure 6: Canopy contribution for k (a) and ε (b) transport equations.

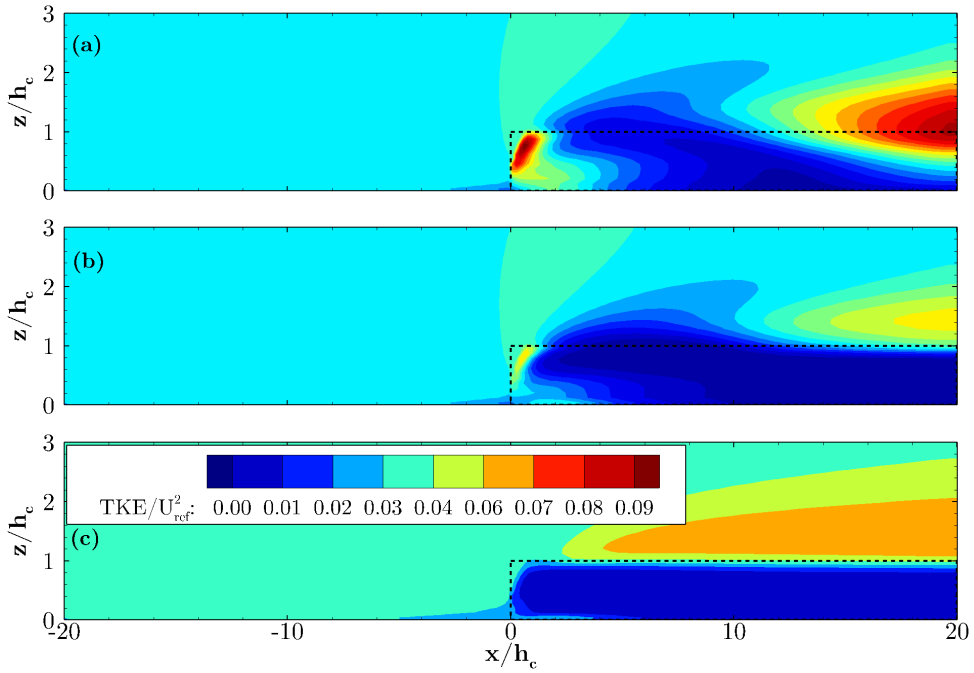


Figure 7: Turbulent kinetic energy along domain: (a) Svensson; (b) Liu; (c) Lopes.

The spatial distribution of k and $u'w'$ (Figs 7 and 8) is presented for the Svensson, Liu, and Lopes models due to their good performance at M2 (Table 3). A turbulent area developed above the canopy ($1 \leq z/h_c \leq 2.4$ at $x/h_c > 10$) for Liu (Fig. 7b), while for Lopes (Fig. 7c), the development of this area started earlier ($x/h_c > 3$, $1 \leq z/h_c \leq 2.8$), similarly to what was

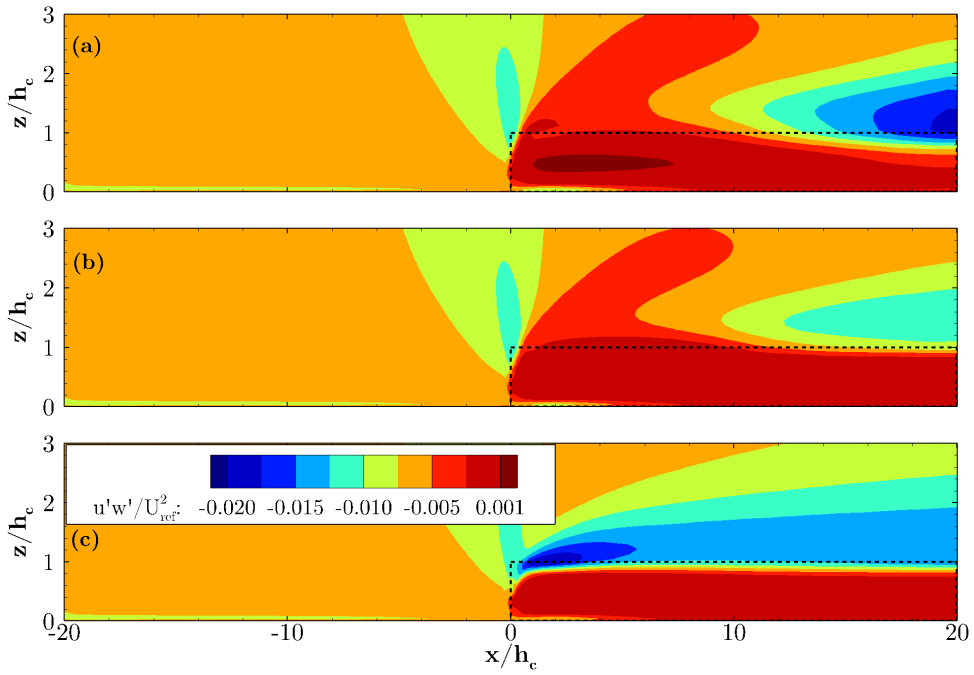


Figure 8: Reynolds shear stress along domain: (a) Svensson; (b) Liu; (c) Lopes.

observed in the LES simulations [4]. The Svensson model showed a similar region inside the canopy ($0.5 \leq z/h_c \leq 2.2$ at $x/h_c > 15$), with a higher TKE that can be related to the lack of sink term ($\beta_d = 0$), This contrasts with the expected turbulence dampening as the foliage generates small wake eddies, increasing the turbulence dissipation rate [3, 4]. However, the damping of TKE for Svensson and Liu was noticeable out of the canopy due to the very high contribution of the dissipation term on the k equation (6) within the canopy below. A layer of positive turbulent momentum flux (Fig. 8) developed from the edge for all models, which may be associated with the high shear of the sub-canopy wind jet.

The appropriateness of each model and its dependence on the variable in focus can be related to how the models were derived. For example, in the case of Svensson, $C_{\epsilon 4}$ was adjusted to find a good fit of the mean wind speed and the Reynolds shear stress [9], thus resulting in its improved Reynolds stress and wind speed performance. The Liu model was obtained by adjusting the dissipative term S_ε (3) to better represent the eddy viscosity, considering a constant mixing length scale [11]. Since μ_t is central to the RANS k-ε turbulence model, its tuning is crucial for a good overall performance, as observed for the Liu model. The Lopes model constants [14] were obtained for maximum correlation between RANS and LES canopy drag contributions to the budgets of TKE and ε, resulting in its excellent performance for TKE. The underestimation near the ground, as in Fig. 5, is a recognised shortcoming of this model [14] and can be related to the underestimation of the turbulent transport term in the same region.

Additional differences between simulation results and measurements can be related to the absence of forest inhomogeneities. Forest inhomogeneities impact the dynamics of the flow and, as Ref. [4] concluded, should be considered when studying canopy–atmosphere exchanges in edge regions.

6. Conclusion

Seven canopy models were evaluated in neutrally stratified flow over flat terrain covered by a forest in an edge configuration. Appropriate source and sink terms represented the interaction

between the forest and the atmosphere in the transport equations of TKE and its dissipation rate (k-ε), and a body force in the momentum equations. The simulations replicated the conditions observed in a site with available measurement datasets used for benchmarking. Results of the wind speed, turbulent kinetic energy and Reynolds shear stress showed:

- The streamwise velocity, U, was similar for all models.
- The Lopes [14] model yielded improvements in TKE prediction compared to other models.
- The Liu [11] and Svensson [9] models showed to be ideal for representing the Reynolds shear stress profile.
- The performance of models Liu and Svensson regarding wind speed and Reynolds stress were very similar. However, due to Svensson's overestimation of TKE inside the canopy, it is fair to say that the Liu model could suitably replace the former.

Based on the performance of each of the seven models in a forest edge configuration, Liu was the best at predicting wind speed, turbulent kinetic energy, and shear stress. However, finding a single model that could predict both the mean and turbulent flow regardless of the flow configuration (homogeneous, edge, and hill) or plant species is the subject of future work.

Acknowledgments
This research was funded by the Ministry of Higher Education, Science, Technology and Innovation (MESCTI) of Angola.

Appendix A. Error measures

The statistical variables considered in this study were root mean square error (RMSE) and Bias

$$\text{RMSE} = \sqrt{\frac{1}{n}\sum_{j=0}^{n}(\omega_j - \phi_j)^2} \tag{A.1}$$

$$\text{Bias} = \frac{1}{n}\sum_{j=0}^{n}(\omega_j - \phi_j) \tag{A.2}$$

where n is the number of points of the measured variable ω_j, and ϕ_j is the result of the predictions.

References

[1] Brunet Y 2020 *Bound.-Lay. Meteorol.* **177** 315–364
[2] Yang B, Raupach M R, Shaw R H, Tha Paw U K and Morse A P 2006 *Bound.-Lay. Meteorol.* **120** 377–412
[3] Dupont S, Bonnefond J M, Irvine M R, Lamaud E and Brunet Y 2011 *Agric. For. Meteorol.* **151** 328–344
[4] Boudreault L E, Dupont S, Bechmann A and Dellwik E 2017 *Bound.-Lay. Meteorol.* **162** 375–400
[5] Costa J C L, Castro F A, Palma J M L M and Stuart P 2006 *J. Wind Eng. Ind. Aerodyn.* **94** 603–620
[6] Enevoldsen P 2016 *Renew. Sust. Energ. Rev.* **60** 1251–1262
[7] Lopes J M V P, Palma J M L M and Lopes A S 2021 *J. Fluid Mech.* **910** 7–24
[8] Katul G G, Mahrt L, Poggi D and Sanz C 2004 *Bound.-Lay. Meteorol.*
[9] Svensson U and Häggkvist K 1990 *J. Wind Eng. Ind. Aerodyn.* **35** 201–211
[10] Green S R 1992 *PHOENICS J. Comput. Fluid Dyn. its Appl.* **5** 294–312
[11] Liu J, Chen J M, Black T A and Novak M D 1996 *Bound.-Lay. Meteorol.* **77** 2–44
[12] Sanz C 2003 *Bound.-Lay. Meteorol.* **108** 191–197
[13] Costa J C P L 2007 *Atmospheric Flow over Forested and Non-forested Complex Terrain* Ph.D. thesis University of Porto
[14] Silva Lopes A, Palma J and Lopes J V 2013 *Bound.-Lay. Meteorol.* **149** 231–257
[15] Dellwik E, Bingöl F and Mann J 2014 *Q. J. R. Meteorol. Soc.* **140** 676–686
[16] Castro F A, Palma J M L M and Lopes A S 2003 *Bound.-Lay. Meteorol.* **107** 501–530
[17] Richards P and Norris S 2011 *J. Wind Eng. Ind. Aerodyn.* **99** 257–266

D.2 Paper II-First Draft: Canopy models assessment near a forest edge in two configurations: flow towards and from the forest

Canopy models assessment over a forest edge in two configurations: flow towards and from the forest

Jesus R. Monteiro[1], Vasco T. P. Batista[1], José M. L. M. Palma[1], and Jakob Mann[2]

[1]Faculty of Engineering of the University of Porto (FEUP), Mechanical Engineering Department, Rua Dr. Roberto Frias, s/n, 4200-465 Porto, Portugal

[2]Technical University of Denmark – DTU Wind Energy, Frederiksborgvej 399, 4000 Roskilde, Denmark

Correspondence: Jesus R. Monteiro (jesus.monteiro@fe.up.pt)

Abstract. Computational modelling of atmospheric flows in forested areas is essential for wind resource assessment, farm design, and turbine siting in identifying low wind speed and high turbulence regions. In this study, using RANS with $k-\varepsilon$ turbulence model, we evaluated eight canopy models to determine which best simulates mean flow characteristics (velocity) and second-order flow statistics (turbulent kinetic energy and shear stress) by comparing against anemometer measurements of the flow towards and from a forest edge at the Island of Falster. For the flow towards the forest, the models captured well-known features, including (1) strong damping of wind and turbulence inside the forest, which, in the case of turbulent kinetic energy (TKE) damping, some models did not represent, (2) a sub-canopy wind jet due to low canopy leaf density, (3) a high TKE near the upper canopy due to large wind shear, which is associated to the canopy leaf density concentration, (4) early onset of the internal boundary layer above the forest at $1.04h_c$ for some models, and (5) a positive turbulent momentum flux layer inside the canopy from the edge, with a high momentum flux above it. For the flow from the forest, models reproduced: (1) wind speed damping and sub-canopy wind jet, (2) a residual flow separation zone at downwind edge, (3) high TKE layer above the canopy, extending up to $20h_c$ downstream, while within the forest, the canopy acts as a sink, effectively damping TKE, and (4) a layer of positive momentum flux inside the canopy, above it, large downward momentum flux develops in regions with no well-defined internal boundary layer. Overall, models that account only for the fraction of turbulent kinetic energy dissipated by short-circuiting the energy cascade tend to better replicate the behaviour of turbulent kinetic energy.

Copyright statement. TEXT

1 Introduction

Computational modelling of atmospheric flows in forested areas is essential at every stage of wind energy development, from wind resource assessment to wind farm location, design–including turbine selection and siting–and operation. Canopy models must reliably predict mean and turbulent fields, as poor-quality predictions can lead to incorrect decisions on turbine location and suboptimal wind farm operation.

In the case of the flow over a flat surface towards a deep forest, a highly turbulent layer develops from the leading edge over the canopy, with a wind jet at the canopy sub-layer (trunk space), and the flow equilibrium is expected after twenty canopy heights (Dupont et al., 2011). In contrast, when developed (equilibrium) flow over the trees encounters the forest edge, typically, three regions form downwind of the edge: (1) an initial region where the streamwise velocity profiles exhibit an inflexion point near the canopy top, with a recirculation zone underneath extending over a length of $2-5$ tree-height (h_c); (2) a mixing zone where the velocity profile becomes smoother; and (3) the re-equilibrium zone, usually after $5h_c$, where the mean wind velocity profile assumes a logarithmic form. The flow characteristics on the clearing side, however, depend on various factors, including forest density and height (Belcher et al., 2003; Detto et al., 2008). For dense and tall forests, the flow resembles a backwards-facing step flow (Raupach et al., 1987; Detto et al., 2008).

Large-eddy simulations (LES) can effectively model the complex turbulent flow in these two configurations concerning the transition between two developed and equilibrium flows: from developed over a canopy to developing over the clearing, and vice-versa, from developed over the clearing to developing over the forest; i.e., either flow towards or from the forest. However, in wind energy applications (e.g.; Costa et al., 2006; Enevoldsen, 2016), due to the computational cost of LES, Reynolds-averaged Navier-Stokes (RANS) with k-ε turbulence model is usually employed with additional terms –(7), (8) and (9) in the momentum (2), turbulent kinetic energy (3) and its dissipation rate (ε) (4), respectively. This approach, with its roots in Svensson and Häggkvist (1990), has originated many combinations of its six parameters, as listed in Lopes et al. (2021), of which eight (in Table 1) were selected to evaluate their performance for simulating the mean and turbulent flow characteristics.

The early RANS k-ε models were based on wind tunnel data to determine the model constants. Svensson and Häggkvist (1990) simulated the mean velocity, shear stress, and turbulence intensity over a homogeneous forest by representing the canopy mainly as a source of turbulence, without explicitly accounting for the additional dissipation induced by vegetation elements. This limitation was later addressed by Green (1992), who introduced an enhanced canopy-related dissipation mechanism. Building on this work, Liu et al. (1996) showed that this formulation tended to overestimate eddy viscosity (μ_t) downstream of a forest edge and proposed a revised balance that strengthened the role of canopy-induced dissipation. In contrast, Sanz (2003) derived model parameters from an analytical solution of the flow within a dense and homogeneous canopy, far enough from any boundary (where the mixing length does not vary significantly), leading to the strongest dissipation contribution among the available formulations. The model proposed by Costa (2007) follows a similar approach, as its validation relied on the same analytical framework complemented by LES results.

According to Lopes et al. (2013), the canopy primarily acts as a mechanism that enhances turbulence dissipation, whereas in the formulation proposed by Svensson and Häggkvist (1990) the canopy contribution is associated mainly with increased

turbulence production. The remaining models account for both mechanisms, with the relative balance between production and dissipation governed by different combinations of model parameters. In Lopes et al. (2021), the canopy-related source terms in equations (2), (3), and (4) were derived using a Taylor-series expansion of the velocity magnitude. This approach adopts a velocity scale based on the total kinetic energy and assumes a weak-turbulence regime, in which turbulent fluctuations are small compared to the mean-flow velocity magnitude

Sogachev and Panferov (2006), Sogachev (2009), and Sogachev et al. (2012) assume that, within the canopy, the production and dissipation of turbulent kinetic energy (TKE) due to plant drag are in local equilibrium. Under this assumption, the TKE equation does not require additional source or sink terms, as the canopy-induced production of turbulence is considered to be balanced by an equivalent dissipation through short-circuiting of the energy cascade. The equilibrium assumption, although convenient, contradicts the established knowledge (cf., Finnigan, 2000) that turbulence inside the canopy is far from local equilibrium, being mainly transported from above. Sogachev's approach and understanding of the canopy flow are not consistent with the previous studies, not only by disregarding any contribution of the canopy to the TKE equation but also because represents the canopy effect in the dissipation equation as a positive source term, identical to the sink type term suggested by all others.

Unlike most studies of edge flow that rely on wind tunnels and numerical experiments (Lopes et al., 2013), in this study, we use field measurements of flow towards (Dellwik et al., 2014) and from forest (subsection 2.1). We aimed to identify one of eight canopy models (Table 1) across a forest edge on flat terrain, where the RANS results of streamwise velocity, turbulent kinetic energy, and Reynolds shear stress best agreed with the field data. For this purpose, the fluid flow equations were solved for a neutrally stratified, statistically steady turbulent boundary layer.

The present study is an extension of Monteiro et al. (2024), including a deeper analysis of the atmospheric flow over a forest edge not only from open farmland towards the forest but also from the forest towards the open farmland.

In what follows, we present a brief description of the experimental data (Section 2), the fundamental equations of the mathematical models (Section 3), the numerical techniques (Section 4), the results and discussion (Section 5), and conclusions (Section 6).

2 Experimental data

The double-mast observations taken upwind and downwind from a dense, straight beech forest (Fagus Sylvatica L) edge on the Island of Falster (Dellwik et al., 2014) were used to appraise the two-dimensional canopy model. The experiment ran between February and mid-September 2008. Due to its extended length, there were sufficient observational results for both flows toward and from the forest edge for leaf-off and leaf-on conditions. The comparison is limited to the summer when the canopy was whole leaf. Whereas these summer observations have been extensively analysed for the case of the wind coming onto the edge (Dellwik et al., 2014; Mann and Dellwik, 2014; Boudreault et al., 2017; Dellwik et al., 2023), the flow statistics from forest to the open farmland are published here for the first time. Based on the characteristics of windy and overcast weather at the site, the observations are well suited for comparison with flow models assuming neutral temperature stratification.

The two masts of 45.9 m height were located at approximately $1.5h_c$ upstream from the forest's leading edge in open farmland (M1) and approximately $1.5h_c$ from the edge inside the forest (M2). The M1 and M2 had 4 and 14 sonic anemometers (USA-1, Metek Gmbh, Germany), respectively. The trees at the location of the M2 mast had a height, h_c, of approximately 24 m at the time of the experiment. The leaf area index (LAI $= \int_0^{h_c} a(z)dz$) was measured using a Plant Canopy Analyser (PCAs; LI-COR, Lincoln, NE, USA) over a line extending 360 m perpendicular to the edge, resulting in a mean value of 6 $\mathrm{m^2 m^{-2}}$. More details of the experimental site can be found in Dellwik et al. (2014) and Arnqvist et al. (2020).

To provide an accurate high-detail description of the forest edge geometry and density as input to the tested RANS models described above, we used the raw data from airborne lidar scans from the summer of 2013. These were processed to achieve a three-dimensionally varying plant area density using the algorithm of "scaled ratios" from Arnqvist et al. (2020), which is less prone to overestimation and less sensitive to spatial averaging compared to the "First Return" method used by Boudreault et al. (2017), see the discussion in Arnqvist et al. (2020) for further details. The spatial resolution of the vegetation layer was set to $\Delta z = 1$ m in the vertical and $\Delta x = \Delta y = 8$ m. The resulting LAI estimates agreed with the LAI observations from the Plant Canopy Analyser data for the range 50-150 m inside the forest. The lidar data were subsequently scaled to account for the estimated forest growth of 0.2 m per year between the field experiment in 2008 and the forest scanning in 2013.

2.1 Definition of forest edge validation datasets

The raw data from the sonic anemometers were first post-processed to correct for flow distortion caused by the sonic anemometer itself (Bechmann et al., 2009), and cross-wind effects on the anemometers' temperature signal (Liu et al., 2001). Further, the time series were despiked with carefully selected thresholds based on manual inspection of all the 20 Hz time series. Subsequently, the data were rotated into the mean wind direction at a reference position, which was the 30.9 m height at M1 for the case of field $\rightarrow$ forest and the 30 m on M2 for the forest $\rightarrow$ field case. First, second and third-order moments were calculated based on ten-minute intervals, and the derived quantities of Obukhov length and friction velocity were also calculated. Finally, validation data were selected based on the following criteria:

- **Perpendicular to the edge**: Reference point wind directions between 280 and 300 degrees (field $\rightarrow$ forest) or 100 to 120 degrees (forest $\rightarrow$ field).
- **Near-neutral atmospheric stratification**: $-0.1 \leq z/L \leq 0.07$ and $U_{ref} > U_0$, where U_0 was set to 5.5 $\mathrm{ms^{-1}}$ for the field $\rightarrow$ forest and 4 $\mathrm{m}s^{-1}$ for the forest $\rightarrow$ field case.

This selection resulted in 124 and 79 ten-minute data series for the field $\rightarrow$ forest and forest $\rightarrow$ field case, respectively. The used resulting statistics are given in Appendix A???

3 Governing equations

VENTOS-2D model, a two-dimensional version of VENTOS®/2 CFD (Castro et al., 2003), was used to solve the RANS equations of mass (1), momentum (2) and k-ε turbulence model (3,4) for a turbulent flow under a neutrally stratified atmosphere:

$$\frac{\partial(\rho U_i)}{\partial x_i} = 0 \tag{1}$$

$$\frac{\partial(\rho U_i U_j)}{\partial x_j} = -\frac{\partial p}{\partial x_i} + \frac{\partial}{\partial x_j}\left(\tau_{ij} + \rho\overline{u_i' u_j'}\right) + F_i \tag{2}$$

$$\frac{\partial(\rho U_j k)}{\partial x_j} = \frac{\partial}{\partial x_j}\left[\left(\mu + \frac{\mu_t}{\sigma_k}\right)\frac{\partial k}{\partial x_j}\right] + P_k - \rho\varepsilon + S_{C_k} \tag{3}$$

$$\frac{\partial(\rho U_j \varepsilon)}{\partial x_j} = \frac{\partial}{\partial x_j}\left[\left(\mu + \frac{\mu_t}{\sigma_\varepsilon}\right)\frac{\partial \varepsilon}{\partial x_j}\right] + \frac{C_1 \varepsilon}{k} P_k - \frac{C_2 \rho \varepsilon^2}{k} + S_{C_\varepsilon} \tag{4}$$

U_i is the Cartesian component of the velocity in the x_i direction, ρ and μ represent the air density and dynamic or turbulence viscosity ($\mu_t = \rho C_\mu k^2/\varepsilon$), and p is the pressure. τ_{ij} is the viscous stress tensor, F_i (7) is a force term accounting for the effects of the canopy, P_k is the turbulence production term (5), and S_{C_k}(8) and S_{C_ε}(9) or (10) account for turbulence production and dissipation inside the canopy.

$$P_k = \rho\overline{u_i' u_j'}\frac{\partial U_i}{\partial x_j} \tag{5}$$

and the Boussinesq approach is used for the Reynolds stress tensor (6),

$$\rho\overline{u_i' u_j'} = -\frac{2}{3}\rho k \delta_{ij} + \mu_t\left(\frac{\partial U_i}{\partial x_j} + \frac{\partial U_j}{\partial x_i}\right) \tag{6}$$

3.1 Canopy model

The VENTOS-2D solvers incorporate the canopy model by including the aerodynamic drag force, F_i (7), within the momentum equation (2). Additionally, the canopy influences turbulence through source terms S_{C_k} (8) in the turbulent kinetic energy equation (3) and S_{C_ε} (9) in the dissipation rate equation (4).

$$F_i = -\rho C_d\, a(x,z)\, |U|\, \overline{U_i} \tag{7}$$

$$S_{C_k} = \rho C_d\, a(x,z)\left(\beta_p |U|^3 - \beta_d |U| k\right) \tag{8}$$

$$S_{C_\varepsilon} = \rho C_d\, a(x,z)\left(C_{\varepsilon 4}\beta_p |U|^3 \frac{\varepsilon}{k} - C_{\varepsilon 5}\beta_d |U| \varepsilon\right) \tag{9}$$

F_i represents the drag force due to the canopy, and S_{C_k} and S_{C_ε} account for the net production of turbulent kinetic energy and its dissipation rate. C_d is the forest mean drag coefficient; $a(x,z)$, the leaf area density (LAD), represents the canopy leaves area per unit volume ($\mathrm{m^2 m^{-3}}$); β_p and β_d set the fraction of mean flow kinetic energy converted to turbulent kinetic energy (a source term) and the fraction of turbulent kinetic energy dissipated (a sink term) by short-circuiting of the energy cascade; and $C_{\epsilon 4}$ and $C_{\epsilon 5}$ adjust the effect of the canopy on the dissipation rate of turbulence.

For Sogachev and Panferov (2006), the canopy effects are only on equation (4) where the S_{C_ε} (10) (higher than zero) acts as a source, where β is a constant calibrated to fit observed wind profile (Sogachev et al., 2012), and $C_{\varepsilon 1}$ and $C_{\varepsilon 2}$ are the standard model coefficients in the production and destruction terms of the ε equation. In Table 1, the constants called Sogachev (2006) correspond to the same set of constants combination used in Dellwik et al. (2019).

$$S_{C_\varepsilon} = \rho C_d \, a(x,z) \, |U| \, \beta \sqrt{C_\mu} \, (C_{\varepsilon 2} - C_{\varepsilon 1}) \, k \, \frac{\varepsilon}{k} \tag{10}$$

Table 1. Canopy model coefficients for the RANS k-ε model.

Model	β_p	β_d	$C_{\varepsilon 4}$	$C_{\varepsilon 5}$	β	$C_{\varepsilon 1}$	$C_{\varepsilon 2}$
Svensson and Häggkvist (1990)	1.00	-	1.95	-	-	-	-
Green (1992)	1.00	4.00	1.50	1.50	-	-	-
Liu et al. (1996)	1.00	4.00	1.50	0.60	-	-	-
Sanz (2003)	1.00	5.10	0.90	0.90	-	-	-
Costa (2007)	0.17	3.37	0.90	0.90	-	-	
Lopes et al. (2013)	-	4.00	-	0.90			
Lopes et al. (2021)	-	2.67	-	1.00	-	-	-
Sogachev and Panferov (2006)	-	-	-	-	12.00	1.21	1.92

In Table 1 according to Svensson and Häggkvist (1990), the canopy enhances the production of turbulence kinetic energy and its dissipation, and additional source terms are required to add to their production. In the next four models, in Table 1, the effect of the trees is such that a fraction of the turbulence kinetic energy is locally and instantaneously dissipated, short-circuiting the energy cascade and the source term in TKE suggested by Svensson must be reduced by adding a negative term (i.e., a sink), which for consistency should also affect the ε equation. According to Lopes (2013) and Viana (2021), based on the LES reasoning and the impossibility of resolving the small and dissipative scales, the additional terms should account for the destruction of TKE and its dissipation rate.

4 Numerical techniques

4.1 Computational domain and canopy description

The computational domain had a size of $40h_c$ in the streamwise (x) direction and $8h_c$ in the vertical (z) direction (Fig. 1). The mesh was structured, with uniform spacing in x between -70 and 70 m, beyond which a geometric expansion factor f_x was applied. In the vertical direction, the grid was uniform up to $z = 3h_c = 72$ m, and above this height a geometric expansion factor f_z was used.

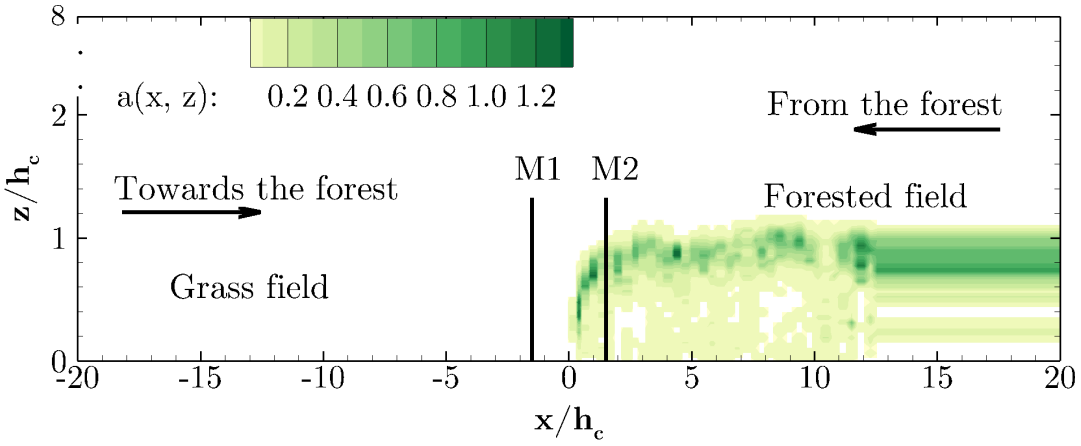


Figure 1. Computational domain of the flow towards and from the forest, with mast locations.

Two scenarios were considered, Fig. 1: a) flow towards the forest, and b) flow from the forest. The inlet conditions for the first scenario, as in Richards and Norris (2011), were: $u(z) = u_* \log(1 + z/z_0)/\kappa$, $k = u_*^2/\sqrt{C_\mu}$ and $\varepsilon = u_*^3/(\kappa(z + z_0))$, where u_* and z_0 are the friction velocity and aerodynamic roughness length, and $\kappa = 0.4$ is the von Kárman constant. The ground was modelled as a rough surface with constant tangential Reynolds stress ($\sigma_t = \rho u_*^2$) and log-law tangential velocity. Zero gradients for shear stress, turbulent kinetic energy and dissipation rate were considered at the top boundary. The second scenario utilised similar conditions to the first, but with velocity, TKE, and dissipation profiles imposed on the upwind side, differentiating it from scenario 1. These inlet profiles were obtained from an additional simulation of flow over a homogeneous forest using periodic boundary conditions in the streamwise direction, allowing the flow to reach a quasi-equilibrium state representative of fully developed forest-edge conditions.

The LAD described in Section 2, $a(x, z)$ in Fig. 1, was calculated as the median over a 40 m wide area in the y-direction to represent a realistic spatial variability. Defined initially in $\Delta x = 8$ m horizontal and $\Delta z = 1$ m vertical bins, $a(x, z)$ was redistributed to the computational mesh as heterogeneous up to $x = 292$ m, and homogeneous after it (the same values as in $x = 292$ m). The maximum forest height was fixed at 27.5 m, and the site average height at 24 m. The drag coefficient C_d was set to 0.2 (Boudreault et al., 2017), and a roughness length of 0.2 m was used for the whole domain (subsection 4.2).

4.2 Inlet conditions calibration

The first scenario inlet conditions were set so that streamwise velocity and turbulent kinetic energy, normalised with a streamwise velocity component (U_{ref}) at 30.9 m height on the M1 mast position (Boudreault et al., 2017), could replicate normalised experimental values at M1 (Fig. 2). The best combination ($u_* = 0.6$ ms^{-1} and $z_0 = 0.2$ m) minimised the root mean square error (11) and was close to the values observed at the site: a friction velocity ($u_* = k^{0.5} C_\mu^0$) and z_0 equal to 0.7 ms^{-1} and 0.3 m, estimated (coefficient of determination, $R^2 = 0.94$) via logarithmic fitting of function $U/u_* = 1/\kappa \log(z/z_0)$.

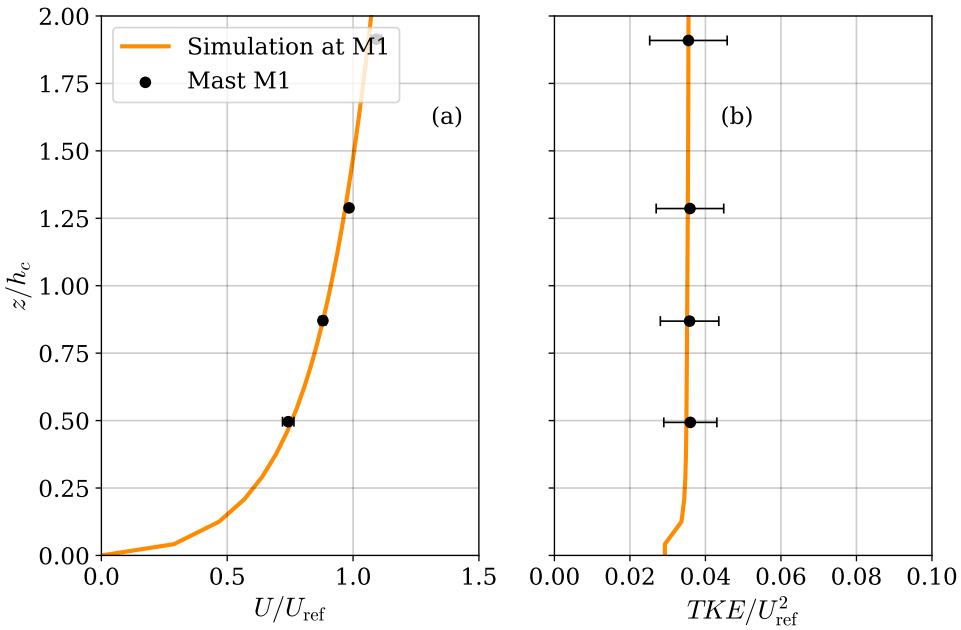


Figure 2. streamwise velocity (a) and turbulent kinetic energy (b) at Mast M1 for scenario 1. Black dots and horizontal lines are the measurement values and variability bars at M1 as in Dellwik et al. (2014).

In scenario 1, the upstream flow was not affected by the canopy model, so the main question was whether the boundary layer developed correctly. To set the inlet conditions for scenario 2, as in scenario 1, it is necessary to simulate the flow over the forested area using each canopy model. One approach is to model the flow over the actual forest length, using boundary conditions that match the measurements at M2. Another option is to simulate a very long forest until the flow reaches equilibrium. In both cases, the inlet profiles will differ depending on the canopy model, unlike scenario 1, where all models used the same inlet conditions. In this work, periodic boundary conditions in the streamwise direction were applied over a very long forest to generate the inlet profiles used for scenario 2 (Fig. 3). These profiles are normalised with the streamwise velocity at 30 m height on the M2 mast ($U_{\mathrm{ref}} = 5.07\ \mathrm{ms}^{-1}$).

4.3 Grid refinement

To assess mesh sensitivity, in the case of flow towards the forest, we performed calculations on three meshes (coarse, medium, and fine, Table 2 and Fig. 4) generated by successively doubling the spatial resolution in all directions. At $x = 1.5h_c$ downstream from the edge, the most significant impact of grid refinement was near the ground and at the tree-top level, particularly for TKE, which increased with higher grid resolution. The results were largely insensitive to mesh refinement above $z = 1.3h_c$. Ultimately, the medium mesh was selected for model comparison since its results were comparable to the fine mesh, with differences of only 0.3% for streamwise velocity (U) and 3.8% for TKE.

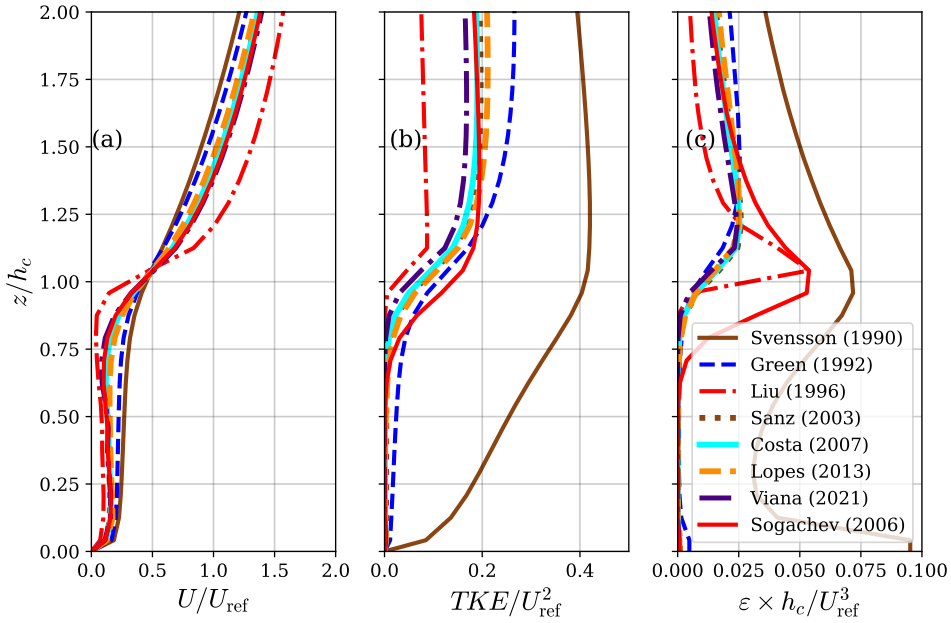


Figure 3. Streamwise velocity (a), turbulent kinetic energy (b) and (c) dissipation for scenario 2.

Table 2. Domain and grid characteristics for the grid sensitivity tests.

Grid	Nodes	Δ_x	Δ_z	f_z
coarse	60×48	8 m	4 m	1.0075
medium	120×96	4 m	2 m	1.0018
fine	240×192	2 m	1 m	1.0004

5 Results and discussion

The section describes the results of the flow towards (subsection 5.1) and from the forest (subsection 5.2). The root mean square error (11) and bias (12) between the RANS k-ε and measurement results (subsection 4.2) of streamwise velocity, TKE, and Reynolds shear stress ($\overline{u'w'}$) at mast M2 and M1 (Figs. 5, 9, and 10) were the indicators of the models' quality.

$$\mathrm{RMSE} = \sqrt{\frac{1}{n}\sum_{i=0}^{n}(\phi_i^m - \phi_i^c)^2} \tag{11}$$

$$\mathrm{Bias} = \frac{1}{n}\sum_{i=0}^{n}(\phi_i^m - \phi_i^c) \tag{12}$$

where the superscripts m and c stand for measurement and computational result of the n points of the variable ϕ.

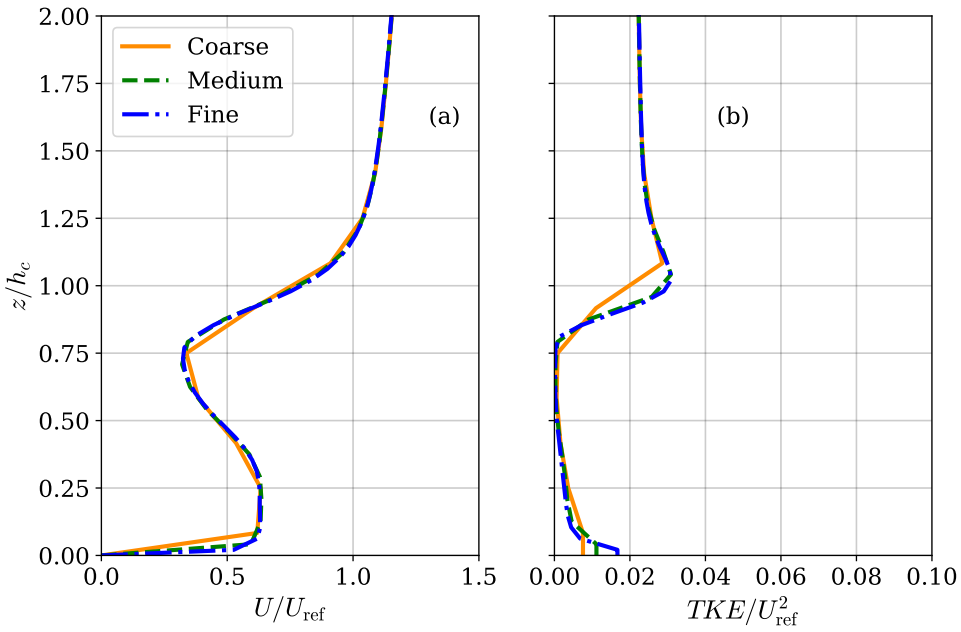


Figure 4. Mesh impact for the high-LAI period at $x = 1.5h_c$ (scenario 1, at Mast M2): (a) streamwise velocity; (b) turbulent kinetic energy.

5.1 Scenario 1: flow towards the forest

Regarding the streamwise velocity (Fig.5a), all models exhibited similar trends and well-known behaviour of the flow over canopy (see Yang et al. (2006); Dupont et al. (2011)), with maximum and minimum values occurring at $z/h_c \approx 0.2$ and 0.78, which correspond to regions of low and high foliage density, respectively. None of the models captures the $1.04h_c$ and $0.78h_c$ observations, which points to the misrepresentation of forest characteristics. The inflexion point is located at the canopy top, and above $z = 1.5h_c$, the forest's influence on U becomes negligible. Differences among the models were more pronounced in the turbulent field. For turbulent kinetic energy (TKE, Fig.5b), five models (Lopes, Viana, Costa, Liu, Sogachev) followed trends similar to experimental data, unlike the other three models (Svensson, Sanz, and Green), which overestimated the TKE. Regarding shear stress, only the Svensson and Liu models aligned with measured values (Fig. 5c). The models' turbulence flow characteristics, including high TKE at the top, positive momentum in the layer beneath the crown, and negative momentum below it, are similar to what was reported by Boudreault et al. (2017) and Dupont et al. (2011). It is important to emphasise that, unlike most models, both Svensson and Liu showed a reduction in momentum flux at the top canopy, which aligns with observational data.

The models' performance, evaluated using RMSE and Bias (Table 3), shows that most models predicted velocity with RMSE and Bias values around 0.30 and 0.10, respectively. For TKE, the Liu, Lopes and Viana models achieved lower RMSE (Bias): 0.005 (-0.001), 0.004 (0.001) and 0.005 (0.002), respectively. The remaining models showed slightly higher RMSEs, with the Costa and Sogachev model at around 0.007 and 0.009. Green exhibited even higher RMSEs at approximately 0.03, followed

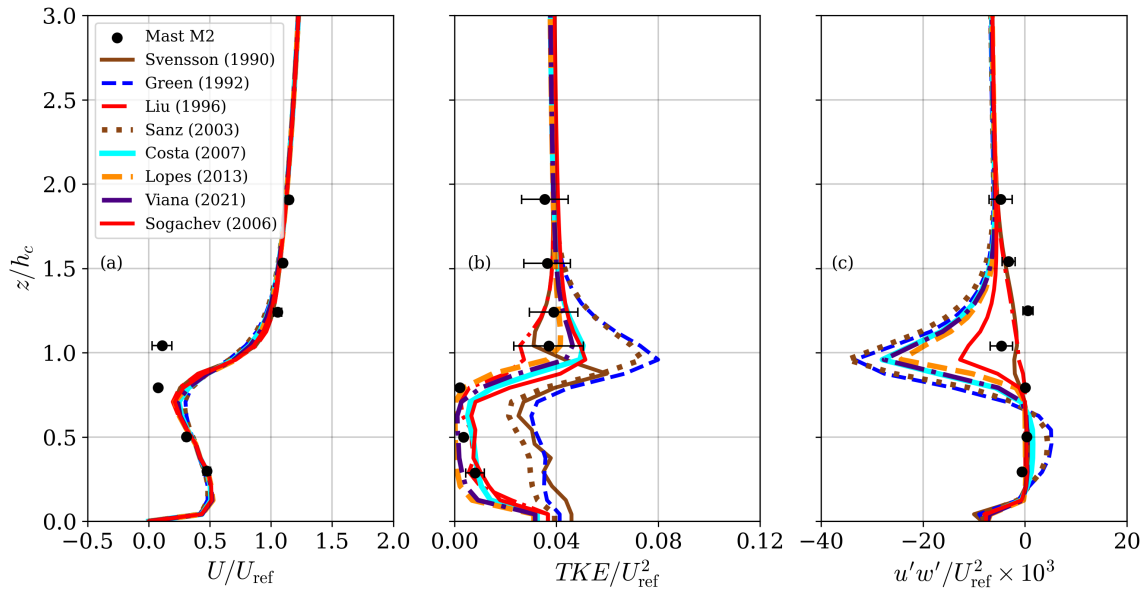


Figure 5. Measurements and computational results of flow towards the forest at M2: (a) streamwise velocity; (b) turbulent kinetic energy; (c) Reynolds shear stress. The black horizontal lines are the variability bars.

by Svensson and Sanz with 0.02. For shear stress ($\overline{u'w'}$), the Svensson and Liu models had the lowest RMSEs (0.0018 and 0.0017, respectively), followed by Sogachev at 0.004. The remaining models had RMSE at around 0.01.

Table 3. Flow towards the forest: RMSE and Bias at mas M2.

	U/U_{ref}		TKE/U^2_{ref}		$\overline{u'w'}/U^2_{\mathrm{ref}} \times 10^3$	
Model	RMSE	Bias	RMSE	Bias	RMSE	Bias
Svensson (1990)	0.283	0.136	0.022	0.015	**1.762**	**0.231**
Green (1992)	**0.267**	**0.123**	0.027	0.024	10.605	-5.075
Liu (1996)	0.284	0.137	**0.005**	**-0.001**	**1.685**	**-0.121**
Sanz (2003)	**0.268**	**0.125**	0.022	0.019	10.785	-5.315
Costa (2007)	0.275	0.131	0.007	0.006	8.016	-4.349
Lopes (2013)	0.279	0.134	**0.004**	**0.001**	6.749	-3.785
Viana (2021)	0.276	0.133	**0.005**	**0.002**	7.806	-4.550
Sogachev (2006)	0.281	0.136	0.009	0.007	3.716	-2.008

Note: The best values are in bold, and the worst are underlined.

The TKE and $\overline{u'w'}$ profiles are strongly related to the S_k and S_ε terms in the equations for k and ε (Fig. 6). Sanz and Green performed as a source term up to the canopy midpoint and as a sink up to $\approx 0.95h_c$. Lopes and Viana acted exclusively as sink

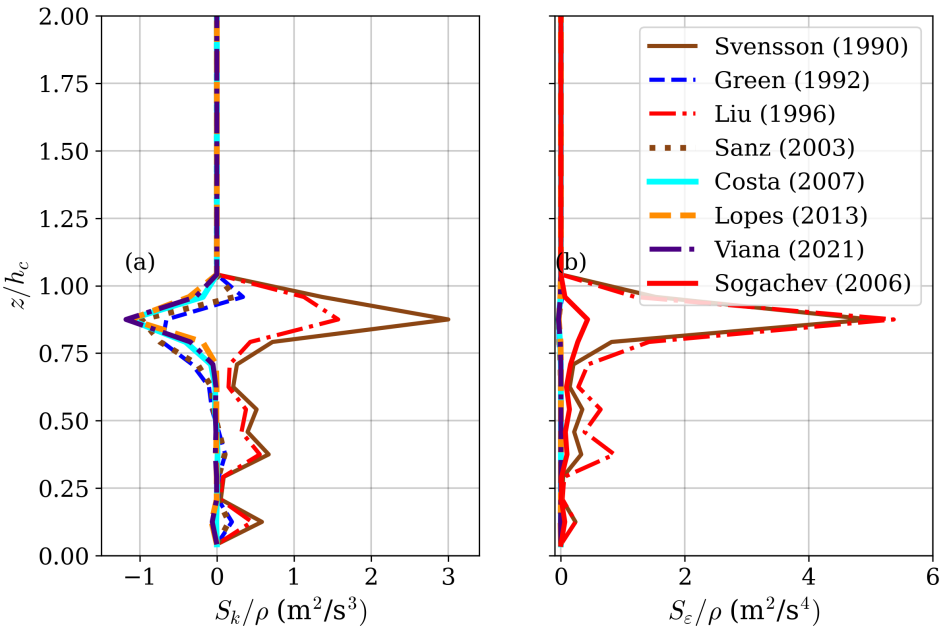


Figure 6. Canopy contribution for k (a) and ε (b) transport equations. Flow towards the forest.

terms in both equations, whereas Sogachev acted as source terms in the ε equation and the null contribution for the k equation. Liu and Svensson acted as source terms.

The spatial distribution of streamwise velocity, k, $\overline{u'w'}$ and length scale ($L_m = C_\mu^{3/4}\ k^{3/2}\ \varepsilon^{-1}$) (Fig. 7 and 8) is presented for all models to characterise the flow along the domain better. All models displayed similar streamwise velocity magnitude along the domain (Fig. 7a1, b1, c1, d1, e1, f1, g1 and h1), with velocity reduction up to $z/h_c \leq 1$ due to canopy presence, and accelerating above it. A flow deflection is observed near the edge, and in the sub-canopy layer, the models showed wind jets in areas with low leaf density. The large wind shear due to the canopy leaf concentration at the upper canopy originated a highly turbulent region development above the canopy ($1 \leq z/h_c \leq 2.8$ at $x/h_c > 9$) for Svensson and Liu (Fig. 7a2 and c2), which in the case of Green, Sanz, Costa and Sogachev starts at the edge (Fig. 7b2, d2 and e2, $1 \leq z/h_c \leq 3$), Lopes and Viana (Fig. 7f2 and g2) near the edge ($x/h_c \leq 1$, $1 \leq z/h_c \leq 3$). The turbulence is damped within the canopy, except for Svensson Green and Sanz, which showed a significant level of TKE. This contrasts with the expected turbulence dampening as the foliage generates small wake eddies, increasing the turbulence dissipation rate. However, this characteristic was previously reported by Dupont et al. (2011) in pine forests with a deep and sparse trunk space, which he associated with a shear layer below the crown layer. Results of Reynolds shear stress showed a layer of positive turbulent momentum flux developed within the canopy, from the edge for all models (Fig. 8a3, b3, c3, d3, e3, f3, g3 and h3), which may be associated with the sub-canopy wind jet. A high negative momentum flux develops above the canopy within the internal boundary layer. At the canopy top, Svensson and

Liu displayed momentum flux close to zero near the edge, whereas others predicted a higher shear stress magnitude. Similar findings of mean flow characteristics and second-order flow statistics were previously reported (Dupont et al., 2011; Dellwik et al., 2014; Boudreault et al., 2017). The model's turbulence length scale remains the same inside the forest (Fig. 8a4, b4, c4, d4, e4, f4, g4 and h4), with minor variations, except for Svensson, Green and Sanz, which is associated with the high level of turbulent kinetic energy inside the canopy.

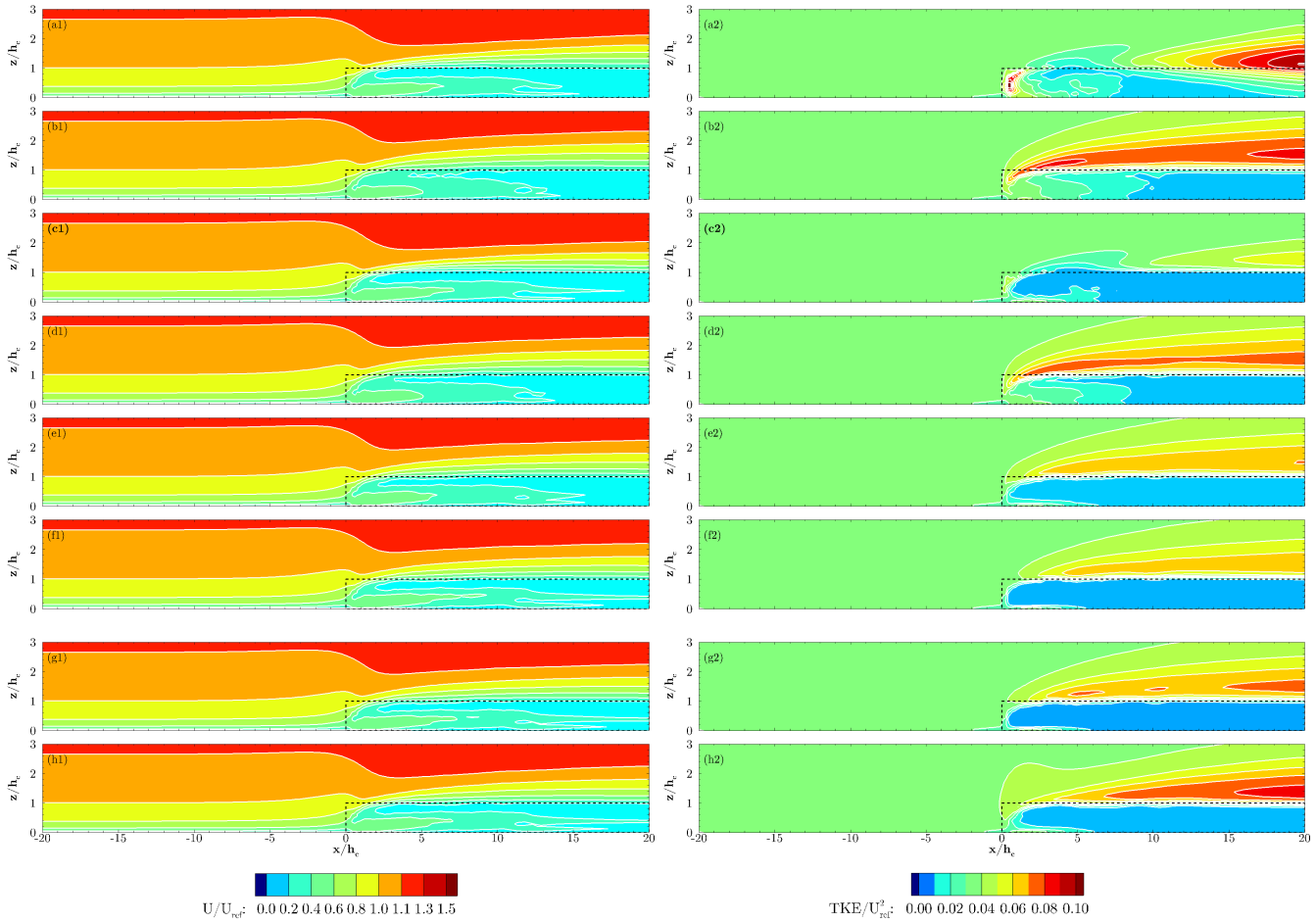


Figure 7. Scenario 1: mean streamwise velocity and turbulent kinetic energy (a) Svensson, (b) Green, (c) Liu, (d) Sanz, (e) Costa, (f) Lopes, (g) Viana, (h) Sogachev .

5.2 Scenario 2: flow from the forest

At M2 (Figures 9 and 10), the streamwise velocity peaks at $z/h_c = 0.2$ and reaches a minimum near 0.8, after which the flow begins to recover. At M1, recirculation is observed up to $z/h_c \leq 0.25$, except in the Svensson and Green profiles. Among the models, Liu best matched the experimental extremes at both locations, while Svensson overestimated and Green underestimated

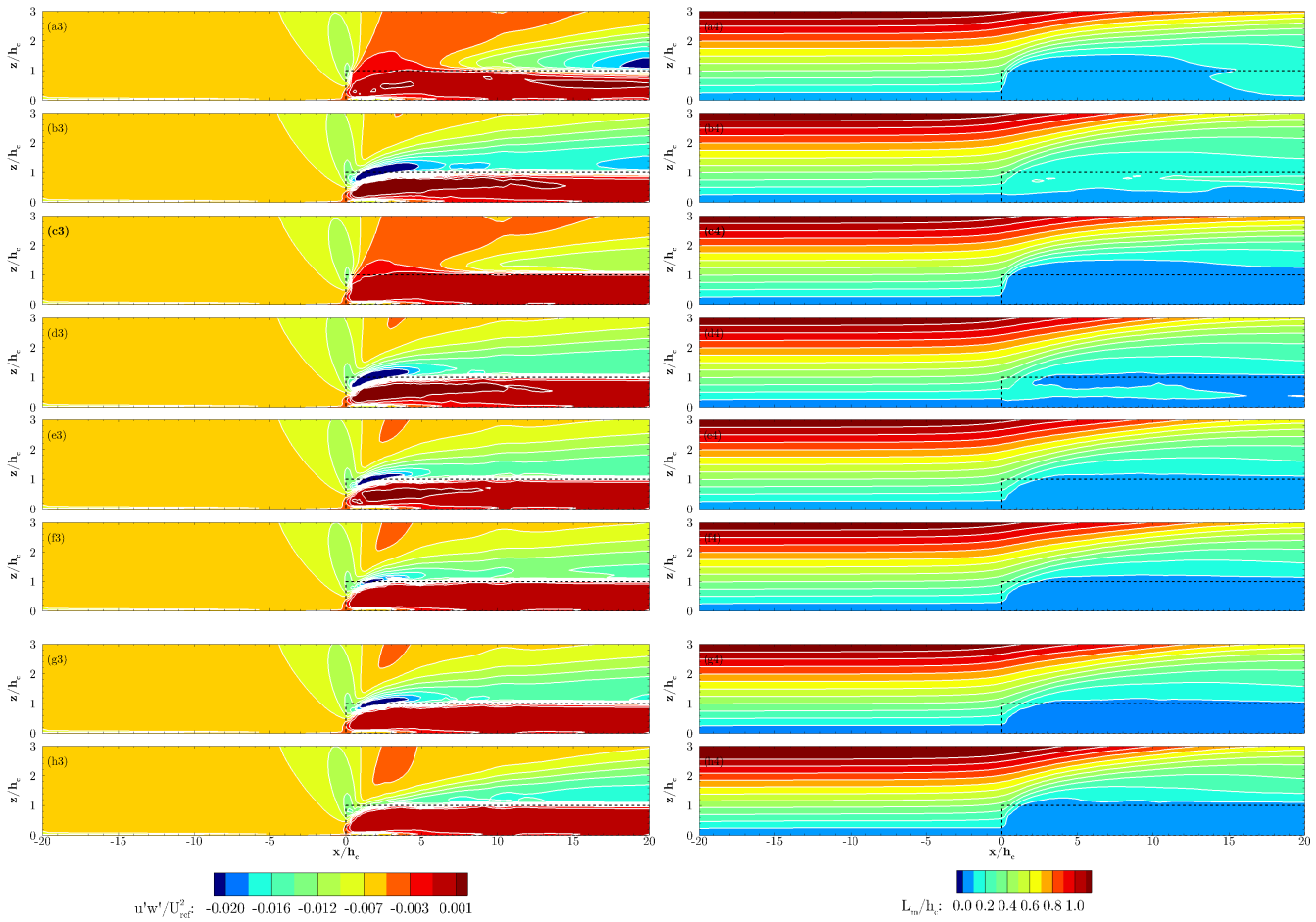


Figure 8. Scenario 1: Reynolds shear stress and mixing length scale ($L_m = C_\mu^{3/4}\ k^{3/2}\ \varepsilon^{-1}$) (a) Svensson, (b) Green, (c) Liu, (d) Sanz, (e) Costa, (f) Lopes, (g) Viana, (h) Sogachev .

them. All models showed similar TKE trends, except for Svensson and Green, which consistently overestimated TKE at both M2 and M1. The other models were closer to the measurements. For $\overline{u'w'}$ (Figures 9c and 10c), the models generally followed the measured pattern, although clear differences appeared. Svensson and Green predicted much higher shear stress, while Liu gave lower values. These differences reflect how each model handles eddy viscosity, which depends on turbulence production and dissipation. In this case, the higher TKE predicted by Svensson and Green led to increased eddy viscosity and, as a result, stronger shear stress. The other models followed a more consistent $\overline{u'w'}$ trend.

The RMSE and BIAS results (Table 4) indicate that the Sanz model gives the most accurate wind speed predictions, with the lowest RMSE at both M2 and M1. The Lopes model performs best for TKE, while Sanz also provides the most accurate Reynolds shear stress estimates at M2. At M1, however, the Green model performs better for shear stress. In contrast, the

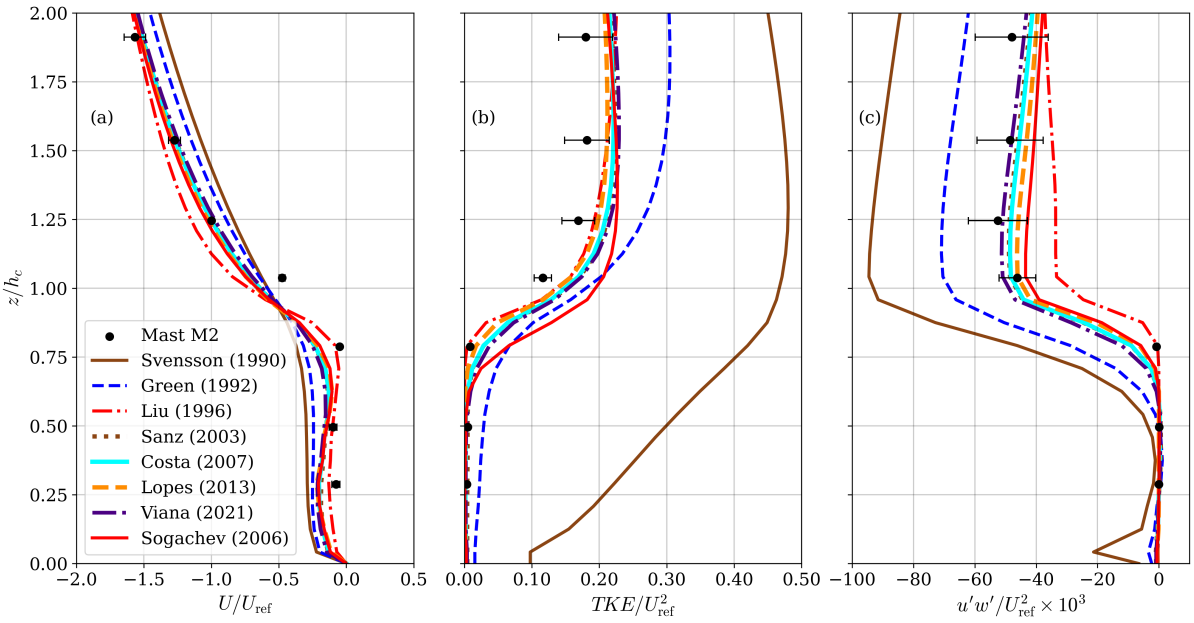


Figure 9. Measurements and computational results of flow from the forest at Mast M2: (a) streamwise velocity; (b) turbulent kinetic energy; (c) Reynolds shear stress. The black horizontal lines are the variability bars. The streamwise velocity was multiplied by -1 to represent flow from the forest and to enable a direct comparison with Scenario 1, where the flow is towards the forest. This sign change was applied only to the mean wind speed for visual and comparative consistency.

Svensson model consistently shows the highest RMSE and BIAS across all variables, indicating poor agreement with the observations.

The contour plot of the normalised streamwise velocity (U/U_{ref}, Figure 11) shows a deceleration of the flow within the canopy due to vegetation drag for all models. This leads to a low-speed zone near the ground, with the flow starting to recover above the canopy height ($z/h_c > 1$). Localised recirculation zones indicate increased turbulence and momentum exchange within the canopy, although the recirculation was modest and could not be confirmed. Wind jets were also observed within the canopy. These flow features are important for wind energy applications, as they affect turbine positioning and performance.

Above the canopy, a high-TKE layer extends from roughly $-20h_c$ to beyond $20h_c$ downwind (Figure 11), a feature typical of flow over forested terrain. This layer is relevant for wind turbine lifespan, as it influences the ideal distance from the forest edge for turbine placement and increases blade exposure to turbulence. Within the canopy, the flow is damped by vegetation-induced drag and turbulence dissipation—an effect that models like Svensson fail to capture. The positive momentum flux within the canopy and the well-defined internal boundary layer (IBL) above it (Figure 12) further illustrate the canopy's role in shaping the wind profile. Regarding the turbulence length scale (Figure 12), Liu, Costa, and Sogachev predicted a relatively

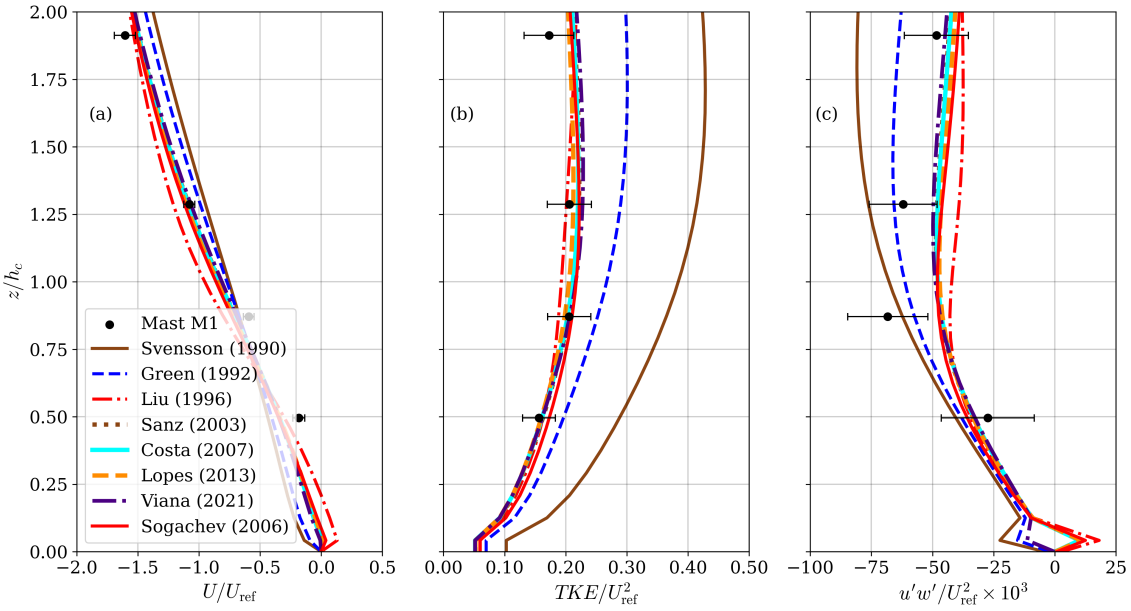


Figure 10. Measurements and computational results of flow from the forest at Mast M1: (a) streamwise velocity; (b) turbulent kinetic energy; (c) Reynolds shear stress. The black horizontal lines are the variability bars. The streamwise velocity was multiplied by -1 to represent flow from the forest and to enable a direct comparison with Scenario 1, where the flow is towards the forest. This sign change was applied only to the mean wind speed for visual and comparative consistency.

stable and lower L_m below the canopy. In contrast, other models, especially Svensson and Green, showed higher and more variable values, associated with their elevated TKE levels.

The performance of each model and its dependency on the focused variable depends on how it was developed. For instance, in the case of the Svensson model, the parameter $C_{\epsilon 4}$ was adjusted to achieve a good fit for the mean streamwise velocity and the Reynolds shear stress, as documented. The Liu model was derived by modifying the dissipative term S_{C_ε} in equation (9) to better capture the eddy viscosity while assuming a constant mixing length scale, as discussed in Liu (1996). The tuning of μ_t is crucial for the overall performance of the RANS k-ε turbulence model, as observed in the case of the Liu model. In Sogachev's approach the model's performance is more dependent on the settings of the atmospheric flow constants (C_μ, σ_k, σ_ε, $C_{\varepsilon 1}$, $C_{\varepsilon 2}$, κ) rather than introducing additional constants to the $k-\varepsilon$ model. In a specific case, the Sogachev (0.03, 1, 1.3, 1.21, 1.92, 0.4) yielded better predictions than Sogachev (0.09, 1, 1.7, 1.52, 1.833, 0.4), result not shown, as reported Ivanell et al. (2018), where $C_\mu = 0.03$ better represented TKE. The constants of the Lopes model were determined to maximise the correlation between RANS and LES canopy drag contributions to the TKE and dissipation rate (ε), resulting in excellent performance for TKE. However, it is worth noting that the Lopes model underestimates near the ground, as shown in Fig. 5, and this is a recognised limitation of the model, as reported in Lopes (2013). This underestimation can be related to the model's underestimation of the

Table 4. Flow from the forest: RMSE and Bias.

		Mast M2		Mast M1	
	Model	RMSE	Bias	RMSE	Bias
U/U_{ref}	Svensson (1990)	<u>0.217</u>	**0.041**	<u>0.203</u>	<u>-0.020</u>
	Green (1992)	0.170	0.049	0.166	**-0.001**
	Liu (1996)	0.152	<u>0.095</u>	0.141	0.096
	Sanz (2003)	**0.123**	0.072	**0.111**	0.039
	Costa (2007)	0.125	0.076	**0.111**	0.041
	Lopes (2013)	0.129	0.086	0.114	0.052
	Viana (2021)	0.127	0.070	0.114	0.031
	Sogachev (2006)	0.126	0.087	0.119	0.062
$\mathrm{TKE}/U_{\mathrm{ref}}^2$	Svensson (1990)	<u>0.313</u>	<u>0.308</u>	<u>0.194</u>	<u>0.188</u>
	Green (1992)	0.084	0.074	0.082	0.074
	Liu (1996)	0.027	**0.018**	0.024	**0.007**
	Sanz (2003)	0.034	0.028	0.023	0.016
	Costa (2007)	0.033	0.026	0.022	0.014
	Lopes (2013)	**0.025**	**0.018**	**0.017**	0.009
	Viana (2021)	0.038	0.031	0.026	0.019
	Sogachev (2006)	0.049	0.039	0.022	0.019
$\overline{u'w'}/U_{\mathrm{ref}}^2 \times 10^3$	Svensson (1990)	<u>36.148</u>	<u>-31.178</u>	<u>19.081</u>	<u>-13.397</u>
	Green (1992)	17.981	-14.817	**10.952**	**-4.675**
	Liu (1996)	10.978	8.192	18.250	13.038
	Sanz (2003)	**4.129**	**0.374**	13.471	8.710
	Costa (2007)	4.296	0.581	13.665	9.002
	Lopes (2013)	4.823	2.152	14.423	9.791
	Viana (2021)	4.768	-1.249	12.802	8.051
	Sogachev (2006)	6.303	3.606	14.455	9.287

Note: Best and worst values in bold and underlined.

turbulent transport term in the same region. Considering the fraction of turbulent kinetic energy dissipated by short-circuiting of the energy cascade (β_d) is essential in turbulence modelling. Models that account for this fraction tend to better replicate the behaviour of turbulent kinetic energy, as observed in Lopes (2013) and Viana (2021). Conversely, models that do not consider this fraction often struggle to reproduce the behaviour of turbulent kinetic energy.

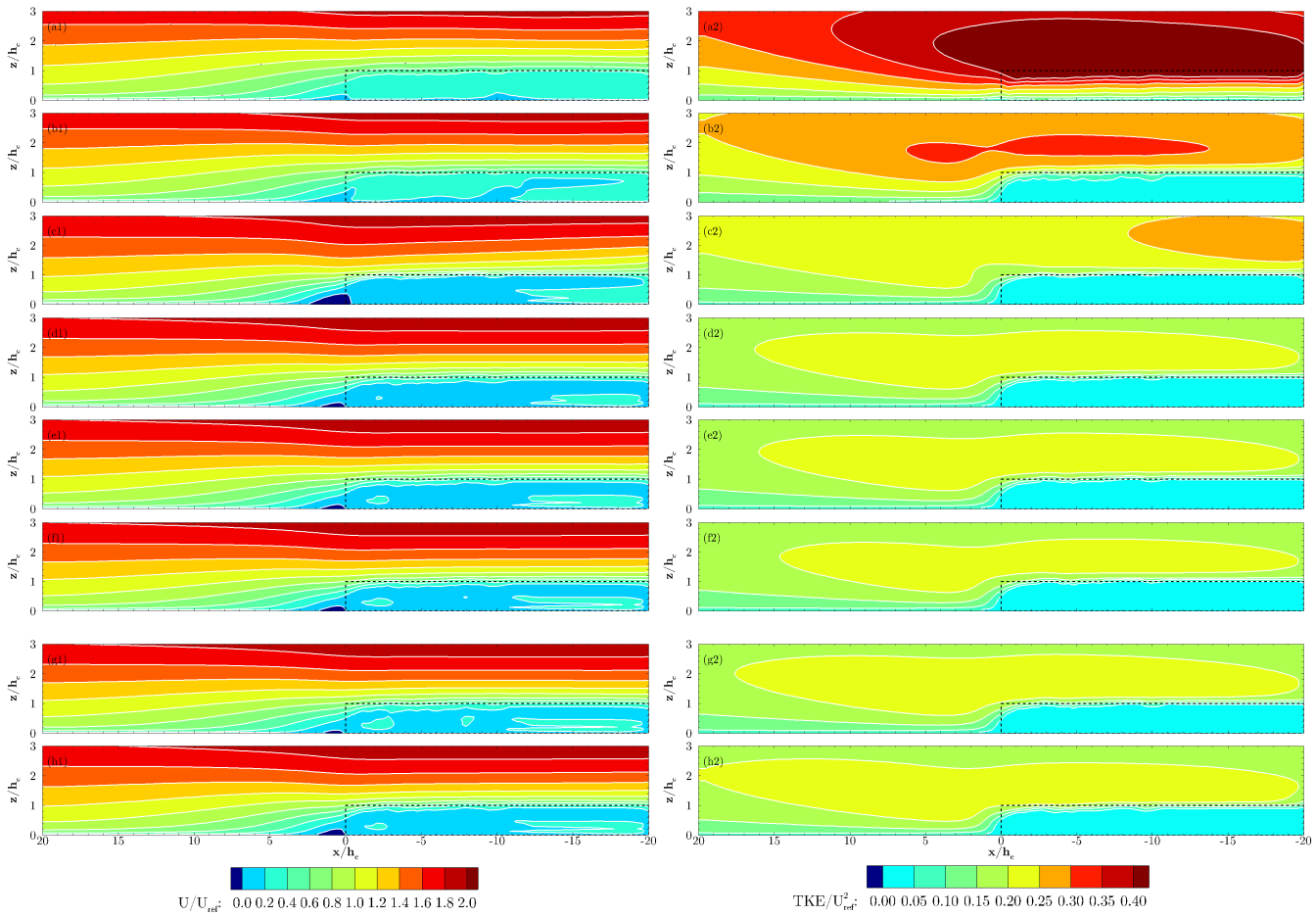


Figure 11. Scenario 2: mean streamwise velocity and turbulent kinetic energy (a) Svensson, (b) Green, (c) Liu, (d) Sanz, (e) Costa, (f) Lopes, (g) Viana, (h) Sogachev .

6 Conclusions

Eight canopy models were evaluated in neutrally stratified flow over flat terrain covered by a forest in an edge configuration. Additional terms represented the interaction between the forest and the atmosphere in the transport equations of TKE, its dissipation rate (k-ε), and a body force in the momentum equations. The simulations replicated the conditions observed in a site used for benchmarking. Results of the mean streamwise velocity, turbulent kinetic energy and Reynolds shear stress were used to assess the models' performance.

The model results of the flow towards the forest captured the five well-known features:

- Strong damping of wind and turbulence kinetic energy (TKE) inside the forest, except for Svensson and Häggkvist (1990), Green (1992) and Sanz (2003), which predicted high TKE;

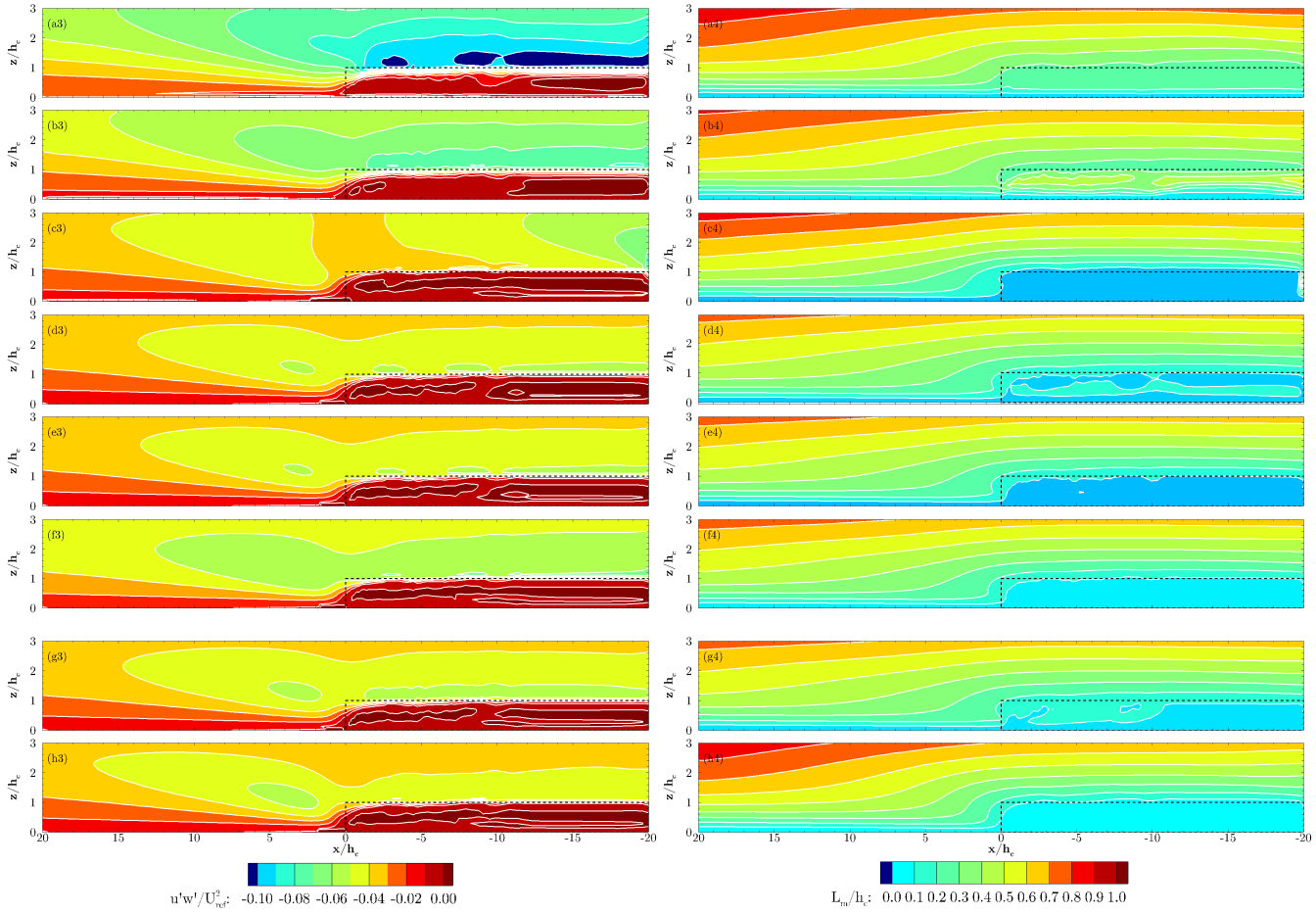


Figure 12. Scenario 2: Reynolds shear stress and mixing length scale ($L_m = C_\mu^{3/4} k^{3/2} \varepsilon^{-1}$) (a) Svensson, (b) Green, (c) Liu, (d) Sanz, (e) Costa, (f) Lopes, (g) Viana, (h) Sogachev .

- Wind jet at sub-canopy layer due to low canopy leaf density;
- Presence of a high TKE layer for Svensson, Green, Sanz and Sogachev and Panferov (2006) at the upper canopy due to large wind shear associated with the canopy leaf density concentration. Other models show a modest increase compared to the upstream (undisturbed) TKE near and inside the upper canopy.
- Early onset of the internal boundary layer (or mixing layer) above the forest at $1.04h_c$, which is similar to the observation data, except for Svensson and Liu et al. (1996) model;
- A positive momentum flux layer is observed within the canopy edge, along with a high negative momentum flux above the canopy in the internal boundary layer. However, it is important to emphasise that at the measurement position (one

and a half canopy heights from the edge), unlike most models, Svensson and Liu's models emphasised momentum flux at the canopy top, in line with observational data.

The model results of flow from the forest showed the following features:

- Wind speed damping and high wind jet below the canopy; above it, a pronounced recovery of the flow is observed.;
- A small flow separation zone at downwind edge;
- A high TKE layer above the canopy, extending up to $20h_c$ downstream, while within the forest, the canopy acts as a sink, damping TKE;
- A layer of positive momentum flux inside the canopy; above it, large downward momentum flux develops in regions with no well-defined internal boundary layer.

Based on the performance of the eight models, Liu gave the best predictions of mean streamwise velocity, TKE, and shear stress for flow towards the forest. In the reverse flow direction, the model by Lopes et al. (2013) performed better in capturing both the mean and turbulent characteristics. Overall, models that account only for the dissipation of TKE due to short-circuiting of the energy cascade offer a more accurate representation of TKE behavior. In contrast, some canopy closure models treat the forest as a TKE source, which contradicts observations. Except for the Svensson and Häggkvist (1990) and Green (1992) models, the remaining approaches are suitable for wind resource assessments over forested flat terrain, providing useful insights into the horizontal and vertical extent of the high-TKE layer.

Data availability. TEXT

The data used to validate the models are available at ???

Appendix A: A note on the approach by Sogachev and Panferov (2006)

The proposal by Sogachev and Panferov (2006) is formally different from all the others (changing the ε equation only)

Option 1: based on the ε equation only

Equating (9) and (10), there are greater similarities with Lopes et al. (2013) and Lopes et al. (2021) than with any of the remaining six.

$$\rho C_d\, a(x,z)\left(C_{\varepsilon 4}\beta_p|U|^3\frac{\varepsilon}{k}-C_{\varepsilon 5}\beta_d|U|\varepsilon\right)=\rho C_d\, a(x,z)\,|U|\,\beta\sqrt{C_\mu}\,(C_{\varepsilon 2}-C_{\varepsilon 1})\,k\,\frac{\varepsilon}{k} \tag{A1}$$

$$\left(\underbrace{\cancel{C_{\varepsilon 4}\beta_p|U|^3\frac{\varepsilon}{k}}}_{\beta_p=0}-C_{\varepsilon 5}\beta_d|U|\varepsilon\right)=|U|\,\beta\sqrt{C_\mu}\,(C_{\varepsilon 2}-C_{\varepsilon 1})\,\varepsilon \tag{A2}$$

$$-C_{\varepsilon 5}\beta_d=\beta\sqrt{C_\mu}\,(C_{\varepsilon 2}-C_{\varepsilon 1}) \tag{A3}$$

$$C_{\varepsilon 5}=-\left[\beta\sqrt{C_\mu}\,(C_{\varepsilon 2}-C_{\varepsilon 1})\right]/\beta_d \tag{A4}$$

$C_{\varepsilon 5}$ in Sogachev's formulation is equivalent to -0.37 and -0.55 in Lopes (2013) and Viana (2021).

Option 1: based on the k and ε equation also

Since turbulence is in equilibrium inside the canopy, $S_{C_k}=0$, and

$$\beta_p|U|^3\frac{\varepsilon}{k}-\beta_d|U|\varepsilon=0 \tag{A5}$$

$$\beta_p|U|^3=\beta_d|U|k \tag{A6}$$

which replaced in (9)

$$\left(C_{\varepsilon 4}\beta_d k|U|\frac{\varepsilon}{k}-C_{\varepsilon 5}\beta_d|U|\varepsilon\right)=|U|\,\beta\sqrt{C_\mu}\,(C_{\varepsilon 2}-C_{\varepsilon 1})\,\varepsilon \tag{A7}$$

$$(C_{\varepsilon 4}-C_{\varepsilon 5})\,\beta_d=\beta\sqrt{C_\mu}\,(C_{\varepsilon 2}-C_{\varepsilon 1}) \tag{A8}$$

$$C_{\varepsilon 4}-C_{\varepsilon 5}=\left[\beta\sqrt{C_\mu}\,(C_{\varepsilon 2}-C_{\varepsilon 1})\right]/\beta_d \tag{A9}$$

in Sogachev's formulation $C_{\varepsilon 4}-C_{\varepsilon 5}$ is equal to 0.37 and 0.55 in Lopes and Viana.

Author contributions. TEXT

this section is mandatory

Competing interests. TEXT

The authors declare that they have no conflict of interest.

Disclaimer. TEXT

Acknowledgements. TEXT

References

Arnqvist, J., Freier, J., and Dellwik, E.: Robust processing of airborne laser scans to plant area density profiles, Biogeosciences, 17, 5939–5952, https://doi.org/10.5194/bg-17-5939-2020, 2020.

Bechmann, A., Berg, J., Courtney, M., Ejsing Jørgensen, H., Mann, J., and Sørensen, N.: The Bolund Experiment: Overview and Background, no. 1658(EN) in Denmark. Forskningscenter Risoe. Risoe-R, Danmarks Tekniske Universitet, Risø Nationallaboratoriet for Bæredygtig Energi, ISBN 978-87-550-3703-8, risø-R-1658(EN), 2009.

Belcher, S. E., Jerram, N., and Hunt, J. C. R.: Adjustment of a turbulent boundary layer to a canopy of roughness elements, J. Fluid Mech., 488, 369–398, https://doi.org/10.1017/S0022112003005019, 2003.

Boudreault, L. E., Dupont, S., Bechmann, A., and Dellwik, E.: How forest inhomogeneities affect the edge flow, Bound.-Lay. Meteorol., 162, 375–400, https://doi.org/https://doi.org/10.1007/s10546-016-0202-5, 2017.

Castro, F. A., Palma, J. M. L. M., and Lopes, A. S.: Simulation of the Askervein flow. Part 1: Reynolds averaged Navier-Stokes equations ($k-\epsilon$ turbulence model), Bound.-Lay. Meteorol., 107, 501–530, https://doi.org/https://doi.org/10.1023/A:1022818327584, 2003.

Costa, J. C. L., Castro, F. A., Palma, J. M. L. M., and Stuart, P.: Computer simulation of atmospheric flows over real forests for wind energy resource evaluation, J. Wind Eng. Ind. Aerodyn., 94, 603–620, https://doi.org/10.1016/j.jweia.2006.02.002, 2006.

Costa, J. C. P. L.: Atmospheric flow over forested and non-forested complex terrain, Ph.D. thesis, University of Porto, 2007.

Dellwik, E., Bingöl, F., and Mann, J.: Flow distortion at a dense forest edge, Q. J. R. Meteorol. Soc., 140, 676–686, https://doi.org/10.1002/qj.2155, 2014.

Dellwik, E., van der Laan, M. P., Angelou, N., Mann, J., and Sogachev, A.: Observed and modeled near-wake flow behind a solitary tree, Agric. For. Meteorol., 265, 78–87, https://doi.org/10.1016/j.agrformet.2018.10.015, 2019.

Dellwik, E., Romanic, D., Mann, J., Enuş, M., and Hangan, H.: Forest Edge Representation in Scaled Experiments: A Flexible Approach for Matching to Field Observations, Boundary-Layer Meteorology, 187, 793–817, https://doi.org/10.1007/s10546-023-00796-z, 2023.

Detto, M., Katul, G. G., Siqueira, M., Juang, J., and Stoy, P.: The structure of turbulence near a tall forest edge: the backward-facing step flow analogy revisited, Ecol. Appl., 18, 1420–1435, https://doi.org/10.1890/06-0920.1, 2008.

Dupont, S., Bonnefond, J. M., Irvine, M. R., Lamaud, E., and Brunet, Y.: Long-distance edge effects in a pine forest with a deep and sparse trunk space: In situ and numerical experiments, Agric. For. Meteorol., 151, 328–344, 2011.

Enevoldsen, P.: Onshore wind energy in northern european forests: reviewing the risks, Renew. Sust. Energ. Rev., 60, 1251–1262, 2016.

Finnigan, J.: Turbulence in plant canopies, Annual Review of Fluid Mechanics, 32, 519–571, https://doi.org/10.1146/annurev.fluid.32.1.519, 2000.

Green, S. R.: Modelling turbulent air flow in a stand of widely-spaced trees, PHOENICS J. Comput. Fluid Dyn. its Appl., 5, 294–312, 1992.

Ivanell, S., Arnqvist, J., Avila, M., Cavar, D., Aurelio Chavez-Arroyo, R., Olivares-Espinosa, H., Peralta, C., Adib, J., and Witha, B.: Micro-scale model comparison (benchmark) at the moderately complex forested site Ryningsnäs, Wind Energy Sci., 3, 929–946, https://doi.org/10.5194/WES-3-929-2018, 2018.

Liu, H., Peters, G., and Foken, T.: New Equations for Sonic Temperature Variance and Buoyancy Heat Flux with an N Omnidirectional Sonic Anemometer, Boundary Layer Meteorology, https://doi.org/https://doi.org/10.1023/A:1019207031397, 2001.

Liu, J., Chen, J. M., Black, T. A., and Novak, M. D.: E-ϵ modelling of turbulent air flow downwind of a model forest edge, Bound.-Lay. Meteorol., 77, 2–44, 1996.

Lopes, A. S., Palma, J. M. L. M., and Lopes, J. V.: Improving a two-equation turbulence model for canopy flows using large-eddy simulation, Bound.-Lay. Meteorol., 149, 231–257, 2013.

Lopes, J. M. V. P., Palma, J. M. L. M., and Lopes, A. S.: Modelling the flow within forests: the canopy-related terms in the Reynolds-averaged formulation, J. Fluid Mech., 910, 7–24, https://doi.org/10.1017/jfm.2020.927, 2021.

Mann, J. and Dellwik, E.: Sudden distortion of turbulence at a forest edge, Journal of Physics: Conference Series, 524, 012 103, http://iopscience.iop.org/1742-6596/524/1/012103, 2014.

Monteiro, J. R., Batista, V. T. P., and Palma, J. M. L. M.: Assessing canopy models across forest edges on flat terrain, Journal of Physics: Conference Series, 2767, 092 011, https://doi.org/10.1088/1742-6596/2767/9/092011, 2024.

Raupach, M. R., Bradley, E. F., and Ghadiri, H.: Wind tunnel investigation into the aerodynamic effect of forest clearing of the nesting of Abbott's Booby on Christmas Island, Progress report, CSIRO Division of Environmental Mechanics, Canberra, Australia, 1987.

Richards, P. J. and Norris, S. E.: Appropriate boundary conditions for computational wind engineering models revisited , J. Wind Eng. Ind. Aerodyn., 99, 257–266, 2011.

Sanz, C.: A note on $k-\varepsilon$ modelling of vegetation canopy air-flows, Bound.-Lay. Meteorol., 108, 191–197, https://doi.org/10.1023/A:1023066012766, 2003.

Sogachev, A.: A note on two-equation closure modelling of canopy flow, Bound.-Lay. Meteorol., 130, 423–435, https://doi.org/10.1007/s10546-008-9346-2, 2009.

Sogachev, A. and Panferov, O.: Modification of two-equation models to account for plant drag, Bound.-Lay. Meteorol., 121, 229–266, https://doi.org/10.1007/s10546-006-9073-5, 2006.

Sogachev, A., Kelly, M., and Leclerc, M. Y.: Consistent two-equation closure modelling for atmospheric research: buoyancy and vegetation implementations, Bound.-Lay. Meteorol., 145, 307–327, https://doi.org/10.1007/s10546-012-9726-5, 2012.

Svensson, U. and Häggkvist, K.: A two-equation turbulence model for canopy flows, J. Wind Eng. Ind. Aerodyn., 35, 201–211, 1990.

Yang, B., Raupach, M. R., Shaw, R. H., Tha Paw U, K., and Morse, A. P.: Large-eddy simulation of turbulent flow across a forest edge. Part I: flow statistics, Bound.-Lay. Meteorol., 120, 377–412, https://doi.org/10.1007/s10546-006-9057-5, 2006.

D.3 Paper III-Abstract: Modelling the flow within forest: The weak turbulence regime approach in the Reynolds-averaged formulation with $k - \varepsilon$ turbulence model.

The weak turbulence regime (WTR) canopy model was developed in a steady RANS $k - \varepsilon$ framework to better capture canopy-driven turbulence in different flow conditions. It uses perturbation theory, assuming TKE is small compared to the mean flow's kinetic energy. Unlike earlier simplified versions (Lopes et al., 2016), it solves the full dissipation equation, keeping it consistent with the turbulence scheme.

Simulations were carried out for three canonical canopy configurations of increasing complexity: a horizontally homogeneous forest, a forest edge, and a forested hill. Large-eddy simulation (LES) data from Lopes (2013) served as reference, and results were benchmarked against the canopy models of Liu (1996) and Lopes (2013). All simulations used the same drag formulation and numerical setup to isolate the impact of turbulence modelling. Wind speed was normalised by the reference velocity (U_b), while TKE, Reynolds shear stress, and dissipation were scaled by the friction velocity at canopy top (u_*). RMSE and BIAS were used to assess model performance.

In the homogeneous case, the WTR model produced accurate wind speed and turbulence predictions, with RMSE and BIAS values comparable and better than the Lopes model, despite not being tuned for this configuration. It captured the shape and magnitude of the TKE profile more reliably than Liu or Lopes, demonstrating improvements over earlier implementations (Lopes et al., 2016). For the forest edge case, the WTR model delivered the most balanced performance. It closely matched LES results for velocity and shear stress and showed a reasonable estimate of TKE and dissipation. Contour plots revealed that WTR minimised local over- or under-predictions near the canopy top and downstream of the edge. Although the Lopes model performed slightly better for peak TKE values, it consistently overpredicted other variables, while Liu showed weaker agreement across all metrics. In the forested hill scenario, WTR again performed best overall. It successfully reproduced the speed-up on the windward slope and the recirculation in the lee, unlike the Lopes model, which failed to capture flow separation. WTR showed the lowest errors across all evaluated quantities, highlighting its robustness under complex terrain conditions.

Overall, the WTR model performed well without case-specific tuning. While calibrating canopy coefficients, as in Lopes et al. (2013), can improve accuracy, it limits use at other sites. WTR offers a more general approach.

New WTR simulations are under way to study grid-sensitivity effects. Starting from the mesh in Lopes et al. (2021), the node count is doubled and the grid spacing halved for both forest-edge and forested-hill cases. LES data from Lopes et al. (2021) will serve as the reference. At the same time, budget analyses of momentum, TKE, and dissipation are being prepared to highlight the physical differences between the WTR scheme and reference canopy models like Lopes et al. (2013).

D.4 Paper IV-Abstract: Three-dimensional formulation of the weak turbulence regime in Reynolds-averaged framework with $k - \varepsilon$ turbulence model: the Perdigão case study.

Predicting atmospheric flow over complex terrain is challenging, and forests add complexity. CFD accuracy depends on canopy parametrisation. This study tests the Weak Turbulence Regime (WTR) model at Perdigão site, whose steep terrain, complex forests, and 2017 field data make it ideal for evaluating canopy models.

The simulations were performed using the VENTOS®/2 CFD solver, with the WTR approach implemented within a standard RANS framework. Forest effects were modelled using detailed canopy input data from a 2015 airborne LIDAR survey (ALS), which provided high-resolution information on leaf area density (LAD) and tree height. Unlike previous studies that used simplified or uniform vegetation profiles, this work accounts for spatial variability in the canopy, allowing the model to capture small-scale features such as gaps and forest edges more accurately. The focus was on near-neutral atmospheric conditions under southwesterly (SW) and northeasterly (NE) winds, identified using the Obukhov length derived from 10 m tower measurements. To assess model performance, additional simulations were run without canopy parametrisation, alongside two known RANS-based canopy models—the Liu and Lopes models—for comparison. Observational data from 14 meteorological towers were used for validation, including three 20 m towers (tnw01/T01, tnw02/T02, tnw11/T11), seven 30 m towers (tse01/T12 to tse02/T18), one 60 m tower (rsw03/T34), and three 100 m towers (tse04/T20, tse09/T25, tse13/T29). All towers were equipped with 20 Hz anemometers, providing high-frequency wind measurements for benchmarking the simulation results.

The results show that the WTR approach performs much like the Liu and Lopes models in predicting mean flow and turbulence patterns. Cross-sections and vertical profiles reveal that it captures key features, including slower flow on windward slopes, higher turbulence above the canopy, and recirculation zones on the leeward side. These match well with measurements from several tower locations. Liu tends to predict lower turbulence, Lopes higher, and WTR produces intermediate TKE near forested slopes. Overall, the WTR approach works well in complex terrain, balancing mean and turbulent flow representation without relying on the fixed constants used in models like Liu or Lopes.

Overall, this study highlights the advantages of combining realistic forest representation with advanced canopy parametrisations when modelling flow over complex terrain. The WTR approach showed good predictive skill across various conditions and appears well suited for future applications in wind energy and micrometeorology.

Ongoing work involves simulations that use a more detailed and spatially variable surface roughness map—such as the CORINE Land Cover dataset—combined with tree height data from Sentinel-2 and the 2015 ALS survey. The recirculation zone in the simulations is being validated using LIDAR data. These enhancements aim to improve the realism of canopy representation and extend the effective forest coverage in the model. As a result, the physical accuracy of canopy modelling is expected to improve, leading to more reliable predictions of atmospheric flow over forested terrain.

Bibliography

P. C. Albornoz, A. M. Soberanis, R. V. Rivera, and M. Rivero. Review of atmospheric stability estimations for wind power applications. *Renewable and Sustainable Energy Reviews*, 163: 112505, 2022. ISSN 1364-0321. doi: https://doi.org/10.1016/j.rser.2022.112505. URL `https://www.sciencedirect.com/science/article/pii/S1364032122004099`.

J. Arnqvist, J. Freier, and E. Dellwik. Robust processing of airborne laser scans to plant area density profiles. *Biogeosciences*, 17:5939–5952, 2020. ISSN 17264189. doi: 10.5194/BG-17-5939-2020.

R. C. Arroy, J. S. Rodrigo, and P. Gankarski. Modelling of atmospheric boundary-layer flow in complex terrain with different forest parameterizations. *Journal of Physics: Conference Series*, 524:012119, 2014. doi: 10.1088/1742-6596/524/1/012119.

E. J. Bannister, A. R. MacKenzie, and X.-M. Cai. Realistic forests and the modeling of forest-atmosphere exchange. *Reviews of Geophysics*, 60(1):e2021RG000746, 2022. doi: https://doi.org/10.1029/2021RG000746. URL `https://agupubs.onlinelibrary.wiley.com/doi/abs/10.1029/2021RG000746`. e2021RG000746 2021RG000746.

V. T. P. Batista and J. M. L. M. Palma. Perdigão terrain coverage: forest size and distribution and main aerodynamic parameters. Technical report, University of Porto, 2021.

S. E. Belcher, N. Jerram, and J. C. R. Hunt. Adjustment of a turbulent boundary layer to a canopy of roughness elements. *Journal of Fluid Mechanics.*, 488:369–398, 2003. doi: 10.1017/S0022112003005019.

S. E. Belcher, I. N. Harman, and J. Finnigan. The wind in the willows: flows in forest canopies in complex terrain. *Annual Review of Fluid Mechanics*, 44:479–504, 2012. doi: 10.1146/ANNUREV-FLUID-120710-101036.

L. É. Boudreault, S. Dupont, A. Bechmann, and E. Dellwik. How forest inhomogeneities affect the edge flow. *Boundary-Layer Meteorology*, 162(3):375–400, 2017. doi: https://doi.org/10.1007/s10546-016-0202-5.

Y. Brunet. Turbulent flow in plant canopies: historical perspective and overview. *Boundary-Layer Meteorology*, 177:315–364, 2020. doi: 10.1007/s10546-020-00560-7.

F. A. Castro, J. M. L. M. Palma, and A. S. Lopes. Simulation of the Askervein flow. Part 1: Reynolds averaged Navier-Stokes equations ($k - \epsilon$ turbulence model). *Boundary-Layer Meteorology*, 107(3):501–530, 2003. doi: https://doi.org/10.1023/A:1022818327584.

C. Cintolesi, F. Barbano, P. L. Trudu, A. Finco, G. Gerosa, and S. Di Sabatino. Characterisation of flow dynamics within and around an isolated forest, through measurements and numerical simulations. *Agricultural and Forest Meteorology*, 343:109287, 2023. ISSN 0168-1923. doi: 10.1016/j.agrformet.2023.109287. URL `https://doi.org/10.1016/j.agrformet.2023.109287`.

A. Clifton, S. Barber, A. Stökl, H. Frank, and T. Karlsson. Research challenges and needs for the deployment of wind energy in hilly and mountainous regions. *Wind Energy Science*, 7 (6):2231–2254, 2022. doi: 10.5194/wes-7-2231-2022. URL `https://wes.copernicus.org/articles/7/2231/2022/`.

I. Coimbra, J. Mann, and J. M. L. M Palma. Exploring dual-lidar mean and turbulence measurements over complex terrain. *Atmospheric Measurement Techniques*, 2024:1–26, 2024. doi: 10.5194/egusphere-2024-936. URL `https://egusphere.copernicus.org/preprints/2024/egusphere-2024-936/`.

J. C. P. L. Costa. *Atmospheric flow over forested and non-forested complex terrain*. PhD thesis, University of Porto, 2007.

J. C. P. L. Costa, F. A. Castro, J. M. L. M. Palma, and P. Stuart. Computer simulation of atmospheric flows over real forests for wind energy resource evaluation. *Journal of Wind Engineering and Industrial Aerodynamics*, 94(8):603–620, 2006. ISSN 01676105. doi: 10.1016/j.jweia.2006.02.002.

E. Dellwik, F. Bingöl, and J. Mann. Flow distortion at a dense forest edge. *Quarterly Journal of the Royal Meteorological Society*, 140(679):676–686, 2014. doi: 10.1002/qj.2155.

E. Dellwik, M. P. van der Laan, N. Angelou, J. Mann, and A. Sogachev. Observed and modeled near-wake flow behind a solitary tree. *Agricultural and Forest Meteorology*, 265:78–87, 2019. ISSN 0168-1923. doi: 10.1016/j.agrformet.2018.10.015.

S. Dupont and Y. Brunet. Edge flow and canopy structure: a large-eddy simulation study. *Boundary-Layer Meteorology*, 126:51–71, 2008. doi: 10.1007/s10546-007-9216-3.

S. Dupont, Y. Brunet, and J. Finnigan. Large-eddy simulation of turbulent flow over a forested hill: validation and coherent structure identification. *Quarterly Jounal of the Royal Meteorological Society*, 134:1911–1929, 2008. doi: 10.1002/qj.328. URL `www.interscience.wiley.com`.

S. Dupont, J. M. Bonnefond, M. R. Irvine, E. Lamaud, and Y. Brunet. Long-distance edge effects in a pine forest with a deep and sparse trunk space: in situ and numerical experiments. *Agricultural and Forest Meteorology*, 151(3):328–344, 2011. doi: 10.1016/j.agrformet.2010.11.007.

H. J. S. Fernando, J. Mann, J. M. L. M. Palma, J. K. Lundquist, R. J. Barthelmie, M. Belo-Pereira, W. O. J. Brown, F. K. Chow, T. Gerz, C. M. Hocut, P. M. Klein, L. S. Leo, J. C. Matos, S. P. Oncley, S. C. Pryor, L. Bariteau, T. M. Bell, N. Bodini, M. B. Carney, M. S. Courtney, E. D. Creegan, R. Dimitrova, S. Gomes, M. Hagen, J. O. Hyde, S. Kigle, R. Krishnamurthy, J. C. Lopes, L. Mazzaro, J. M. T. Neher, R. Menke, P. Murphy, L. Oswald, S. Otarola-Bustos, A. K. Pattantyus, C. V. Rodrigues, A. Schady, N. Sirin, S. Spuler, E. Svensson, J. Tomaszewski, D. D. Turner, L. van Veen, N. Vasiljević, D. Vassallo, S. Voss, N. Wildmann, and Y. Wang. The Perdigão: peering into microscale details of mountain winds. *Bulletin of the American Meteorological Society*, 100(5):799–819, 2019. ISSN 0003-0007. doi: 10.1175/BAMS-D-17-0227.1.

J. H. Ferziger and M. Peric. *Computational methods for fluid dynamics*. Springer, 3 edition, 2002. ISBN 978-3-642-56026-2. doi: https://doi.org/10.1007/978-3-642-56026-2.

J. Finnigan. Turbulence in plant canopies. *Annual Review of Fluid Mechanics*, 32(1):519–571, 2000. doi: 10.1146/annurev.fluid.32.1.519.

J. Finnigan and S. E. Belcher. Flow over a hill covered with a plant canopy. *Quarterly Journal of the Royal Meteorological Society*, 130:1–29, 2004. ISSN 00359009. doi: 10.1256/qj.02.177.

J. Finnigan and R. H. Shaw. Double-averaging methodology and its application to turbulent flow in and above vegetation canopies. *Acta Geophysica*, 56(3):534–561, 2008. doi: 10.2478/s11600-008-0034-x. URL https://doi.org/10.2478/s11600-008-0034-x.

J. Finnigan, R. H. Shaw, and E. G. Patton. Turbulence structure above a vegetation canopy. *Journal of Fluid Mechanics*, 637:387–424, 2009. doi: 10.1017/S0022112009990589.

J. Finnigan, K. Ayotte, I. Harman, G. Katul, H. Oldroyd, E. Patton, D. Poggi, A. Ross, and P. Taylor. Boundary-layer flow over complex topography. *Boundary-Layer Meteorology*, 177:247–313, 2020. doi: 10.1007/s10546-020-00564-3. URL https://doi.org/10.1007/s10546-020-00564-3.

S. R. Green. Modelling turbulent air flow in a stand of widely-spaced trees. *PHOENICS Journal Computational Fluid Dynamics and its Applications*, 5:294–312, 1992.

K. Hanjalic and B. E. Launder. Contribution towards a Reynolds-stress closure for low-Reynolds-number turbulence. *Journal of Fluid Mechanics*, 74(4):593–610, 1976.

I. N. Harman and J. Finnigan. A simple unified theory for flow in the canopy and roughness sublayer. *Boundary-Layer Meteorology*, 123(2):339–363, 2007. doi: 10.1007/s10546-006-9145-6. URL https://doi.org/10.1007/s10546-006-9145-6.

J. C. R. Hunt, S. Leibovich, and K. J. Richards. Turbulent shear flows over low hills. *Quarterly Journal of the Royal Meteorological Society*, 114(484):1435–1470, 1988. doi: 10.1002/qj.49711448405.

IEA. World Energy Investment 2022, 2022. URL www.iea.org/t{&}c/.

S. Ivanell, J. Arnqvist, M. Avila, D. Cavar, R. Aurelio Chavez-Arroyo, H. Olivares-Espinosa, C. Peralta, J. Adib, and B. Witha. Micro-scale model comparison (benchmark) at the moderately complex forested site Ryningsnäs. *Wind Energy Science*, 3(2):929–946, 2018. ISSN 23667451. doi: 10.5194/WES-3-929-2018.

B. Launder. Application of the energy-dissipation model of turbulence to the calculation of flow near a spinning disc. *International Communications in Heat and Mass Transfer*, 1(2):131–137, 1974. doi: 10.1016/0735-1933(74)90024-4.

B. P. Leonard. A stable and accurate convective modelling procedure based on quadratic upstream interpolation. *Computer Methods in Applied Mechanics and Engineering*, 19(1):59–98, 1979. ISSN 0045-7825. doi: 10.1016/0045-7825(79)90034-3.

R. Li, Y. Zhao, M. Chang, F. Zeng, Y. Wu, L. Wang, J. Niu, X. Shi, and N. Gao. Numerical simulation methods of tree effects on microclimate: a review. *Renewable and Sustainable Energy Reviews*, 205:114852, 2024. ISSN 1364-0321. doi: https://doi.org/10.1016/j.rser.2024.114852. URL https://www.sciencedirect.com/science/article/pii/S1364032124005781.

F. Lien, E. Yee, and J. D. Wilson. Numerical modelling of the turbulent flow developing within and over a 3-D building array, part II: a mathematical foundation for a distributed drag force approach. *Boundary-Layer Meteorology*, 114:245–285, 2005.

J. Liu, J. M. Chen, T. A. Black, and M. D. Novak. E-ϵ modelling of turbulent air flow downwind of a model forest edge. *Boundary-Layer Meteorology*, 77:2–44, 1996.

A. S. Lopes, J. M. L. M. Palma, and J. M. V. P. Lopes. Improving a two-equation turbulence model for canopy flows using large-eddy simulation. *Boundary-Layer Meteorology*, 149(2): 231–257, 2013. doi: 10.1007/s10546-013-9850-x.

A. S. Lopes, J. M. L. M. Palma, and J. V. Lopes. Modelling flows within forested areas using the $k-\varepsilon$ rans model. *Journal of Physics: Conference Series*, 753(8):082035, 2016. doi: 10.1088/1742-6596/753/8/082035. URL `https://dx.doi.org/10.1088/1742-6596/753/8/082035`.

J. M. V. P. Lopes, J. M. L. M. Palma, and A. S. Lopes. Modelling the flow within forests: the canopy-related terms in the Reynolds-averaged formulation. *Journal of Fluid Mechanics*, 910:7, 2021. doi: 10.1017/jfm.2020.927.

V. G. M. Garza, J. Sumner, J. Nathan, and C. Masson. Evaluating the accuracy of rans wind flow modeling over forested terrain—part 1: canopy model validation. *Journal of Solar Energy Engineering*, 141(4):041009, 2019. doi: 10.1115/1.4042242. URL `https://doi.org/10.1115/1.4042242`.

Y. Ma, H. Liu, T. Banerjee, G. G. Katul, C. Yi, and E. R. Pardyjak. The effects of canopy morphology on flow over a two-dimensional isolated ridge. *Journal of Geophysical Research: Atmospheres*, 125(19):e2020JD033027, 2020. doi: https://doi.org/10.1029/2020JD033027. URL `https://agupubs.onlinelibrary.wiley.com/doi/abs/10.1029/2020JD033027`. e2020JD033027 2020JD033027.

R. Menke, N. Vasiljevi, J. Mann, and J. K. Lundquist. Characterization of flow recirculation zones at the Perdigão site using multi-lidar measurements. *Atmospheric Chemistry and Physics*, 19(4):2713–2723, 2019. ISSN 16807324. doi: 10.5194/ACP-19-2713-2019.

J. R. Monteiro, V. T. P. Batista, and J. M. L. M. Palma. Assessing canopy models across forest edges on flat terrain. *Journal of Physics: Conference Series*, 2767(9):092011, jun 2024. doi: 10.1088/1742-6596/2767/9/092011. URL `https://dx.doi.org/10.1088/1742-6596/2767/9/092011`.

J. M. L. M. Palma, C. A. M. Silva, V. M. M. G. C. Gomes, A. S. Lopes, T. Simões, P. Costa, and V. T.P. Batista. The digital terrain model in the computational modelling of the flow over the Perdigão site: the appropriate grid size. *Wind Energy Science*, 5(4):1469–1485, 2020. doi: 10.5194/WES-5-1469-2020.

S. V. Patankar. *Numerical heat transfer and fluid flow*. CRC Press, 1980. ISBN 9781315275130. doi: 10.1201/9781482234213.

E. G. Patton and G. G. Katul. Turbulent pressure and velocity perturbations induced by gentle hills covered with sparse and dense canopies. *Boundary-Layer Meteorology*, 133:189–217, 2009. doi: 10.1007/s10546-009-9427-x.

D. Poggi, A. Porporato, L. Ridolfi, J. D. Albertson, and G. G. Katul. The effect of vegetation density on canopy sub-layer turbulence. *Boundary-Layer Meteorology*, 111(3):565–587, 2004. doi: 10.1023/B:BOUN.0000016576.05621.73. URL https://doi.org/10.1023/B:BOUN.0000016576.05621.73.

J. Quimbayo-Duarte, J. Wagner, N. Wildmann, T. Gerz, and J. Schmidli. Evaluation of a forest parameterization to improve boundary layer flow simulations over complex terrain. A case study using WRF-LES V4.0.1. *Geoscientific Model Development*, 15(13):5195–5209, 2022. ISSN 1991-9603. doi: 10.5194/GMD-15-5195-2022. URL https://gmd.copernicus.org/articles/15/5195/2022/.

C. M. Rhie and W. L. Chow. Numerical study of the turbulent flow past an airfoil with trailing edge separation. *AIAA*, 21(11):1525–1532, 1983. ISSN 00011452. doi: 10.2514/3.8284. URL https://arc.aiaa.org/doi/abs/10.2514/3.8284.

P.J. Richards and S.E. Norris. Appropriate boundary conditions for computational wind engineering models revisited | Elsevier Enhanced Reader. *Journal of Wind Engineering and Industrial Aerodynamics*, 99:257–266, 2011.

C. V. Rodrigues. *Computer Modelling of Atmospheric Flows in Wind Energy Applications*. PhD thesis, University of Porto, 2013.

C. V. Rodrigues, J. M. L. M. Palma, and H. Á. Rodrigues. Atmospheric flow over a mountainous region by a one-way coupled approach based on Reynolds-averaged turbulence modelling. *Boundary-Layer Meteorology*, 159(2):407–437, 2016. doi: 10.1007/S10546-015-0116-7.

C. Sanz. A note on $k-\varepsilon$ modelling of vegetation canopy air-flows. *Boundary-Layer Meteorology*, 108(1):191–197, 2003. doi: 10.1023/A:1023066012766.

R. H. Shaw and U. Schumann. Large-eddy simulation of turbulent flow above and within a forest. *Boundary-Layer Meteorology*, 61:47–64, 1992. URL https://api.semanticscholar.org/CorpusID:56050838.

A. Sogachev. A note on two-equation closure modelling of canopy flow. *Boundary-Layer Meteorology*, 130:423–435, 2009. doi: 10.1007/s10546-008-9346-2.

A. Sogachev and O. Panferov. Modification of two-equation models to account for plant drag. *Boundary-Layer Meteorology*, 121:229–266, 2006. doi: 10.1007/s10546-006-9073-5.

A. Sogachev, M. Kelly, and M. Y. Leclerc. Consistent two-equation closure modelling for atmospheric research: buoyancy and vegetation implementations. *Boundary-Layer Meteorology*, 145:307–327, 2012. doi: 10.1007/s10546-012-9726-5.

D. B. Spalding. A novel finite difference formulation for differential expressions involving both first and second derivatives. *International Journal for Numerical Methods in Engineering*, 4 (4):551–559, 1972. ISSN 1097-0207. doi: 10.1002/NME.1620040409.

U. Svensson and K. Häggkvist. A two-equation turbulence model for canopy flows. *Journal of Wind Engineering and Industrial Aerodynamics*, 35(C):201–211, 1990. ISSN 01676105. doi: 10.1016/0167-6105(90)90216-Y.

D. Tabas, J. Fang, and F. Porté-Agel. Wind energy prediction in highly complex terrain by computational fluid dynamics. *Energies*, 12(7):1311, 2019. doi: 10.3390/en12071311.

J. Tolladay and C. Chemel. Numerical modelling of neutral boundary-layer flow across a forested ridge. *Boundary-Layer Meteorology*, 180:457–476, 2021. doi: 10.1007/s10546-021-00628-y. URL `https://doi.org/10.1007/s10546-021-00628-y`.

N. Vasiljevia, J. M. L. M. Palma, N. Angelou, J. C. Matos, R. Menke, G. Lea, J. Mann, M. Courtney, L. Frölen Ribeiro, and V. M. M. G. C. Gomes. Perdigaõ 2015: Methodology for atmospheric multi-doppler lidar experiments. *Atmospheric Measurement Techniques*, 10 (9):3463–3483, sep 2017. ISSN 18678548. doi: 10.5194/AMT-10-3463-2017.

K. Venkatraman, T. Hågbo, S. Buckingham, and K. E. T. Giljarhus. Effect of different source terms and inflow direction in atmospheric boundary modeling over the complex terrain site of perdigão. *Wind Energy Science*, 8(1):85–108, 2023. doi: 10.5194/wes-8-85-2023.

J. M. A. Vilaça. Analysis of atmospheric conditions: data quality and stationarity in perdigão. Master's thesis, Universidade do Porto, Faculdade de Engenharia, 2018.

S. Wharton and K. J. Lundquist. Assessing atmospheric stability and its impacts on rotor-disk wind characteristics at an onshore wind farm. *Wind Energy*, 15(4):525–546, 2012. doi: 10.1002/we.483.

WindEurope. Wind energy in Europe: 2021 statistics and the outlook for 2022-2026, 2022.

John C. Wyngaard. *Turbulence in the Atmosphere*, page pp.223. Cambridge University Press, 2010.

B. Yang, M. R. Raupach, R. H. Shaw, K. Tha Paw U, and A. P. Morse. Large-eddy simulation of turbulent flow across a forest edge. Part I: flow statistics. *Boundary-Layer Meteorology*, 120:377–412, 2006a. doi: 10.1007/s10546-006-9057-5.

B. Yang, M. R. Raupach, R. H. Shaw, K. Tha Paw U, and A. P. Morse. Large-eddy simulation of turbulent flow across a forest edge. Part I: flow statistics. *Boundary-Layer Meteorology*, 120:377–412, 2006b. doi: 10.1007/s10546-006-9057-5.